The MESSENGER Mercury Dual Imaging System (MDIS): Design, Observing Plan, and Calibration

S. Edward Hawkins, III[1], J. Boldt[1], E.H. Darlington[1], R. Espiritu[2], R. Gold[1], B. Gotwols[1], M. Grey[1], C. Hash[2], J. Hayes[1], S. Jaskulek[1], C. Kardian[1], M. Keller[1], E. Malaret[2], S.L. Murchie[1], P. Murphy[1], K. Peacock[1], L. Prockter[1], A. Reiter[1], M.S. Robinson[3], E. Schaefer[1], R. Shelton[1], R. Sterner[1], H. Taylor[1], T. Watters[1], and B. Williams[1]

[1] The Johns Hopkins University Applied Physics Laboratory, Laurel, MD
[2] Applied Coherent Technology, Herndon, VA
[3] Northwestern University, Evanston, IL
[4] National Air and Space Museum, Smithsonian Institution, Washington, D.C.

ABSTRACT

The MESSENGER Mercury Dual Imaging System (MDIS) will provide critical measurements tracing Mercury's origin and evolution.. MDIS consists of a coaligned monochrome, narrow-angle camera (NAC) and a multispectral, wide-angle camera (WAC). The NAC is a 1.493° field-of-view (FOV) off-axis reflector with a 1024x1024 Thomson (Atmel) TH7887A CCD at the focal plane. The WAC uses a 4-element refractor to provide a 10.54° FOV, and includes a 12-color filter wheel allowing characterization of Mercury's surface. The WAC CCD is identical to that of the NAC, and both share the same electronics. The NAC and the WAC are mounted on a pivoting platform that provides a 90° field of regard, extending 40° sunward and 50° anti-sunward from the spacecraft +Z-axis which contains the boresights of most of MESSENGER's instruments. Onboard data compression provides capabilities for pixel-binning, remapping of 12-bit data into 8 bits, and lossless or lossy compression. MDIS will acquire 4 main data sets at Mercury during 3 flybys and the 2 Mercury solar day nominal mission: a monochrome global image mosaic at near-zero emission angles and moderate incidence angles, a stereo-complement map at off-nadir geometry and near-identical lighting, multicolor images at low incidence angles, and targeted high-resolution images of key surface features. These data will be used to construct a global image basemap, a digital terrain model, global maps of color properties, and mosaics of high -resolution image strips. Analysis of these data will provide information on Mercury's impact history, tectonic processes, the composition and emplacement history of volcanic materials, and compositional variations and thickness distribution of crustal materials. This paper summarizes MDIS's science objectives and technical design, presents detailed results from ground and early flight calibrations, and outlines the plan for Mercury image products to be generated from MDIS data.

xxxx

1. INTRODUCTION

Mariner 10 executed three flybys of Mercury in 1974-1975, providing a reconnaissance view of one hemisphere and measuring the planet's magnetic field and interaction with the space environment. No spacecraft has returned in the intervening thirty years and thus our knowledge of Mercury's composition, origin, and evolution is limited. However, from Earth-based remote sensing and the Mariner 10 flyby observations (*Murray 1975*) we have inferred that Mercury has a high metal-to-silicate ratio, that its silicate portion is relatively depleted in FeO (*Rava and Hapke, 1987; Vilas 1988; Blewett et al., 1997; Robinson and Taylor 2001*), and that volatile species such as Na and K (*Potter and Morgan, 1985, 1986*) are present in Mercury's surface-bound exosphere. Even though our understanding of Mercury's bulk composition is so limited, constraints on models of formation and evolution of the planet are still possible. The planet's high metal content and presence of volatile species and FeO (albeit at low levels) demands a complicated, rather than simple, formation history. If Mercury simply condensed out of the very hot, and thus refractory, inner portion of the early nebula, it should have no volatiles and no FeO (e.g. *Lewis 1972, 1974*). At the other extreme Mercury may have accreted from planetesimals that originated from a wide range of regions within the Solar System, even as far out as Mars (*Wetherill, 1994*); in such a case Mercury should have more volatiles and more FeO than is indicated with current measurements.

The Mariner 10 images showed a heavily cratered surface grossly similar to that of the Earth's moon (*Murray et al, 1975; Spudis and Guest, 1988*). One of the more distinctive morphologic features discovered by Mariner 10 is a class of tectonic features known as lobate scarps, which are interpreted to reflect large-scale compressional deformation of Mercury's crust. Their origin has been hypothesized as buckling of the rigid outer portion of Mercury as the planet's interior cooled and thus shrank, or tidal despinning, or a combination of the two (*Strom et al., 1975, Cordell and Strom, 1977, Melosh and Dzurisin*, 1978; *Pechmann and Melosh*, 1979; *Melosh and McKinnon*, 1988). Another distinguishing mercurian feature is the smooth plains unit, which is comparable in morphology to the lunar mare deposits. However the smooth plains lack the distinctive low albedo of their lunar counterparts, and thus must have a very low FeO content (*Trask and Guest, 1975; Strom, 1977; Keiffer and Murray, 1987; Rava and Hapke, 1987; Spudis and Guest, 1988*). As an example of our current state of ignorance concerning Mercury, the volcanic origin of the smooth plains is still debated (*Wilhelms, 1976; Keiffer and Murray, 1987; Robinson and Lucey 1997*).

Earth-based radar has not only returned images of Mercury's polar regions rivaling those obtained by Mariner 10 (*Harmon et al., 2001*), but it has also discovered an anomalous class of materials inside permanently shadowed crater interiors in both polar regions. These materials exhibit high radar reflectivity and a circular polarity inversion consistent with a volume scatterer (*Slade et al., 1992, Harmon and Slade, 1992*). Water ice remains the leading hypothesis to explain the shadowed deposits, but many unanswered issues remain and final resolution must await orbital observations (*Harmon et al., 2001*).

The MESSENGER (Mercury: Surface, Space Environment, GEochmistry, and Ranging) spacecraft was conceived, designed, and built to address six fundamental science questions regarding the formation and evolution of Mercury (*Solomon et al, 2001*). (1) What planetary formational processes led to the planet's high metal silicate ratio? (2) What is Mercury's geological history? (3) What are the nature and origin of Mercury's magnetic field? (4) What are the nature and dynamics of its thin atmosphere and Earth-like magnetosphere? (5) What are the structure and state of Mercury's core? (6) What are the radar-reflective materials at Mercury's poles? What are the important volatile species and their sources and sinks on and near Mercury? Investigating these diverse questions requires a diverse set of scientific measurements from an array of instruments. MESSENGER carries ten miniaturized instruments organized into seven packages (*Gold et al., 2003*): the Gamma Ray and Neutron Spectrometers (GRNS), X-Ray Spectrometer (XRS), Mercury Dual Imaging System (MDIS), Mercury Laser Altimeter (MLA), Magnetometer (MAG), Mercury Atmospheric and Surface Composition Spectrometer (MASCS), and Energetic Particle and Plasma Spectrometer (EPPS). Additionally, a radio science investigation will address key measurements such as Mercury's physical libration.

2. MDIS SCIENCE OBJECTIVES AND DESIGN IMPLEMENTATION

MDIS's two cameras provide capabilities tailored to the elliptical orbit and imaging requirements of the MESSENGER mission. The WAC consists of a 4-element refractive telescope having a focal length of 78 mm and a collecting area of 48 mm^2. The focal plane is a Thomson (Atmel) TH7887A frame-transfer CCD with a 1024x1024 format and 14-µm pitch detector elements which provide a 179 µrad instantaneous field-of-view (IFOV). A 12-position

filter wheel provides color imaging over the spectral range of the CCD detector. Eleven spectral filters covering the range 415 to 1020 nm are defined to cover wavelengths diagnostic of different surface compositions, and have bandwidths from 5 - 40 nm (Table 4). The filters are arranged on the filter wheel in such a way as to provide complementary bandpasses (e.g., for 3-color imaging, four color imaging, etc.) in adjacent positions. The NAC is an off-axis reflective telescope with a 550 mm focal length and a collecting area of 462 mm^2. The focal plane is identical to the WAC's, providing a 25 μrad IFOV. The NAC has a single medium-band filter (50 nm wide, centered at 750 nm) whose center wavelength is matched to that of the WAC filter for monochrome imaging. Due to thermal constraints, only one camera will operate at a time; however, observations with the two cameras can be interleaved at five second intervals.

The MESSENGER spacecraft will make three flybys of Mercury, in January 2008, October 2008, and September 2009, during which regions unexplored by Mariner 10 will be imaged by MDIS. In March 2011, the spacecraft will begin the orbital phase of its mission, which is one Earth year in length. The orbital mission is just longer than two mercurian solar days, which are 176 Earth solar days in length.

The MDIS investigation will begin with the three flybys, and continue through the orbital mission. The two primary imaging objectives during the flybys are:

1. acquisition of near-global coverage at ~500 m/pixel (this is a lie), and
2. 11-filter multispectral mapping at ~2 km/pixel for greater than 60% of the planet (I made up the number). During the flyby departures large portions of the planet are viewed at a uniform low phase angles.

From orbit, gaps in color imaging acquired during the flybys will be filled with images taken at a wide variety of lighting geometries (this sentence seems out of place – perhaps move it to orbital observation paragraph below?). Total flyby coverage will exclude only the polar regions and two narrow longitudinal bands. The flybys each have one of two basic geometries (Table 1), and similar observation strategies will be used for each (Table 2). During the flyby phase, 85% of the planet will be imaged in monochrome at a resolution averaging ~500 m/pixel and in color at about 2 km/pixel. Half of the planet will be covered in color at ~1 km/pixel. High-resolution NAC swaths will contain monochrome images at better than 125 m/pixel (I thought we could do better than that?).

During the Mercury orbital phase of the mission the MDIS observation strategy will shift to acquisition of four key datasets:

1. nadir-looking monochrome (750-nm) global photomosaic at moderate solar incidence angles (55-75°) and 250 m/pixel or better sampling,
2. 25°-off-nadir mosaic to complement the nadir-looking mosaic for stereo,
3. completion of the multispectral mapping begun during the flybys, and
4. high-resolution (20-50 m/pixel) image strips across features representative of major geologic units and structures.

Both the nadir and off-nadir image mosaics will be acquired with the NAC for southern latitudes when altitude is high, and the WAC at lower altitudes over the northern hemisphere (Fig. 1). This two camera strategy results in near-uniform global coverage with an average spatial resolution of140 m/pixel (I thought this number was 250 m/pixel?). The off-nadir mosaic will be acquired under nearly identical lighting geometries to the nadir map to facilitate automated stereo matching. The stere derived global digital elevation modelwill have a spatial resolution of 1-4 km horizontal and 100-500 m vertical resolution, depending on latitude. MDIS stereo imaging will be the main source of surface elevation mapping for the southern hemisphere, as MLA's 1000-km range largely limits laser altimetry to the northern hemisphere. Filling gaps in color coverage is a relatively simple matter of pointing at and imaging a particular location during times of favorable lighting, except at low altitudes over high northern latitudes. At northern mid-latitudes, low spacecraft altitudes will limit viewing opportunities and probably require gap-filling images to be taken in long strips. At the time of this writing, the exact strategy for gap-filling of flyby color mapping is still being defined. High-resolution NAC imaging is effectively limited by ground motion smear (? Which potentially could be removed from a camera with a decent PSF) to about 20 m/pixel in the along-track direction: accurate post-processing correction for electronics artifacts (section 4.3) requires exposure times ~7 ms or longer, equivalent to <20 m of along-track motion smear.

2.1. Science Traceability

Table 3 summarizes the flowdown of requirements from science objectives to instrument design and data acquisition strategy, and compares the instrument requirements to as-built performance.Key constraints on the design of the MDIS investigation are the spacecraft's thermal environment, its highly elliptical orbit, the vertical accuracy required of stereo imaging, the low downlink rates, and the need to provide optical navigation prior to each Mercury flyby.

At Mercury, the intensity of the solar radiation varies from about 7 to 10 times the total irradiance falling on the Earth. A large sunshade protects MESSENGER from this intense solar illumination thus constraining the spacecraft pointing ability — however a variety of geometries is required for imaging. To support optical navigation during the flybys Mercury will be imaged against the star background thus MDIS had to be designed to image at phase angles as high as 140°. At the other extreme, flyby science observations requires imaging at phase angles of 32°.. To compensate for the limited pointing capability of the spacecraft imposed by the sunshade, the dual cameras of MDIS are able to pivot about a common axis (Fig. 2). The nominal scan range of the platform is 40˚ in the sunward direction and 50˚ anti-sunward. With spacecraft slewing, phase angle coverage of 28°-142˚ is possible in both cameras at the centers of their FOVs. Actual imaging is available in the WAC 5.27˚ further in each direction due to the wide FOV, and in the NAC 0.75° further. During launch and key orbital maneuvers, the camera can be placed in a stowed position, providing contamination protection for the optics (Fig. 3).

The thermal environment poses challenges for MDIS performance, because the cameras must point at the hot (up to 470°C) mercurian surface on some orbits for >60 minutes (or whatever the right number is). Although this thermal environment presents issues for all parts of the instrument, the most stressing case is maintaining nominal CCD temperature. Wide swings in detector temperature potentially degrade SNR, calibration accuracy, and thus science value of the

data. One example is the temperature-dependence of dark current, which increases with increasing temperature. In order to facilitate accurate dark current modeling and correction, there is a masked strip ("dark strip") on each CCD that measures dark current simultaneously with each scene image. As will be discussed in section 4.2, the accuracy of dark current modeling and removal degrades at higher dark levels. For "typical" exposure times of several hundred ms, residual uncorrected dark current approaches noise levels from photon counting at a CCD temperature of 5°-10°C. Accuracy of dark removal, to limit degradation of SNR, thus requires operating temperatures several degrees lower than this.

DOES THIS PARAGRAPH NEED TO BE IN THE PAPER?

Another impact of temperature on calibration accuracy is (section 4.6.2) the relative responsivity of the CCDs at wavelengths longer than about 700 nm. Responsivity at longer wavelengths increases strongly with temperature. If data are acquired over a large temperature range, inaccuracies in correction for temperature-dependent responsivity will introduce systematic errors in spectral properties at 850-1000 nm that ultimately could lead to false mineralogic interpretations. To protect the MDISCCDs from wide temperature swings incoming thermal IR radiation is rejected in the optics. In the WAC this is accomplished using a short-pass filter as the outer optic, for the NAC the bandpass filter also serves as the heat-rejection filter. To buffer temperature swings between times when MESSENGER is over the day or night side of Mercury, each MDIS CCD is thermally coupled to a wax phase change material (Fig. 4). During times of high heat input the wax melts and absorbs heat; at other times heat is dissipated by a radiator, and the wax refreezes. This system is predicted to maintain the CCDs in the operating temperature range -40°C to -10°C.

The thermal environment also poses a challenge for stereo imaging. Stereo provides measurement of both relief (the elevation difference between stereo resolution cells, about 5x5 to 7x7 pixels in size) and elevation relative to mean planetary radius. In the southern hemisphere, beyond the range of the MLA, the primary knowledge of elevation to mean planetary radius will be from photogrammetric analysis of MDIS images. Accuracy in an elevation determination from stereo is proportional to orbital altitude * σ / tan *e*, where σ is uncertainty in pointing knowledge between image pairs, and *e* is the emission angle of the off-nadir image. The goal for elevation is ±2 km accuracy of elevation. Assuming that accuracy can be improved by a factor of 2 using photogrammetric techniques at the corners of 4 stereo pairs, the required accuracy is ±4 km. For a 6000 km orbital altitude, which is relevant to southern high latitudes, and a 25° emission angle of the off-nadir images, the required pointing knowledge is ±240 μrad. This is requirement is budgeted between uncertainty due to knowledge in time of image acquisition (which translates into downtrack position error), uncertainty in pivot position within its plane of motion, and variation in orientation of the pivot plane relative to the star camera due to thermal distortion of the spacecraft. The largest term is due to variation in pivot plane orientation relative to the star camera (Table 3d). On the NEAR mission, orientation of its fixed-pointed camera was modeled to ±130 μrad as a function of temperature of spacecraft structure, using star-field images to calibrate pointing. Allowing for the fact that MDIS moves in a plane, and that the plane may shift in orientation with temperature, the budget is increased by √2 to 180 μrad, leaving 140 μrad for uncertainty in position within the gimbal plane and along-track errors. To facilitate pointing calibrations with MESSENGER's limited downlink, the spacecraft main

processor provides a subframing capability that allows up to 5 subframes per image encompassing stars.

The elliptical orbit results in challenges due to spacecraft range and velocity. For all launch dates and mission times, spacecraft altitude above the surface may ranges between 280 and 15,000 km on the dayside. This variation, combined with the requirement for imaging at near-nadir geometries, drove the selection of camera optics. The WAC's 10.54˚ FOV is sufficient that overlap occurs between nadir-pointed image strips taken on adjacent orbits, even at northern mid-latitudes where low altitudes occur. The NAC's 1.5˚ FOV is sufficiently narrow that 375 m/pixel sampling is attained at 15,000 km altitude. Low emission-angle geometries are available each solar day for all parts of the planet from altitudes of less than 10,000 km, providing 250 m/pixel sampling or better. The low altitude at periapsis also drives the speed of image acquisition. For multispectral imaging, acquisition of 11-color data from the minimum dayside altitude (~280 km) requires the WAC to take images at 1 Hz cadence. Along-track continuity of high-resolution imaging also requires 1 Hz imaging. In neither case is full resolution of either the WAC or NAC required; 2x2 pixel binning on-chip meets the spatial sampling requirements both for WAC color and for NAC high-resolution imaging from low altitude. Meeting low-altitude imaging requirements thus drives the speed of the WAC filter wheel (1 Hz imaging in adjacent filters) and link speed from either camera to the recorder (12-bit, 512x512 frames at 1 Hz) as described in Tables 3c and 3d.

The MESSENGER mission requires compression to meet its science objectives within the available downlink.. Figure 5 summarzies the compression options available to MDIS at the instrument level and using the spacecraft main processor (MP). At the focal plane, 2x2 binning is available on-chip to reduce the 1024x1024 images to 512x512 format, 12-bit DN levels can be converted to 8 bits, and data can be compressed losslessly. The strategy for DPU image compression is to acquire all monochrome data in 8-bit mode, and color data 12-bit, and to compress all data losslessly to conserve recorder space. Image format is controlled by loading imposed on MP compression by the total number of pixels to be compressed per day. After data are written to the recorder, they can be uncompressed and recompressed by the MP more aggressively using any of several options: additional pixel-binning, subframing, and lossy compression using an integer wavelet transform. The strategy for MP compression is that all data except flyby color imaging will be wavelet compressed, typically 8:1 for monochrome data and to a lower ratio ($\leq$4:1) for orbital color data. Color imaging but not monochrome imaging may be further pixel-binned. For the special case of optical navigation images, there is a "jailbar" option that saves selected lines of an image at a fixed interval for optical navigation images of Mercury during flyby approaches..

Compression performance has been extensively modeled prelaunch. The 12-to-8 bit look-up tables have been designed to preferentially retain information at low, medium, or high 12-bit DN values, for a nominal detector bias or for one that has decreased with time (Fig. 6). Compression ratios to be used for flight ratios have been based on a study of the magnitude and spatial coherence of compression artifacts using NEAR images (Fig. 7). For expected loading of the main processor, simulations have shown that the MP can compress the equivalent of 82 full 1024x1024 images per day (or 330 512x512 images per day). The actual number of images has also been simulated, based on orbital trajectory simulations and the imaging plan described

below. The MP image compression capabilities are consistent with the mission-average number of images per day. However on peak days when lighting is favorable for global mapping, a peak of ~260 images per day may be expected, requiring on-chip binning of most of the data on peak days. The full implications for average imaging resolution are still being assessed.

The final set of driving requirements involves responsivity required for mapping Mercury and for optical navigation. For WAC spectral filters, bandpass widths were selected to provide required SNR in exposure times short enough to prevent linear smear due to along-track motion, yet long enough (>7 ms) to avoid excessive artifacts from removal of frame transfer smear during ground processing. SNR is not an issue, as sufficient light is available for SNRs >200, but saturation is a concern at low phase angles. At the same time, both cameras must be sensitive enough to provide star images for optical navigation. When imaging Mercury against a star background, at least 3 stars must be visible per image, at ≥7x noise. For the WAC this was easily accomplished (Table 5a) using a clear filter. For the NAC, its single filter was designed with a first priority of not saturating on bright crater ejecta while imaging Mercury at low phase angles using pixel binning. As a consequence, sensitivity to stars is limited. Detection of 3 stars per frame for a typical patch of sky is only marginal (Table 5b).

2.2. Data Acquisition Strategy

2.2.1. Flyby Imaging

The MESSENGER trajectory provides three flyby opportunities of Mercury (January 2008, October 2008, September 2009, Table 1, Figures 8 and 9). During the first flyby, approximately half of the hemisphere not viewed by Mariner 10 will be illuminated (subsolar longitude 170°W); the first Mercury data return from MESSENGER will thus observe new terrain, including the previously unseen western half of the Caloris Basin and its ejecta. During the second flyby, illumination will be centered on the eastern edge of the Mariner 10 hemisphere (subsolar longitude 356°W). The lighting geometry for the third encounter will be nearly identical to that of the second encounter with the subsolar point at the prime meridian (0°W); however the approach and departure phase angles will be less extreme, resulting in better inbound imaging. During the second and third flybys, most of the remaining unseen portion of Mercury will be imaged. Total coverage between Mariner 10 and the three flybys will exclude only the poles and a small longitudinal gap ~6°-wide, centered at ~263°W longitude. Due to the equatorial closest approach on all three flybys, resolution will diminish towards the poles and limb. From the flybys >80% of the planet will be imaged in monochrome at a resolution averaging ~500 m/pixel (big fat lie) and in color at ~2.4 km/pixel. Half of the planet will be covered in color at ~1.2 km/pixel. High-resolution data swaths will contain monochrome images at better than 125 m/pixel (isn't it higher resolution than this?). The detailed flyby imaging plan is given in Table 2.

Mosaicking images from the various photometric geometries obtained during the flybys and from orbit will require an accurate photometric model of the planet at the wavelengths of the NAC and WAC filters. Therefore, MESSENGER will perform a sophisticated photometric characterization of Mercury's surface from data acquired during the flybys, as well as during orbital operations, through observations of the same point on the ground acquired at various

emission, incidence, and phase angles. During each flyby one area on the surface will be observed at 11 different phase angles in 10° increments. Due to Mercury's slow rotation these observations will have a fixed incidence angle – only the emission and phase angles will change.

2.2.2. Orbital Imaging

MESSENGER will be placed in a highly elliptical orbit with a periapse of 200 km at ~64˚N and an apoapse of 13100 km (Fig. 1). The orbit has a 12-hour period, is inclined 80˚ to the planet's equatorial plane, and is not sun-synchronous. During one Mercurian solar day, the orbit precesses completely around the planet twice. At times the groundtrack is near the terminator (the "dawn-dusk orbit" in Fig. 1); 22 days later it passes over the sub-solar point (the "noon-midnight" orbit in Fig. 1).

Global monochrome basemap. One of the primary goals of MDIS is to acquire a global monochrome basemap at 250-m/pixel average spatial sampling, low emission angle, and moderate incidence angle (what does moderate mean? For a photometrist this might mean 10-45 and to a morphologist 50-80). For a given area coverage is obtained at the first opportunity when local nadir is viewed at solar incidence angles of 55°-75˚. Selection of the combination of emission and incidence angles dictates that the spacecraft will be nearly in a dawn-dusk orbit, minimizing thermal disturbances to pointing. The choice of NA or WA camera is driven by the necessity of maintaining both cross-track overlap and near uniform spatial resolution (140 m/pixel, Fig. 10): the NAC will be used to image the southern hemisphere, whereas the WAC will be used in the northern hemisphere. (Fig. 10). For monochrome imaging, the 750 nm filter is used in the WAC to match the 750 nm bandpass of the NAC. The global nadir-viewing basemap is planned for completion during the first mercurian solar day (i.e., during the first half of the orbital mission).

Stereo mapping. The off-nadir stereo-complement to the basemap will consist of images taken at nearly the same local solar time. This occurs with the spacecraft in the same nearly dawn-dusk orbit, again minimizing the thermal disturbance to pointing and the propagation of pointing uncertainty into uncertainty in southern-hemisphere elevations. Off-nadir pointing will be accomplished using the capability of the guidance and control system to point up- or down-track by commandable offsets.

The downlink profile over the course of the orbital mission is heavily front-loaded due to favorable Earth-Mercury distance thus the off-nadir complement will be time-phased to take advantage of this high downlink rate. In the southern hemisphere, stereo mapping will be accomplished entirely during the first solar day. Imaging on one orbit will be at nadir (0˚ emission), then on the next orbit off-nadir (25° emission), and the sequence will be repeated so that nadir and off-nadir mapping will be built up simultaneously. The northern hemisphere will be imaged at nadir on the first solar day, then on the second solar day the same image sequence will be repeated except off-nadir, covering locations at the same local solar time as in the nadir map. The vertical precision of the stereo map will typically be about 100 m.

Gap-filling the flyby color map. Once in orbit, the remaining gaps in the flyby color maps will be filled. Details of the exact mapping strategy are still under development, but

acquisition will mesh with the global monochrome and stereo mapping. The southern hemisphere will likely be imaged as mosaics centered on given latitude and longitude, while the northern hemisphere will probably be imaged as strips which are pixel-binned on-chip, in order to obtain images in a greater number of filters with no gaps.

Polar mapping. In order to identify permanently shadowed (and permanently illuminated) areas, polar regions will be imaged repeatedly throughout the mercurian solar day during every second orbit, so that all longitudes are illuminated at 5° increments of solar longitude. This strategy provides coverage of all areas near their minimum solar incidence angle. Coverage will extend from 85˚ or lower latitude to the pole on the nightside, and from 80˚ or lower latitude to the pole on the dayside. At the south pole, the campaign will be divided between the two solar days. On the first solar day, the WAC will be used while the spacecraft is at high altitude, providing ~1.5 km spatial sampling and extending equatorward to approximately 70° latitude on the dayside. On the second solar day a more limited region will be covered at higher resolution, using one 2x3 NAC mosaic per day with long axis aligned N-S. The latter provides about 200 m/pixel spatial sampling.

For the northern polar region, the entire first solar day is required for the monochrome basemap, so the polar campaign will be delayed until the second solar day. The WAC will be used because its wider FOV is required for latitude coverage. The imaging strategy will parallel that used for the NAC in the southern polar region, using one 2x3 mosaic per day with long axis aligned N-S (THE PREVIOUS PARAGRAPH TELLS A DIFFERENT STORY!!!).

High-resolution imaging. Selected areas of the northern hemisphere, identified for the most part in flyby imaging, will be imaged from orbit at resolutions of up to ~20 m/pixel. The NAC has a "fast" 1 Hz mode for this purpose, which will acquire images binned 2x2 on-chip in continuous strips 512 pixels wide. At low dayside altitudes (280 km), spatial sampling is 11 m/pixel but along-track motion smear is 18 m at the shortest exposure consistent with low artifacts from frame transfer smear. Due to MESSENGER's highly elliptical orbit high-resolution imaging is possible only in the northern hemisphere.

Targeted color. Selected regions of the planet will be targeted on the second solar day for full-resolution color imaging with spatial sampling up to ~400 m/pixel using the ability of the guidance and control system to track a commanded latitude and longitude on the surface. The maximum spacecraft angular velocity dictates the minimum altitude and thus best spatial sampling at which this can be done. Initial targets will be identified from Mariner 10 data and MESSENGER flyby results.

Color photometry. During the orbital phase of the mission, photometric geometry complementary to that measured during the flybys is possible: incidence angle variations will be measured at nearly constant emission angle. Key features in low southern latitudes will be imaged repeatedly while the spacecraft is high (10,000 km) above high southern latitudes as the sub-solar point moves from terminator to near noon-time. Several target areas will be selected: one to represent average Mercury (heavily cratered highlands), another representing intercrater plains, and a third representing smooth plains materials (probably Tolstoj plains).

Including the flyby and orbital observations, the photometric properties of Mercury will be characterized over greater than 80° of emission angle, 100° of phase angle, and 80° of incidence angle. Results from this experiment will not only characterize photometric properties of the surface, but also photometric normalization to a standard geometry (30° solar incidence angle, 0° emission angle) for production of mosaicked products.

On-orbit calibrations. In order to maintain accuracy of southern-hemisphere elevation measurements, pointing calibrations will be interleaved with nadir and off-nadir global mapping. Once or twice per orbit, depending on orbital geometry, MDIS will be pointed off the planet using the pivot and star images acquired using the WAC at at least two gimbal orientations (Ii simply do not understand this sentence). Sub-frames centered on stars will be utilized to minimize the data volume required. Onground, these data will be used to solve for gimbal plane orientation as a function of temperature at the base of MDIS.

3. INSTRUMENT DESCRIPTION

The full MDIS instrument is comprised of two redundant external Data Processing Units (DPUs) and a pivoting dual camera system (Figure 2). This assembly consists of two main components, a bracket assembly that interfaces to the spacecraft, and a pivoting platform on which both cameras and the thermal control system are located (Figure 11). The overall design and look of the instrument was driven by the severe thermal environment, and the requirement for a large field-of-regard to assist in optical navigation.

The bracket assembly supports the DPU Interface Switching Electronics (DISE) box that connects the active DPU to the MDIS instrument. Only one DPU may be active at a time. The pivot platform consists of the multispectral WAC and the monochrome NAC. The motor drive train permits very small steps (150 μrad/step) with deviations from normal over the full pivot range of <85 urad, and is expected to be substantially better over the operating range of motion (-40° to +50°) (this sentence confuses me). An innovative thermal design maintains the CCD detectors in the WAC and NAC within their operating temperature range of (-40°C to -10°C), over a MESSENGER orbit.

Protective covers for optical components are very desirable during ground-based testing, launch, and trajectory maneuvers requiring large thruster burns. However, due to mass limitations conventional protective covers for MDIS were not practical. Instead, the critical first optic of each telescope is protected by rotating the platform 180 deg from the +z direction such that both cameras look downward into the deck (Figure 3). This innovative approach ensures a circuitous path for any particulate or molecular contamination.

A spectral calibration target is mounted on the inside of the payload adapter ring. Early in the mission it will be possible to rotate the spacecraft and provide solar illumination on the calibration target, permitting absolute inflight radiometric calibration.

3.1. Bracket Assembly

The bracket assembly, made of the same advanced composite material (graphite/cyanate ester fabric pre-preg) as the MESSENGER spacecraft structure, was chosen to minimize mechanical stresses due to mismatches in coefficients of thermal expansion. The composite bracket assembly, being a very poor thermal conductor, isolates the pivot platform and thereby the cameras from the payload instrument deck. Eight titanium feet form the mechanical interface to the spacecraft. Four feet are bonded to each stand using a precision fixture, then bolted to the stand. A trim cut machined from a top layer of epoxy on each composite stand ensured that the pivot axis of rotation would be parallel to the spacecraft deck.

The pivot motor assembly is located on one of the composite stands and is comprised of a stepper motor, resolver, and harmonic drive assembly. The stepper motor contains redundant windings so that the two fully redundant DPUs can independently control the motion of the pivot, enhancing the overall reliability of the pivot mechanism.

The total range of motion of MDIS is 239.71, limited by hard mechanical stops in the pivot motor. Pointing knowledge is determined by "homing" the instrument by driving the actuator into one of the mechanical hard stops for a period of time sufficient to ensure the orientation of the instrument if it had been previously stopped at the opposite extreme of travel (about 4 minutes). Once the location of the pivot actuator is known, the flight software retains this knowledge and subsequent pointing commands are achieved by counting pulses (steps) to the motor. The pivot actuator assembly also includes an angular position sensor (electrical resolver). However, due to mechanical distortions in the drive shaft and electrical noise in the device itself, the output resolution (of what?)_is worse than a step size (150 μrad). The actuator mounts on a titanium bracket, designed to thermally isolate the platform assembly from the bracket stands, while not introducing any pointing errors due to thermal gradients from the composite stand to the platform. A precision titanium shaft mounts to the motor output flange. All assemblies are drilled and pinned to limit uncertainties in alignment of mechanical assemblies.

In my corrections I may have subtly changed the intent, make sure I didn't pervert the meaning…

The titanium bracket opposite the pivot actuator supports a bearing mount, flexible diaphragm, hollow shaft, and electrical feed-through. Strict attention to mechanical tolerances (very fuzzy, just state the tolerances) was paid to all components, with particular attention given to components that could contribute to errors in pointing. A duplex pair of angular contact bearings was chosen for the pivot because the stainless steel races and ceramic balls ensure minimal diffusion between the two surfaces and reduce the risk of "cold welds" which over time could decrease the torque margin of the motor. The angular contact bearings use a dry lubricant, MoS_2, and underwent a run-in period prior to installation. After preliminary cleaning, the bearings underwent a vacuum soak for 24 hours (why?) to degas???? Dehydrate???. The bearings were exercised in a dry-N_2 environment for 10,000 cycles (revolutions) clockwise, followed by 10,000 cycles in the counterclockwise direction.

A clearance of 12 μm between the outer race of the bearings (the same angular contact bearings mentioned in the previous paragraph?) and the inner diameter of the bearing holder was established. The bearings were pressed into the bearing holder by heating the titanium holder to 100°C, while keeping the bearings at room temperature. The hollow shaft was fabricated to have a line-to-line fit (zero clearance to within measurement error which was?). Assembly of the hollow shaft required pressing the shaft into the bearing and bearing holder by cooling the shaft to -100 C, with the bearing and holder at room temperature. Figure 12 shows the hollow shaft after assembly into the bearing holder, and the flexible diaphragm. The precision diaphragm permits motion along the axis of rotation while maintaining the trueness of the rotation axis.

Perpendicularity of the mating surfaces on the hollow shaft, motor shaft, and pivot platform were maintained to within machining limits. After heating the magnesium pivot platform, the hollow shaft was pressed into place. The rotational orientation of the motor shaft established the final alignment of the pivot platform relative to the spacecraft. Special keying tools ensured proper orientation of the motor shaft prior to it being pressed into the platform.

Once the rotating portion of the MDIS instrument was determined to satisfy the pointing requirement in terms of trueness of rotation to within the allowed tolerance, it was necessary to maintain the perpendicularity of the rotation axis to the mounting feet. A high precision fixture was fabricated to emulate the spacecraft instrument deck (Figure 13). Each composite stand was mounted to the fixture and the pivot platform assembly was loosely attached to the stands. Using a Coordinate Measurement Machine (CMM), two parallel planes were established relative to the mounting feet. The hardware attaching the motor drive train (bracket/pivot assembly) to the composite stands was slowly tightened. An iterative process of measuring the relative parallelism of each bracket to the mounting feet was performed until the motor bracket measured parallel to the mounting feet to 10 μm (0.4 mils) and the diaphragm bracket measured parallel to motor stand feet at 13 μm (0.5 mils). The assembly was bagged, and the motor/diaphragm brackets were drilled and pinned to the composite stands. Runout measured at the bearing end of the hollow shaft as shown in Figure D was determined to be less than 20.3 μm (0.8 mils), corresponding to a rotational deviation from normal of < 85 urad.

The MDIS pivot actuator (Figure 15) is capable of accurately stepping in intervals of 0.0086° (~150 μrad) per step, achieved through a hybrid gear-train within the actuator. The 5° stepper motor is coupled to a 4.84:1 in-line planetary gear-train, used to drive the wave generator of a harmonic drive. Harmonic drives permit very precise pointing and high torque ratios at lower mass than comparable conventional gear systems. These devices use a radial motion to engage the teeth of a flex-spine and a circular-toothed spline, rather than the rotating motion of other gear systems. This motion allows for very high gear ratios and near zero-backlash performance. The harmonic drive in the pivot actuator provides an additional factor of 120:1 mechanical advantage, resulting in a total gear ratio of 580:1. The maximum rotational speed of the pivot platform is 1.0078 deg/s. Why isn't this paragraph up with the previous material describing the pivot on the previous page, they seem very related?

A stainless steel rotary feed-through (twist capsule), shown in Figure 14, mounts to the bearing holder and passes through the hollow shaft. All electrical connections to the platform pass through the 110 conductors of the twist-cap. The angular extent of the twist-cap is +90° to -220° and exceeds that of the pivot motor. Rigid-flex circuitry inside the twist capsule, along with

stainless steel bearings, require extremely low torque to rotate. The connectors for each Focal Plane Unit (FPU) were assembled after the twist capsule was assembled. Most signal connections through the twist-cap are redundant and spliced just before each potted connector. The harness at the fixed end of the twist-cap largely connect to the DISE box.

3.2. Platform Assembly

The mass of the MESSENGER spacecraft and payload is tightly constrained,. As a result, housings were fabricated from magnesium wherever possible. The pivot platform, the two FPUs and the Filter Wheel Housing are fabricated from magnesium stock while he WAC telescope, filter wheel, NAC and WAC light baffles ar titanium and the NAC telescope is aluminum. The supporting structure for the radiators and heat-pipes is stainless steel, to match the CTE of the stainless steel heat-pipes and to minimize parasitic heat leaks from the radiators to the platform. The radiator panels are made of beryllium, selected for its light-weight and high heat capacity. Each beryllium panel is passivated (real word?) with a thin aluminum layer which is then clear anodized to optimize thermal properties.

The Filter Wheel actuator for the WAC (Figure 16) consists of a CDA-Intercorp DS9-A stepper motor with output step angle of 30°, and an in-line gear train with 50:1 reduction resulting in an output step size of 0.6°. The step rate is 120 deg/s permitting 1 Hz imaging using adjacent filters, provided the exposure is less than 490 ms. The output shaft of the motor has a double-D interface to the wheel assembly, and an internal spline to accept the shaft of the electrical resolver (DT1-A) angular position sensor. The motor mounts to the filter wheel housing, and the resolver mounts to the filter housing cover, eliminating the need for a bearing and provides a simple robust design.

3.3. Optical Design

The wide-angle camera (WAC) consists of a refractive telescope with a collecting area of 48 mm^2. The optical prescription is that of a modified Dogmar (reference?), as shown in Figure 17 (why is Figure 17 before figure 16?). The f/10 design has a focal length of 78 mm. Axial chromatic aberration over the wide spectral range of 395-1040 nm is corrected by varying the thickness of each filter, a technique used in the NEAR Multispectral Imager (*Hawkins et al. 1997*). The WAC is focused at infinity with a FOV of 10.54° and an instantaneous FOV (IFOV) of 178 µrad. The rms spot radii of the WAC optics are smaller than the 14-µm square pixels of the CCD, and the diffraction Airy disk radius is 8.5 µm at 700 nm.

The 12-position multispectral filter wheel provides color imaging over the spectral range of the CCD detector (395-1040 nm). Eleven spectral filters are defined to cover wavelengths diagnostic of common crustal silicate materials and have bandwidths (FWHM?) from 5-40 nm (Table 4). A broadband clear filter was included for optical navigation imaging of stars.. Filter shapes were designed to minimize the overall size and mass of the wheel assembly (Figure 16) and are constructed with a substrate of BK7G18 radiation-resistant glass, which is standard BK7 glass doped with 1.8% Ce, in combination with one or two colored glasses. The filters were

bonded in place using a low-outgassing epoxy (Arathane 8780). Radiation tests performed on the MDIS WAC filters imply that overall transmission loss should be <4% for the estimated 15 krad environment during the nominal MESSENGER mission. IS THERE ANY BAFFLING??? ANY STRATEGY TO REDUCE SCATTERED LIGHT?

The NAC optical design paragraph us very short. Can this be expanded? Scattered light, baffling etc…

The NAC has a 1.5° FOV and uses an off-axis reflective design with a single medium-band filter centered at 750 nm with a FWHM of 100 nm , with a center wavelength matching a WAC filter (750BW5). The filter is tilted 1 deg with respect to the optic axis to minimize scattered light. The telescope has a focal length of 550 mm and a collecting area of 462 mm2. The NAC ray trace is shown in Figure 18.

3.4. Electronics

3.4.1. Focal Plane Electronics

Both cameras have identical detector electronics contained in a modular focal plane unit (FPU). The FPU electronics are composed of multiple rigid-flex circuits (Figure 19) to minimize the size of the FPU and still satisfy the thermal requirements. Each FPU uses a Thomson (Atmel)-TH7888A frame-transfer CCD (Figure 20). A tantalum radiation shield (0.127 mm thick) not only protects the CCD but also blocks illumination to the memory zone. The 1 megapixel CCD has 14-µm square pixels and anti-blooming control. Custom hybrids are used to miniaturize the packaging of the clock drivers to the CCD (what the heck does this sentence convey?). All clocking, control, and readout takes place in a Field-Programmable Gate Array (FPGA) as shown in Figure 21. Due to thermal, power, and operational constraints, only one camera will operate at a time (I'm not sure where this sentence should go – it was randomly placed above.

Manual and autoexposure control from 1 ms to 9.988 s permits imaging targets over a broad range of intensities. The frame transfer time is 3.84 ms, so the minimum useful exposure is about 8 ms. Figure 21 shows the detailed timing for short exposures (≤988 ms) in the top panel, and long exposures (990 ms < exposure < 9988 ms) in the bottom panel. The maximum frame rate of each FPU is 1 Hz. Low Voltage Differential Drivers (LVDS) provide a robust interface to the DISE box and subsequently to the DPU. Pixel data are digitized to 12 bits using the AD9807. Latch-up protection circuitry for the A/D converter (AD9807) is provided.

The CCD provides specially shielded columns to provide an accurate measure of the dark level. Four of these dark pixels are sampled per line and substituted during readouit for four of the 1024 active pixels in a full resolution image (1024x1024). The four reference columns provide a measure of the dark background, even in the two on-chip binning modes. In the case of 2x2 binning, two dark reference columns are available (no mention of how screwed up these are…).

3.4.2. DISE

The (what does DISE stand for?) DISE box switches between the DPUs in a master/slave configuration and provides a regulated 6 V from the DPU-supplied 15 V. This approach maintains the high level of redundancy designed into the MESSENGER spacecraft, at the same time minimizing the total number of connections required to pass through the rotating interface. The 1.7 W dissipated in the DISE box gets conducted into the spacecraft deck through a thermal strap. A nusil thermal gasket applied to the copper strap just prior to mounting MDIS to the spacecraft ensures excellent thermal contact with the deck.

3.4.3. Data Processing Unit

The Data Processing Unit (DPU) provides data processing, power, and control, plus all interfaces to the spacecraft (Figure 23). The slices (?) communicate through various buses, which run through a stacking connector. Each 10.16 cm x 10.16 cm (4"x4") slice (???) is part of a standard packaging design that provides great flexibility in developing the control electronics for new flight instruments while reusing those portions of the design that do not change from program to program. The DPU-A and DPU-B are shown in Figure 22. Each DPU contains 8 slices: four digital control cards, and four power/motor control cards. A low speed RS-422 interface to the DPU is used for all commands from the spacecraft. Image data are transferred to the spacecraft via a three wire RS422 high-speed serial interface. The spacecraft interface limits the maximum image transfer rate of 3 Mbps, thus maximum full resolution 1024x1024 image transfer time is 4 s.

The DPU is designed to place as few demands on the spacecraft as possible. Dedicated power converters in the DPU provide power to the WAC and NAC, protecting the spacecraft from overcurrent fault conditions. Electromagnetic interference filters and surge limiting on each converter reduce instrument-conducted emissions and load switching transients on the spacecraft power bus.
Why is this thing called the DPU when it is more than that – power converters?

3.5. Thermal Design

The two FPUs with their CCD detectors are passively cooled. Because the instrument payload is protected from direct solar illumination by the spacecraft sunshade, the thermal environment of the instruments is largely benign with the exception of short intervals during the 12-hour orbital period when Mercury's illuminated surface subtends a large solid angle. The thermal design takes advantage of the eccentric orbit of MESSENGER around Mercury by radiatively cooling the pivot platform during most of an orbital period using aluminum coated beryllium radiators with a total area of 342 cm^2 and a total mass of 104 g (Figure X?).

The radiators are mounted on a stainless steel structure, and supported by thin titanium rods to form a spoke-like structure that minimizes heat conduction from the radiators back to the platform. The structure also supports two diode heat-pipes, a copper braid strap which ties each heat pipe to a wax pack on each camera. A thermal link, consisting of many thin sheets of aluminum, ties the wax pack to the CCD heat sink. A schematic of the thermal system is shown in Figure 4. This was discussed earlier – why two places. I find that there are many cases of redundant sentences throughout this whole paper!!!! Yuck…

Figure 24 shows the supporting structure and the two diode heat-pipes prior to assembly. Inside each heat-pipe is a working (?correct term?) fluid, butane, which remains in the gaseous (fluid which remains in the gaseous state – might not be the best wording) state as long as the pipe is cooler than the liquid trap. This is the working condition of the pipe, and the working fluid is free to transport heat from one end of the pipe to the other. If the pipe temperature exceeds the temperature of the liquid trap, the gas condenses, and heat from the radiators must conductively pass through the stainless steel pipes, which are very poor thermal conductors. The diode action of the heat pipe effectively operates as a thermal switch. THIS PARAGRAPH CONFUSES ME.

The heat pipes are made of 9.525-mm stainless steel tubing, and each pipe contains a wick which abets the heat transport. Copper pads or saddles are silver-soldered to the pipe at the location of each radiator panel. The surface flatness of each saddle and the radiator panels was controlled to ensure optimum contact area.

During cruise, the diode heat-pipes will operate as standard heat-pipes, cooling the wax packs connected to each FPU. Each wax pack contains ~240 g of paraffin that freezes at -9.9˚ C. Once the wax has frozen heat is continually removed from it via the thermal straps connected to the radiators thus cooling the CCDs. Survival heaters ensure that the temperature of the CCDs do not fall below their minimum operating temperature (about –45°C). In addition to the thermostatically controlled wax pack heaters, platform heaters maintain the pivot platform to above -45°C. Once MESSENGER has begun the primary phase of the mission, MDIS will rely on the diode action of the heat pipes to satisfy the thermal requirements.

Near periapsis thermal flux from the hot planet will be absorbed by the radiators. The choice of beryllium for the radiator materials provides the maximum latent heat for the smallest mass. A large latent heat results in the temperature of the radiator changing more slowly (than what?). As the radiators and hence the heat-pipes get warm, the fluid (what fluid?) condenses into the liquid trap and the heat-pipe shuts down. Parasitic heat losses to the radiator (what?), as well as heat generated by the CCD, begin to melt the wax, still maintaining the CCDs at about -10°C. Just as the beryllium has a large latent heat, the paraffin in the wax pack has a very large latent heat (240 W/g). Each wax pack on MDIS contains about 250 g of paraffin, which ensures that the wax does not fully melt over the 2-hour heat pulse during periapsis. The subsequent 10 hours of the orbit are more than sufficient to refreeze the wax, completing the thermal cycle.

The CCDs are thermally tied to the wax pack with thermal links and are thermally isolated from the FPU electronics and housing by precision titanium thermal spacers. An internal mulit-layer insulation (MLI) blanket further minimizes radiative coupling between the FPU electronics and the CCD. Panel A of Figure 25 shows the front panel of the NAC Focal Plane Unit that serves as reference surface for all mechanical tolerances. As shown in the panels A and B, the focus spacers are drilled and pinned in location to the front panel. G10 isolators increase the thermal resistance between the CCD heatsink and the front panel. The CCD itself is bonded to an aluminum heat sink with Uralane 5753. A thermal link is mechanically fastened to the back of the CCD heatsink, and an MLI blanket encompasses the entire CCD assembly. Panel

C shows the focal plane electronics are folded into the FPU housing, and the thermal link passes through an opening in the top cover of the housing.

Temperature sensors are mounted at key locations on the instrument (Figure 26) and reported in image headers. The most important temperature readout for calibration purposes are the CCD temperatures (section 4.2.1).

4. INSTRUMENT CALIBRATION

Laboratory measurements described in the following sections were used to derive values for the terms of the calibration equation as shown in Equation 1 for both the WAC and NAC. Both instruments measure relative light intensity in engineering units referred to asdata number [DN]. DNs are generally converted to radiance, R (W m^{-2}-μm^{-1}-sr^{-1}), following the calibration equation:

$$R(x,y,f,T,\tau,b) = \frac{[DN(x,y,f,T,\tau,b,MET) - Dk(x,y,T,\tau,b,MET) - Sm(x,y,\tau,b) - Scat(x,y,f,\tau,b)}{Flat(x,y,f,b) * Coef(f,b) * Resp(f,T) * \tau} \quad [1]$$

where:

DN(x,y,f,T,τ,b,MET) is the raw DN measured by the pixel in column x, row y, through filter f, at CCD temperature T and exposure time τ, for binning mode b, and Mission Elapsed Time (MET),

Dk(x,y,T,τ,b,MET) is the dark level in a given pixel, derived either from the dark strip or estimated from exposure time and CCD temperature,

Sm(x,y,τ,b) is the scene-dependent frame transfer smear for the pixel,

Scat(x,y,f,τ,b) is the contribution of scattered light from elsewhere in the scene,

Flat(x,y,f,b) is the non-uniformity or "flat-field" correction at this pixel location,

Coef(f,b) is the reponsivity, relating dark-, flat-, and smear-corrected DN per unit exposure time to radiance,

Resp(f,T) is the responsivity relative to the baseline operating temperature, and,

τ is the exposure time in milliseconds.

The analysis used to derive each term of the calibration equation is described in the following sections.

4.1. Ground Calibration Facility and Test Results

All calibration tests were performed in the Optical Calibration Facility (OCF) at the Johns Hopkins University Applied Physics Laboratory (JHUAPL). The OCF consists of large,

linked vacuum chambers with a host of support equipment. The largest of these chambers, the instrument chamber, has an internal diameter of 1.3 m, a length of 2 m, and permits mounting the instrument on a two-axis motion stage. The motion stage can rotate the instrument in azimuth and elevation through a range limited only by the instrument cable and mounting hardware. The interior and ends of the instrument vacuum chamber are surrounded by cold walls, within which an external refrigerator circulates a cooling fluid to reduce the internal temperature to approximately –40°C. Most of the calibrations were performed at approximately –30°C. However, additional thermal configurations over the range –34° to +25°C were also performed, to bracket the behavior of the instrument over the range of expected flight conditions. Figure 27 shows a schematic of the OCF test setup. Inside the instrument chamber, there are two sources of calibrated illumination. In one configuration the instrument views a 20-inch diameter, $BaSO_4$-lined integrating sphere through a 203-mm diameter quartz window. Dark cloth was draped around the window and sphere opening in order to block unwanted external light from entering the instrument optical path. Sphere spectral radiance was calibrated by Labsphere just prior to the start of instrument calibration, separately for each and its two 45-W lamps and two 150-W lamps. One photometer was coupled through a fiber optic to monitor the internal sphere brightness during all calibration runs. Two additional photometers (not shown in Figure 27) were mounted on the camera, and allowed additional monitoring of incident irradiance.

With a 180° rotation of the motion stage, the instrument looks along a beam tube, into an off-axis parabolic collimating mirror which has a focal length of 1.43 m, operates at f/7, and is focused on a grating monochromator. The monochromator is illuminated by an incandescent lamp with quartz optics. At the input slit is a set of neutral density filters to attenuate the light by known amounts. At the exit slit a set a long pass filters is used to remove higher orders (i.e., shorter wavelengths) from the grating. The wavelength can be changed manually or can be set to scan under computer control. Setting the grating to pass zero order allows the full incandescent spectrum to be passed.

The monochromator can be removed without breaking vacuum, and other sources placed at the focus of the collimator and viewed through a MgF_2 window. These sources include a point source (pinhole), pinhole array, and test samples illuminated by an incandescent source and viewed off a silver fold mirror.

A total of four networked computers were used to acquire and monitor the calibration data. Each computer had a specialized set of tasks to perform. The first was dedicated to running most of the OCF instrumentation such as the motion stage, monochromator wavelength adjustment, and filter wheel selection. The second computer served as a frame grabber that communicated directly to the instrument Digital Processing Unit (DPU). The operators ran the calibration scripts and monitored the progress of the runs from the third computer. The fourth computer presented real time images and plots on its screen allowing the analysts to monitor the calibration results during each experiment.

All data were saved locally on disk and were also automatically copied to the remotely located MESSENGER Science Operations Center (SOC) within approximately 30 sec of acquisition. The SOC provides a web interface to the data (Figure 28) organized by test, that includes facilities for searching the database for images in particular configurations, dark-

correction and desmearing of data as collected (using the dark strips), and various plotting and profiling options. These were used in near-real time to examine the data for instrumental issues and to validate test results.

4.2. Dark Level

The measured signal in a CCD image in the absence of incident photons is the sum of three major components: (1) dark current from thermal electrons, (2) an electronic offset, or bias, of ~240 DN intentionally added to the readout to prevent occurrence of negative values which would be quantized to zeroes in the 8- or 12-bit unsigned DN words, and (3) noise picked up by instrument electronics. Throughout calibration, there has not been evidence of picked up noise. In the following discussion, the sum of dark current and bias is treated together as "dark level." The response of pixel-dependent dark level to temperature and exposure time was investigated separately for the NAC and WAC without on-chip binning ("not-binned") and with on-chip binning.

4.2.1 Response of the Sensor System to Exposure Time and Temperature

Characterization of the WAC and NAC dark level was conducted over the temperature range 25°C to -40°C. Temperature is measured at several locations in the WAC and NAC systems, with sensors affixed to the backs of each of the CCD mounting plates. Exposure times during the tests ranged from 1 to 9001 msec. Figure 29 details the conversion from CCD temperature counts to degrees Celsius.

Figure 30 shows dark image-means for the NAC and WAC not-binned and binned, as a function of exposure time and temperature counts. In the NAC not-binned data, at short exposure times and low temperatures at which the dark level is dominated by bias, the image mean decreases with increasing temperature. This relationship is believed to originate in the amplifiers in the read-out electronics, which become more sensitive at low temperatures, and in power supply filters. Switching pulses are sent from the power supply to the sensor electronics to initiate image acquisition. The switching pulses would, for short times, increase the overall signal levels and, hence, the measured DNs. Filters in the power supply lines dampen these short time-scale effects. As exposure time increases, so does the effectiveness of the filters, and the dark current contribution becomes more evident. At longer exposure times (>200 ms) and higher temperatures (>1070 temperature counts) at which the effects of dark current dominate, the NAC not-binned shows the expected behavior of increasing dark level with increasing temperature exposure time. With on-chip binning, which works by summing the outputs of 4 pixels prior to addition of bias, the impact of the dark current is larger, and the onset of increasing dark level with temperature and exposure time occurs at lower temperature and shorter exposure time.

WAC dark levels are dominated by the increase in dark current with higher temperature and longer exposure time.

4.2.2. Dark Models

For the purpose of modeling dark current, the WAC and NAC were treated as four different instruments: NAC not-binned, NAC binned, WAC not-binned, and WAC binned. Two dark models were derived from the OCF calibrations, for each of the four modeled sensors: (1) a forward model of the dark current as a function of column number, row number, exposure time, and CCD temperature count, and (2) a backward model that uses the row-dependent dark levels in the dark strips, and extrapolates them across the FOV using the same variables as the forward model. For both the forward and backward models, dark level is treated as a linear function of column number, row number, and exposure time. The exponential temperature dependence was approximated with a third-order polynomial for ease of calculation. While it is known that the CCD temperature response will change with MET due to exposure to radiation in space, this specific time dependence will need to be determined while the sensors are en-route to Mercury.

Forward Model. An overview of the forward dark model is illustrated in Figure 31. Consider the first of four variables to the dark model: column position x, row position y, exposure time τ, and temperature T. For the column-dependence at a particular row, exposure time, and temperature, dark level is modeled linearly where an offset $\alpha(y, \tau, T)$ is the value at column x=0, and a slope $\beta(y, \tau, T)$ is the increase per column (per increment of x). Then, to find the dark level at a given column, the model for this row, exposure time, and temperature is:

$$Dk(x, y, \tau, T) = \alpha(y, \tau, T) + \beta(y, \tau, T)*x \quad [2]$$

However, the column-dependence will vary with row, so that in the second level of the model, the offset α and slope β are each a function of row position y. Thus, linear expansions of α and β are:

$$\alpha(y, \tau, T) = A(\tau, T) + B(\tau, T)*y \quad [3]$$

$$\beta(y, \tau, T) = M(\tau, T) + N(\tau, T)*y \quad [4]$$

The offset α to the column-dependent dark level has a value $A(\tau, T)$ in row y=0, and in each subsequent row y+1 that is incremented by slope $B(\tau, T)$. Similarly, the slope to column-dependent dark level β changes with each row by an offset $M(\tau, T)$ and slope $N(\tau, T)$.

But note that at this level, the row-dependences of column-dependences are themselves dependent on exposure time and temperature. Thus in a third level to the model, $A(\tau, T)$, $B(\tau, T)$, $M(\tau, T)$, and $N(\tau, T)$ can each be expressed as it own linear function of exposure time τ, using a temperature-dependent offset C(T), O(T), E(T), or Q(T) respectively, and a temperature-dependent slope D(T), P(T), F(T), or S(T) respectively:

$$A(\tau, T) = C(T) + D(T)*\tau \quad [5]$$

$$M(\tau, T) = O(T) + P(T)*\tau \quad [6]$$

$$B(\tau, T) = E(T) + F(T)*\tau \quad [7]$$

$$N(\tau, T) = Q(T) + S(T)*\tau \quad [8]$$

So, the expanded dark model at this level is:

$$Dk(x, y, \tau, T) = C(T) + D(T)*\tau + (E(T) + F(T)*\tau)*y + (O(T) + P(T)*\tau + (Q(T) + S(T)*\tau)*y)*x \quad [9]$$

At the fourth and final level of the model, C(T), D(T), E(T), F(T), O(T), P(T), Q(T), S(T) are all third-order functions of temperature, for example:

$$C(T) = H_0 + H_1 * T + H_2 * T^2 + H_3 * T^3 \quad [10]$$

The forward dark current model was derived by first finding a linear fit of dark level as a function of column number for each row in the dark calibration data (equation 2). Second, the bias and dark DN accumulation rate per column increment were fitted linearly as function of row (equations 3-4). A, B, M, and N were fitted as functions of exposure time, from data binned into fifteen CCD temperature count bins (each bin 10 DN wide) covering the range 1000-1150, or, -40.8° to -6.8°C (equations 5-8). Finally, the linear fit coefficients as a function of exposure time were fitted across the temperature bins with a third-order polynomial (equation 10).

The coefficients of these expansions are given in Table 6 for the four sensor models. Post-launch, these coefficients will serve as the bias for the MET dependence of the dark model, with the slopes to be calculated post-launch.

To assess accuracy of the model, the fitted model was differenced from the data used to create it, and the RMS errors between the data and model were measured. Figure 32 shows that, for all four sensor models, over the expected range of temperatures and for exposure times of 1200 ms or less, the RMS difference between the dark current models and the data used to derive them is coimparable to the read noise for each CCD (~1 DN for the WAC, ~2 DN for the NAC).

Backward Model from Dark Columns. Figure 33 shows the location of scene and dark columns on the NAC and WAC CCDs (both are identical). In the not-binned mode for either the WAC or NAC, the first four columns of each image are taken from a region of the CCD that is never exposed to light and, thus, represents a dark level that is purely a function of bias and dark current. The dark columns are separated from the image section by five isolation columns to avoid diffusion of signal from the active area. When the image is read-out, these four columns are mapped into the first four imaging columns, so the resulting image is a square 1024 by 1024 pixels, with four dark columns. The four dark columns behave identically to the scene as a function of row, exposure time, and temperature to within 0.26 DN.

However for the binned modes of both cameras, and error in programming the Actel field-programmable gate arrays (FPGAs) that execute the binning resulted in a different sampling of the CCDs. In binned mode, the offset to the isolated dark columns was miscalculated, and the first dark column is actually derived from an inactive portion of the CCD. The second dark column is an average of an inactive column and the first dark column in the dark strip. The sampled dark column is not one of the four read out for the not-binned images, but it does show a temperature- and exposure-time response that can be modeled, making it a

functional "dark" column albeit with lower response. So, for the dark level from dark column model, the second column (binned or not-binned) was taken to be representative of the dark strip properties and used accordingly.

For the dark level from dark column model, the same procedure was used as for the dark current model, with the following exception. The bias for the fit to each row as a function of column number was defined to be the value of the fit to the dark column at that row number. Then, the regression error for a range of accumulation rates assuming this fixed bias was calculated. The accumulation rate minimizing the regression error was used as the accumulation rate of each row as a function of column number. From this set of coefficients, the exposure time dependence and the temperature bins were derived, and, as above, the RMS error of fit regressions calculated. Since the bias derived from the dark columns is not the same as the bias derived directly from the dark current, it is expected the RMS errors will be slightly greater. For exposure times of less than 1200 msec, the RMS error for the darks from dark column model is, on average, 0.4 DN larger than the dark current model, as shown in Figure 32.

Given the initial better fit of the forward dark current model to the data, as well as the nature of the binned "dark" columns, it is tempting to rely on the dark current model exclusively. However, the dark strips, even for binned data, serve as an indicator of the variations of the CCDs' response to radiation, and, as such, a means to calibrate the changes in the behavior of the CCD with MET. Thus, both dark models will be periodically re-evaluated en route to Mercury and during the orbital portion of the mission.

4.3. Frame Transfer Smear

Frame transfer smear corrections for MDIS follow the technique described for NEAR MSI image by *Murchie et al.* (1999). In brief, an image is exposed for a nominal integration time and is then transferred in 3.84 ms to a memory zone on the CCD, from which the analog signal is digitized line-by-line. Accumulation of signal continues during the finite duration of frame transfer, inducing a streak or frame-transfer smear in the wake of an illuminated object in the field of view, parallel to the direction of frame transfer. Quantitatively, the smear correction is:

$$\mathrm{Sm}(x,y,T,\tau,f,b) = \sum_{1}^{y-1} \frac{t_2}{\tau} \frac{[\mathrm{DN}(x,y,\tau,b) - \mathrm{Dk}(x,y,T,\tau,b,MET)] - \mathrm{Sm}(x,y,b,\tau)}{\mathrm{Flat}(x,y,b,f)} \qquad [11]$$

where Sm(x,y,T,τ,f,b) is the smear in column x, row y at exposure time τ and temperature T in binning mode b and filter f. Dk(x,y,T,τ,b,MET) is the dark level in column x, row y at exposure time τ and temperature T in binning mode b at mission-elapsed time MET. Flat(x,y,b,f) is the flat-field correction in column x, row y in binning mode b and filter f. τ is exposure time, and □ is the time for frame transfer (3.84 ms) divided by the number of lines in the image in the direction of frame transfer, i.e., 1024 for not-binned images or 512 for binned images. Empirically, it was found that this correction removes frame transfer smear to the level of noise in typical, field-filling scenes for which exposure time is >2 times the frame transfer time. For high-contrast scenes such aswell-exposed, non-field-filling extended source imaged against a black background, artifacts are at or below the noise when exposure time is >3 times the frame transfer time.

Figure 34 (left) shows an example of frame transfer smear for a not-binned NAC image of a light bulb filament. The image, taken at room temperature, was exposed for 5 ms, less than the guidelin above. In the corrected image (Figure 34, right) the smear is slightly overcorrected. This artifact disappears in typical scenes for exposure times ≥8 ms. Thus, for analysis of MDIS filter bandpasses (section 4.5) and ratiometry (section 4.6), only images with exposure times ≥8 ms were utilized.

4.4. Geometric Calibration

4.4.1. NAC and WAC FOV, IFOV, and Offset

To determine the fields-of-view and the relative alignment of the WAC and NAC, the output slit of the OCF monochromator was imaged using white light at different positions of the motion stage. The ends of the slit were measured from dark-corrected, desmeared images, and the pixel positions and stage positions were used to determine the IFOV, FOV, and relative pointing of each camera (Fig. 35). The angular difference per pixel position defines the IFOV, and 1024 times that value defines the FOV. The WAC FOV is 10.54°±0.02°, and the IFOV is 179.6±0.3 μrad. Assuming a 14-μm pixel pitch (specified by the manufacturer), this implies a focal length of 77.96±0.15 mm. The NAC FOV is 1.493°±0.001°, and the IFOV is 25.44±0.02 μrad, implying a focal length of 550.3±0.5 mm.

This measurement also provides information on the relative orientations of the two FOVs. The pixel positions measured at each stage position define a vector for each camera, whose angular separation defines the twist between the two FOVs. The NAC FOV is rotated relative to the WAC's by approximately 179.69° clockwise, so that a scene that appears "right-side up" in one camera and "upside down" in the other. Allowing for this twist, solving for the center pixel position in each camera in angular coordinates, and differencing the two results yields the offset in boresight positions. The two boresights are offset by 0.21°.

4.4.2. Position within Gimbal Plane

Through mechanical tolerances, deviation of the pivot plane from normal due to mechanical error is less than 85 μrad. Sampled measurements over the range of motion of the actuator are consistent with the nominal stepping of 0.0086 deg/step. We attempted to fully characterize the single step response of the pivot actuator, but found systematic effects dominating the measured response. A detailed calibration of the output angle of the pivot actuator relative to angle was measured previously (Figure 36a). Significant variations from linear are apparent. Motion is in the forward direction which for this test was defined as rotation toward the S/C sunshade (toward higher solar phase angles). Figure 36b reverses the direction. The obvious sinusoidal deviations shown in these two figures reflect the loading and backlash associated with the harmonic drive. This motion is very reproducible when moving either the forward or reverse directions, and should be correctable with a look-up table. The complication in this is that the pivot calibration started from the operational hardstop (as opposed to the stowed hard stop used by the MDIS flight software), and due to time limitations, was only characterized over 100°.

The flight software routinely does not command the pivot actuator to the operational hardstop, but halts motion at a software stop located +49.999 deg. Since the full range of motion from hardstop to hardstop is 239.7096 deg, knowledge of the motion from the home position (stowed hardstop) to some known position does permit correlation of the data shown in Figures 36a,b to pivot motion.

To establish a second known position, the pivot actuator was nominally moved to the 0 position of the actuator (apertures directed along S/C +Z-axis). This position was then mapped into the MDIS cube and also into the master alignment cube of the spacecraft. Camera boresights were previously determined in relative to the MDIS cube.

4.5. Wavelength calibration

The NAC uses a single filter, while the WAC views the scene through a filter wheel outfitted with 12 filters of varying widths. The WAC filters are labeled by their position counter-clockwise around the wheel as viewed from the CCD. Using the OCF monochromator, NAC and WAC filter transmissions were measured as a function of wavelength for temperatures ranging from -35°C (1056 CCD temperature counts) to ~26°C (1265 CCD temperature counts). The source appeared in the data as a bright rectangle in the center of each image. After subtracting the dark model from the image values and performing smear corrections, a mask was derived from each image based on bright and dark pixel distributions. The values in the mask were set to zero for the dark regions and one for the source rectangle. After multiplication, the pixel values for the resulting image were summed to achieve maximum response with varying source wavelength. A Gaussian shape was used to model almost all the WAC and NAC filter centers and widths, except for WAC filters 6 (430 nm) and 11 (1010 nm), which were modeled with a combination of Gaussian and polynomial fits. The center wavelength and bandpasses (full-width at half maximum, or FWHM) were calculated for filters 6 and 11 through a cumulative distribution technique, which is similar to a weighted average. Specifically, after normalization, the data were summed as:

$$C(\lambda_n) = \sum_0^n F(\lambda_i) \qquad [12]$$

where $C(\lambda_n)$ is the cumulative distribution to λ_n, $F(\lambda_i)$ is the filter response at wavelength λ_i, and n varies between 0 and M, the number of monochromator wavelength settings within the filter bandpass. This 50% point was defined as the center wavelength of those two filters, and the 75% and 25% points were differenced to find the filter width.

Figure 37 shows fits calculated to WAC data acquired in the OCF at -26°C (1074 CCD temperature counts), which is about the median operating temperature expected in Mercury orbit. These compare well with the manufacturer-supplied bandpasses, as shown in Table 4. Filter 2 is a clear fused silica filter spanning the entire passband of the CCD (350-1050 nm), and is not shown here. The NAC filter was measured to have a center frequency of 751 nm and a bandpass of 88 nm.

The center wavelengths shift systematically with temperature. However with the exceptions of the longest wavelength WAC filter (11), in which the bandpass is affected by temperature effects on the response of the CCD itself, they agree with the nominal values to within 2 nm. Figure 38 shows the difference between filter center wavelengths at temperatures from their values at 1074 CCD temperature counts (-26°C). The scatter in the wavelength offsets at the lower temperature (1056 counts) should be considered as measure of the precision of determining the center wavelength (±0.5 nm). All filters show the expected shift to longer wavelengths with increasing temperature. Filter 11 has a greater shift than the rest of the filters, due to enhanced long-wavelength response of the CCD at higher temperatures. Figure 39 shows fitted measurements for an example passband, the WAC 750 nm filter (#7), and how the bandpass shifts with temperature.

4.6. Responsivity, Response Linearity, and Response Uniformity

Calibration of the signal accumulation rate per unit time per unit at-sensor radiance was conducted in the OCF for the WAC and the NAC over a broad range of exposure times and source light intensities. The exposure times to saturation were determined empirically in initial set-up. Then, under varying temperatures (-34ˆC to 25ˆC) and source intensities, images were acquired in pseudo power-of-two time steps (e.g., 1, 2, 4, 8, 15, 30, 50, 100 ms, etc.) until saturation was reached. In addition, source intensities were stepped in a fixed decreasing-light pattern through eight levels that could be achieved with the integrating sphere's two 150-W and two 45-W bulbs. Initial testing of the sphere indicated that the halogen bulbs needed several hours of warm-up before asymptotically approaching constant light output. So, for the WAC, the calibration procedure was to begin with all lamps on, wait until constant output, and then begin taking data, turning off lamps in sequence, each time repeating the pseudo power-of-two steps in exposure time for each filter. For the NAC, this sequence needed to be executed only once for its single filter.

When the instruments were mounted in the OCF vacuum chamber, the sphere opening was smaller than the portal door and did not fill the FOV of the WAC when the sphere was set back from the vacuum chamber. For room temperature, ambient pressure measurements, the portal door was opened, and the sphere moved forward until the opening rested against the portal. Light then filled the field of view. For cold temperatures and reduced atmospheric pressures, this was impossible, as the vacuum chamber was, of necessity, required to remain sealed. For these data, the sphere opening does not fill the field of view, but was centered in the FOV.

4.6.1. Response Linearity

Linearity is the measure of how variable is each camera's DN level per unit exposure time and radiance, as a function of variation in exposure time or radiance. Using dark-corrected, desmeared DN values (DCDSI) taken from the center quarter of the images, response linearity was measured with both the NAC and WAC binned and not-binned. Linearity was first examined separately for (a) linearity with respect to exposure time at individual light levels, and (b) linearity with respect to radiance at individual exposure times. The results are not significantly different, so all data were merged to examine linearity with respect to measured

photons (radiance times exposure time). For each filter, the response was normalized to unity at a reference dark-corrected, desmeared DN level of 2000.

Figure 40 shows a representative result for linearity with respect to accumulated photons, for the NAC at room temperature (1260 CCD temperature counts). Error bars represent residuals from the dark-correction model discussed in section 4.2. Due to the 2-10% uncertainties at DN levels <500 introduced by the high dark current, determination of system linearity is not possible with a high degree of confidence at room temperature.

Figures 41 and 42 show WAC not-binned linearity at two different cold temperatures, 1046 CCD counts (~-34°C) and 1060 counts (~-30°C). To illuminate system-wide trends in the WAC, the results from the narrowband filters in the center of the CCD passband (filters 1, 3, 5, 7-10, and 12) are plotted without distinction. The lower dark current at cold temperatures results in much smaller uncertainties, allowing linearity to be measured to the 0.5-1% level. At corrected DN levels >1000, the system is linear to within the error bars. However, at both temperatures, there is a decrease in response at lower DNs, by up to 2% at the lowest DN levels. All filters show the same behavior.

Binned WAC linearity was measured only with respect to exposure time at a few exposure times, and only for filter 1 (699 nm) and one radiance level. The DN accumulation rate in this case was, as expected, 4 times the values for the not-binned WAC using the same bulbs and exposure times. Linearity as a function of corrected DN is similar, but this is based on only a few data points.

NAC linearity at low temperature is shown for not-binned (Figure 43) and binned (Figure 44) cases. Both exhibit the same behavior, which is subtly different from that of the WAC. Linearity is flat above a corrected DN of ~1000 but decreases below that; however, the value at low DN levels falls by up to 4% as opposed to 2% in the WAC.

For an ideal CCD, response relative to the reference DN of ~2000 should be unity for all corrected DN levels. The instrument specification had been ±1%. However, in the low-temperature measures representative of flight conditions, linearity falls off below ~1000 DN but up to 2-4%. For calibration of flight data, this will necessitate usage of a linearity correction either analytically or using a look-up table.

4.6.2. Responsivity

Responsivity is the dark-corrected, desmeared DN per unit time per unit radiance at the reference DN. Integrating-sphere radiances were calibrated by Labsphere using each of the four lamps separately, over a wavelength range of 350-1100 nm in 5-nm steps. To determine radiances through each of the WAC and NAC filters, the bandpasses described in section 4.5 were convolved with the sphere's spectral radiance. For data taken at room temperatures, the chamber door was open, but for lower-temperature measurements the sphere was viewed through the quartz window in the OCF chamber door. Therefore for the low temperature data, an additional correction was applied to the sphere radiance for each filter to account for the window.

This was derived from room temperature data, as the ratio of corrected DNs per unit time with the door closed to that with the door open, for a single configuration of sphere bulbs.

Figures 45 through 47 show the responsivities measured for each filter for the not-binned WAC at a range of radiances and exposures, for three different temperatures. Data points are represented by crosses, which have widths showing 2-σ errors of the dark model and heights showing 2-σ errors in responsivity. Each line connects the responsivities measured at a single sphere radiance through a single filter at different exposure times. For each filter, the data overlay to within the errors in the dark model. Figure 48 shows the temperature dependence of the not-binned WAC responsivities for each filter, normalized to the value at 1060 CCD counts, or -30.25°C. For these data, differences between -30°C and -34°C at wavelengths <700 nm are assumed to be a measure of systematic errors. (No significant temperature-dependence of responsivity is expected in these filters at that temperature range.) For the binned WAC, responsivity is greater than not-binned WAC responsivity by a factor of 4.0.

Figures 49 and 50 show the responsivities measured for the NAC at cold temperatures. Data points are represented by crosses, which have widths showing 2-σ errors of the dark model and heights showing 2-σ errors in responsivity. Each line connects the responsivities measured at a single sphere radiance through a single filter at different exposure times. Note the highly exaggerated scale; the scatter in the determinations is only about 4%, which is a measure of the absolute accuracy of the radiometric calibration.

Table 7 summarizes the responsivities of the NAC and WAC, both binned and unbinned, at a reference temperature of 1060 CCD counts, or -30.25°C. It is expected the temperature-dependence of responsivity over the temperature range shown will be approximmately quadratic. However measurements at intermediate temperatures , e.g. -10°C, were made onground. Therefore the best correction available from ground data is linear in form, and a second-order correction will have to be determined from targets of opportunity inflight (e.g., Canopus from Mercury orbit, at which time the CCD temperature will vary over its operational range). The application of the linear correction is:

$$\mathrm{Resp}_{f,T} = \mathrm{Resp}_{f,-30.3°C} * (\mathrm{correction\_offset}_f + \mathrm{temperature\ counts} * \mathrm{correction\_slope}_f) \quad [13]$$

where $\mathrm{Resp}_{f,T}$ is responsivity in filter *f* at temperature T in units of CCD counts, $\mathrm{Resp}_{f,-30.3°C}$ is reponsivity in filter f at 1060 CCD counts or -30.25°C as given in Table 7, and $\mathrm{correction\_offset}_f$ and $\mathrm{correction\_slope}_f$ are camera- and filter-dependent temperature correction offset and slope also as given in Table 7. The temperature correction defaults to unity at the reference temperature of 1060 CCD counts or -30.25°C.

4.6.3. Response Uniformity (Flat Field)

Response uniformity, or flat field, is a measure of pixel-to-pixel variations in responsivity. Measurements of response uniformity of the WAC and NAC were conducted in the OCF, at room temperature and while cold, by imaging the integrating sphere with the two 45W bulbs illuminating the interior.

Figure 51 shows a 200 ms exposure binned WAC image acquired through the OCF portal door. Note that the OCF chamber window is smaller than the WAC FOV. Four significant non-uniformities are evident in the data: (1) bright patches around the rim of the sphere opening, nicknamed "clouds," (2) a slight falloff in brightness with field angle from near the center of the FOV, (3) slight horizontal striping, and (4) darker spots scattered across the FOV. The clouds are believed to be reflections of the integrating sphere off the radiator and thermal blankets that were mounted on the instrument in the chamber, back off the window, and into the imagers. Removing the thermal blankets in later tests significantly reduced the clouds. The falloff in brightness with angular distance from the center of the FOV (Figure 52) is the expected $\cos^4$ falloff in response with field angle off the optic axis. The horizontal striping is a function of the binning, and is absent in the not-binned imagery.

The darker spots scattered across WAC images are fixed with respect to the CCD regardless of filter wheel setting, though their intensities do vary slightly with filter. The sizes of the spots are consistent with shadows of <<35-μm dust on the CCD cover, and their number density is consistent with the standards for a class-10,000 clean room in which the camera was assembled. Also consistent with this hypothesis, following instrument vibration during environmental testing, the locations of several spots changed. With the exception of a single particle (the black spot in the right center of Figure 51), the dust spots do not significantly affect the DN levels. Given this result, it is likely that the spots themselves will move as the instrument is subjected to the vibrations of launch and flight. Images of the venusian cloud tops acquired during the Venus flybys will be used to redetermine the flat field post-launch.

To avoid issues of reflections in the OCF facility contaminating flat field determinations, and to avoid having to construct the WAC flat field from mosaicked data, it is desirable to determine the flat field at room temperature with the door open and the aperture of the camera at the integrating sphere aperture. To reduce noise in the derived flat field to approximately 10^{-3}, ~100 images have to be averaged together per filter, camera, and binning mode. Figures 53 and 54 compare the central portions of binned, corrected, and averaged WAC integrating sphere images acquired at room temperature and at cold temperature. When the images are dark-subtracted, desmeared, averaged, and normalized to the image mean, the relative DN levels are nearly identical on a pixel-by-pixel basis. Since the data are in good quantitative agreement regardless of physical temperature, the flight flat-fields are derived from room temperature, door-open images.

Not-binned and binned flat fields are shown in Figures 55 and 56 respectively. The values are normalized to unity in the central part of the images used for responsivity determinations, so that updates to responsivity from non field-filling sources and to flat field from field-filling sources can be decoupled. The NAC flatfield is shown in the upper right panel in both figures, and the 11 narrow-band WAC filters are shown in the remaining panels. Spots on the NAC images are not from dust, but instead are from refraction at imperfections in the glass covering of the CCD. Because they are immobile relative to the detector, redoing the NAC flat field inflight is not a requirement for the NAC as it is with the WAC.

4.7. Point-Spread Function

The point spread function, or PSF, is a measure of the two-dimensional distribution of at-sensor radiance emanating from a point source. For a conceptual but non-physical imager, light emanating from a point would all fall into a single detector element. In practice the PSF is broadened by diffraction, surface imperfections of optical elements, or scatterers on optical surfaces. In the particular case of the NAC, the PSF is signficantly broader than if the system were diffraction-limited at the NAC focal length, because mass constraints on MDIS required under-sizing of the aperture. The expected size of the Airy disk (approximately, the FWHM of the PSF including only effects of diffraction) is >2 pixels. For nadir imaging at high southern latitudes, this degradation will limit effective sampling of the surface to significantly worse than the 250 m/pixel desired spatial sampling.

The approach adopted for the NAC was to characterize carefully the PSF during ground testing, and use Fourier image restoration techniques (optimal filter) to improve the PSF during calibration. A similar strategy was applied to NEAR images to remediate PSF degradation of contaminants on the imager's optics (*Li et al. (2002)* The optimal filter deblurring algorithm can be presented as:

$$I = \mathrm{C} * F \cdot \| H \|^2 / [H(\| H \|^2 + \mathrm{K})] \qquad (14)$$

where I is the deblurred image, F is the original, calibrated image in units of radiance, H is the PSF, $\| H \|$ is the norm of complex number H (the square root of the sum of the squares of the real and imaginary parts of H), K is an empirically determined noise constant, and C is an empirically determined constant that maintains radiometric accuracy (refernce source of eqn – look in Li et al). K is determined as a value that provides the most sharpening of an image before "ringing" is introduced at abrupt bright-dark boundaries. The output of the correction is in arbitrary units that are directly proportional to the input units of radiance, so C is the ratio of the summed pixel values in the original and deblurred images.

For the deblurring procedure to work effectively, C and K must be validated across a variety of scenes, and the PSF must be both well determined and nearly constant across an image. In the case of the NEAR imager, these constraints were all satisfied. There is no requirement, however, that the PSF be radially symmetric about its central pixel. In fact, with the NEAR imager the PSF had a slight coma (it was extended diagonally in one direction), and early attempts to impose an average radial symmetry yielded an inferior result to the actual, asymmetrical PSF (I politely assert that you are mistaken!). The effectiveness of the procedure is shown in Figure 57, which compares a NEAR color composite image of Eros before and after the three image planes (red, green, and blue images) were deblurred.

For the NAC, the PSF was assembled from images of a sub-pixel scale pinhole (larger or smaller than a pixel?) imaged in white light at the focus of the OCF collimator. Multiple exposure times were used, the lowest of which is unsaturated, and the longer of which are progressively more saturated. At each exposure time, multiple images are acquired. After correction for dark level, frame transfer smear, and flat-field non-uniformity, the images are divided by exposure times to convert to units of DN/ms and coregistered. The multiple images at each exposure time are averaged to improve statistics. Starting with the longest exposure,

saturated parts of the corrected, averaged image are zeroed out, and replaced with unsaturated parts of the next longest exposure. The procedure is continued until the central pixel is reached, and finally all values are normalized to that of the central pixel. This procedure to assemble the PSF is repeated over a 3x3 grid of positions within the FOV (center, corners, and edges) to assess uniformity of the PSF across the FOV.

Figure 58 shows the 3x3 grid of NAC PSFs, displayed using a linear stretch between 0 and 1. The brightest part of the PSF exhibits its expected 2-3 pixel diameter, and the PSF is closely similar across the FOV; there is no evidence for shapes of the PSF that are related to position or distance relative to the optic axis. Figure 59 shows the PSFs similarly, except displayed using a logarithmic stretch between 10^{-6} and 1. Shape of the PSF is well determined out to a radius of 10 pixels. The shape is not exactly radially symmetric, but it does appear nearly uniform across the FOV. Thus, the measured NAC PSF appears perfectly suited to application of the optimal filter to improve effective spatial sampling of Mercury in the NAC.

5. DATA PRODUCTS

The MESSENGER project will archive all MDIS Experiment Data Records (EDRs) and Reduced Data Records (RDR) with the Planetary Data System (PDS) in a timely fashion (Table 8). EDRs consist of the raw image data (instrument counts) fully documented in terms of geometric and radiometric variables. In addition to the raw images, the MESSENGER project will also archive radiometrically corrected versions in units of I/F or radiance, as appropriate. The information contained in this paper and prelaunch calibration files archived with the PDS will allow a user to apply any advances to state of calibration as needed to the original raw EDRs.

Critical science observations will be obtained during the three Mercury flybys and are of four basic types:

- quadrature monochrome NA camera mosaics (200 m/pixel to 600 m/pixel)
- medium resolution NA camera quadrature stereo mosaics
- synoptic 11-color mosaics (1 to 8 km/pixel)
- approach and departure movies (4.4 to 18 km/pixel).

Data products from these observations will serve as the foundation for assessing the orbital mapping strategy and planning special targeted high-resolution sequences. RDR products associated with the flyby observations will be reviewed and archived with the PDS on the same schedule as the EDRs.

During orbital operations systematic mapping with both the NA camera and WA camera will result in:

- a global monochrome basemap with an average resolution of 250 m/pixel
- merged flyby and orbital multispectral cubes and mosaics in up to 11 spectral filters at ~1 km/pixel
- local stereo-based digital elevation models

- very-high-resolution NAC local strip mosaics in the northern hemisphere (best resolutions ~20 m/pixel)

REFERENCES

Basaltic Volcanism Study Project, *Basaltic Volcanism on the Terrestrial Planets*, Pergamon Press, New York, 1286 pp., 1981.

Benz, W., W.L. Slattery, and A.G.W. Cameron, Collisional stripping of Mercury's mantle, *Icarus*, 74, 516-528, 1988.

Blewett, D. T., Lucey, P. G., Hawke, B. R., Ling, G. G., and Robinson, M. S., A comparison of mercurian reflectance and spectral quantities with those of the Moon, *Icarus*, 129, 217-231, 1997.

Cameron, A.G.W, Fegley, B., Jr., Benz, W., and Slattery, W.L., The strange density of Mercury: Theoretical considerations, In *Mercury* (F. Vilas, C. R. Chapman, and M. S. Matthews, eds), University of Arizona Press, 692-798, 1988.

Cintala M.J, Impact-induced effects in the lunar and mercurian regoliths, *Jour. Geophys. Res*., 97, 947-973, 1992.

Cordell, B.M. and R.G. Strom, Global tectonics of Mercury and the Moon. *Phys. Earth Planet. Inter.,* 15, 146, 1977.

Dzurisin, D. The tectonioc and volcanic history of Mercury as inferred from studies of scarps, ridges, troughs and other lineaments, *Jour. Geophys. Res.*, 83, 4883-4906, 1978.

Fegley,B., Jr., Cameron, A.G.W., A vaporization model fro iron/silicate fractionation in the Mercury protoplanet, *Earth and Planet. Sci. Lett*., 82, 207-222, 1987.

Goettel, K. A., Present bounds on the bulk composition of Mercury: Implications for planetary formation processes, In *Mercury* (F. Vilas, C. R. Chapman, and M. S. Matthews, eds), University of Arizona Press, 613-621, 1988.

Gold, R.E., R.L. McNutt, S.C. Solomon, and the MESSENGER Team, The MESSENGER science payload, 2003.

Hapke B, C. Christman, B, B. Rava, J. Mosher, A color-ratio map of Mercury, *Proc. Lun. and Planet. Sci. Conf*., 11, 817-821, 1980.

Harmon, J. K., and M. A. Slade 1992. Radar mapping of Mercury: Full-disk images and polar anomalies. *Science* **258**, 640–643.

Heiken, G.H., D.T. Vaniman, B.M. French, *Lunar Sourcebook A User's guide to the Moo*n, Cambridge University Press, New York, New York, 1991.

Keiffer, W.S. and B.C. Murray, The formation of Mercury's smooth plains, *Icarus*, 72, 477-491, 1987.

Lewis, J. S., Metal/silicate fractionation in the solar system, *Earth Planet. Sci. Lett*. 15, 286-290, 1972.

Lewis, J. S., Chemistry of the planets, *Ann. Rev. Phys. Chem.* 24, 339-351, 1974.

Lewis, J. S., Origin and composition of Mercury, In *Mercury* (F. Vilas, C. R. Chapman, and M. S. Matthews, eds), University of Arizona Press, 651-666, 1988.

Li, H., M. Robinson, and S. Murchie, Preliminary remediation of scattered light in NEAR MSI images, *Icarus*, *155*, 244–252, 2002.

Melosh, H.J., and D. Dzurisin, Mercurian global tectonics: A consequence of tidal despinning?, *Icarus, 35,* 227-236, 1978.

Melosh, H.J., and W.B. McKinnon, The tectonics of Mercury, in *Mercury*, edited by F. Vilas, C.R. Chapman, and M.S. Matthews, 374-400, 1988.

Melson, W. G., Vallier, T., Wright, T. L., Byerly, G., and Nelen, J., Chemical diversity of abyssal volcanic glass erupted along Pacific, Atlantic, and Indian Ocean sea-floor spreading centers, In *The Geophysics of the Pacific Ocean Basin and Its Margins*, 351-367, 1976.

Morgan, J. W. and Anders, E., Chemical composition of Mars, *Geochim. Cosmochim. Acta*, 43, 1601-1610, 1979.

Murchie, S., M. Robinson, S. E. Hawkins III, A. Harch, P. Helfenstein, P. Thomas, K. Peacock, W. Owen, G. Heyler, P. Murphy, E. H. Darlington, A. Keeney, R. Gold, B. Clark, N. Izenberg, J. F. Bell III, W. Merline, and J. Veverka, Inflight calibration of the NEAR multispectral imager, *Icarus* 140, 66-91, 1999.

Murray, B.C., The Mariner 10 pictures of Mercury, *Jour. Geophys. Res.*, 80, 2342-2344, 1975.

Murray, B.C., R.G. Strom, N.J. Trask, D.E. Gault, Surface history of Mercury: Implications for terrestrial planets, *Jour. Geophys. Res.*, 80, 2508-2514, 1975.

Pechmann, J.B., and H.J. Melosh, Global fracture patterns of a despun planet: Application to Mercury, *Icarus, 38*, 243-250, 1979.

Potter, A. and T.H. Morgan, Discovery of sodium in the atmosphere of Mercury, *Science*, 229, 651-653, 1985.

Potter, A. and T.H. Morgan, Potassium in the atmosphere of Mercury, *Icarus*, 67, 336-340, 1986.

Rava, B., and B. Hapke, An analysis of the Mariner 10 color ratio map of Mercury, *Icarus, 71*, 397-429, 1987.

Robinson, M.S. and P.G. Lucey, Recalibrated Mariner 10 color mosaics: Implications for mercurian volcanism, *Science*, 275, 197-200, 1997.

Robinson, M.S. and J.G. Taylor, Ferrous oxide in Mercury's crust and mantle, *Meteoritics and Planetary Science*, 36, 841-847, 2001.

Slade, M. A., B. J. Butler, and D. O. Muhleman, Mercury radar imaging: Evidence for polar ice, *Science*, 258, 635–640, 1992.

Solomon, S.C., R.L. McNutt, R.E. Gold, M.H. Acuna (need squiggly over n), D.N. Baker, W.V. Boynton, C.R. Chapman, A.F. Cheng, G. Gloeckler, J.W. Head III, S.M. Krimigis, W.E. McClintock, S.L. Murchie, S.J. Peale, R.J. Phillips, M.S. Robinson, J.A. Slavin, D.E. Smith, R.G. Strom, J.I. Trombka, M.T. Zuber, The MESSENGER mission to Mercury: scientific objectives and implementation, *Planetary and Space Sciences*, 49, 1445-1465, 2001.

Spudis, P.D. and J.E. Guest, Stratigraphy and geologic history of Mercury, In *Mercury* (F. Vilas, C. R. Chapman, and M. S. Matthews, eds), University of Arizona Press, 118-164, 1988.

Strom, R.G., Origin and relative age of lunar and mercurian intercrater plains, *Phys. Earth and Planet. Sci.*, 15, 156-172, 1977.

Strom, R.G., N. J. Trask, and J. E. Guest, Tectonism and volcanism on Mercury, *J. Geophys. Res.,* 80, 2478-2507, 1975.

Trask, N.J. and J.E. and Guest, Preliminary geologic terrain map of Mercury, *J. Geophys. Res.*, 80, 2462-2477, 1975.

Vilas, F., Surface composition of Mercury from reflectance spectrophotometry, In *Mercury* (F. Vilas, C. R. Chapman, and M. S. Matthews, eds), University of Arizona Press, 59-76, 1988.

Vilas, F., C.R. Chapman, and M.S. Mathews, *Mercury*, University of Arizon Press, Tucson, AZ, 794 pp., 1988.

Weidenshilling, S. J., Accretion of the terrestrial planets. II, *Icarus*, 27, 161-170, 1976.

Wetherill, G. W., Accumulation of Mercury from planetesimals, In *Mercury* (F. Vilas, C. R. Chapman, and M. S. Matthews, eds), University of Arizona Press, 670-691, 1988.

Wetherill, G.W., Provenance of the terrestrial planets, Geochimica Cosmochimica Acta, 58, 4513-4520, 1994.

Wilhelms, D.E., Mercurian volcanism questioned, *Icarus*, 28, 551-558, 1976.

Table 1. Key parameters describing the three MESSENGER Mercury Flybys, all closet approach (CA) latitudes are equatorial (0°) and range is listed in kilometers, closest approach occurs on the night side of the planet in all three flybys. The columns "In Lon" and "Out Lon" indicate sub-spacecraft point at 20,000 km range during the inbound and outbound legs of the respective flyby. Comments indicate portion of Mercury imaged during respective flyby (Caloris=Caloris Basin, EUH=eastern half of unseen hemisphere, WUH=western half of unseen hemisphere, MG=Mariner 10 Gore). All longitudes reported in positive-west planetographic. During the three Mariner 10 flybys Mercury was illuminated from 10°W to 190°W.

Date	CA Range	CA Lon	Inbound Lon	Outbound Lon	Illuminated Lon.	Key Features
1/14/08	2640	320°	52°	228°	84° to 264°	Caloris, EUH
10/06/08	2640	130°	224°	36°	266° to 86°	Kuiper, WUH, MG
09/29/09	2640	148°	252°	45°	270° to 90°	Kuiper, WUH, MG

Table 2. Mercury flyby imaging plan.

Flyby observations			Approx. minutes duration	Filters	Pixel binning	Compr-ession ratio	Bits/ pixel	Cum. Gb, uncompressed	Cum. images	Cum. Gb, compressed
Description	km/ pixel	Start time.								
Approach opnavs		E-30 hr		1	-	1	12	0.06	6	0.08
Approach movie		E-30 hr		1	-	12	8	0.21	36	0.10
Approach color image	5	E-80 min		11	-	2	12	0.32	47	0.17
Approach mosaic	0.5	E-55 min	3.23	1	-	8	8	0.52	87	0.21
High-resolution 1 mosaic	0.06	E+13 min	4.88	1	-	8	8	0.82	147	0.27
High-res. color mosaic	1	E+20 min	1.90	11	-	2	12	1.78	246	0.90
Color photometry *	various	various		11	2x2	2	12	2.02	345	1.05
High-resolution 2 mosaic	0.2	E+25	12.89	1	-	8	8	2.80	499	1.22
Departure color mosaic	2	E+40 min		11	-	2	12	3.76	598	1.84
1st departure mosaic	0.4	E+50 min	8.27	1	-	6	8	4.26	697	1.98
2nd departure mosaic	0.5	E+60 min	8.27	1	-	6	8	4.76	796	2.12
Departure color image	5	E+80 min		11	-	2	12	4.87	807	2.19
3rd (stereo) mosaic	0.7	E+87 min	2.83	1	-	6	8	5.05	842	2.24
4th (stereo) mosaic	0.8	E+93 min	2.83	1	-	6	8	5.22	877	2.29
Departure opnavs		E+100 min		1	-	1	12	5.28	883	2.36
Departure movie		E+100 min		1	-	12	8	5.43	913	2.38

* Same spot at phase angles 50°-130° in 10° increments.

Table 3a. Derived MDIS requirements and as-built performance for field-of-view, pointing, and spatial resolution. Underlined items incur additional data processing or revisions to the data acquisition strategy to meet requirements, as indicated. (Global map is variously listed as 500, 250, and 150 m/p in text and table – yellow highlight means point not clear)

Measurement Objective	Measurement Requirement	Instrument / s/c Requirement	As-built Performance	Method of Verification
Flyby near global monochrome map at 500 m/pixel	Image Mercury outbound on both flybys; maximize area imaged in orbit at near-0° emission angle	Point from boresight to >40° antisunward, >50° sunward maintaining unobstructed FOV	Unobstructed FOV to 64° antisunward, 52° sunward using gimbal and s/c slew	By design
Provide optical navigation support for Mercury flybys	OpNavs earlier than c/a-2.5 dys at flybys	Availability of imaging at 31°-142° phase angles at center of FOV, from combination of pivoting and spacecraft slewing, provides: • NAC imaging at E-6.0 dys @ flyby 1, E-3.7 dys @ flyby 2, E-7.2 dys @ flyby 3 • WAC imaging at E-7.0 dys @ flyby 1, E-4.7 dys @ flyby 2, E-8.0 dys @ flyby 3		Trajectory analysis
Near-nadir global monochrome map at 250 m/pixel	FOV wide enough for cross-track continuity, avg. dayside altitude	>9.3° WAC FOV for baseline orbit (>160 µrad pixel)	10.5° WAC FOV (179 µrad pixel)	Geometric calibration
	Cross-track continuity maintained at lowest altitudes using pivoting of FOV	1.2°/sec pivot rate to stagger WAC FOVs to produce 15° wide composite image strips	1.2°/sec	Gimbal testing
	Acquire image strips without cross-track gores or excessive cross-track overlap	Acquire rectangular subframes at up to 1 Hz to manage downlink volume	Arbitrarily defined rectangular subframes available at 1 Hz	Spacecraft functional testing
	<250 m/pixel sampling, globally, with low emission angle.	WAC and NAC IFOVs provide <250 m/pixel average sampling for nominal orbit	140 m/pixel average sampling of surface at optimal lighting	Coverage simulations
		WAC and NAC PSF support sampling at <2x average requriement	Projected FWHM of NAC PSF ~700 m in southern high latitudes; onground PSF measurement to be used for image restoration	Radiometric calibration and analytical modeling
		Main processor and downlink volume allow average spatial resolution of binned pixels <250 m/pixel with moderate compression	25.9 Gb MDIS d/l allocation allows d/l of 140 m/pixel using 8:1 compression; MP loading requires on-chip 2x2 binning for portion of data, degrading resolution by TBD up to 2x	Coverage and spacecraft performance simulations
	Point with sufficient accuracy to allow mosaicking with <10% image overlap	<0.15° pointing accuracy for spacecraft to maintain <10% NA image overlap	0.02° pointing accuracy for spacecraft; 0.03° including 1-σ uncertainty	Simulation based on uncertainties from component tests
		<0.15° step for MDIS pivot mechanism	0.0096° step for MDIS pivot mechanism	By design

Table 3b. Derived MDIS requirements and as-built performance for spacecraft slewing, stability, memory, downlink (in 3a Flyby 500 came before Orbital 250).

Measurement Objective	Measurement Requirement	Instrument / s/c Requirement	As-built Performance	Method of Verification
Near-nadir global monochrome map at 250 m/pixel	Roll spacecraft sufficiently rapidly to track nadir at the minimum 200-km orbital altitude	1.35 mrad/sec	1.7 mrad/sec	Spacecraft functional testing
	Ability to track nadir from any orbit	Pivot and spacecraft roll coordinate to point MDIS boresight to local nadir	G&C scenarios MDPT4 and DTZPT6 roll s/c to keep nadir in pivot plane, supplies MDIS with pivot attitude	Spacecraft functional testing
	Image smear by spacecraft jitter small compared with image smear due to downtrack motion	Jitter <25 μrad in 100 ms (<1 NAC pixel, typical exposure)	<1 μrad in 100 ms	Analytical modeling
	Hold orbital data in recorder	Hold volume of DPU-compressed mages	Baseliine mission requires storing <2.3 Gb; usable recorder vol. 6.2 Gb	Data coverage simulation
		Hold number of MP-compressed mages	Baseliine mission requires storing <2500 compressed images; >8000 available	
Flyby near global monochrome map at 500 m/pixel Multispectral map at 2 km/pixel	Hold flyby data in recorder	Hold volume of DPU-compressed mages	Nominal flyby scenario 5.4 Gb; usable recorder volume of 6.2 Gb	
		Hold number of MP-compressed mages	Nominal flyby scenario 913 images; uncompressed image directory holds 2046	
	Downlink compressed flyby data to ground	>2.3 Gb downlink allocation to MDIS following each Mercury flyby (core data)	Current downlink >6 Gb after each flyby	
Targeted high-resolution imaging	Transfer data to SSR at rate greater than image acquisition	Highest image acquisition rate is 1 Hz (3.2 Mb/s for image binned 2x2 on-chip)	3.2 Mb/s link speed	Instrument and spacecraft functional testing

Table 3b (cont'd). MDIS requirements and as-built performance for spacecraft slewing, stability, memory, downlink. Underlined items incur additional data processing or revisions to the data acquisition strategy to meet requirements, as indicated.

Measurement Objective	Measurement Requirement	Instrument / s/c Requirement	As-built Performance	Method of Verification
Near-nadir global monochrome map at 250 m/pixel Global multispectral map at 2 km/pixel	Downlink compressed orbital data to ground	5.6 Gb/yr minimum allocation to MDIS during orbital mission as per Concept Study	~25.9 Gb/yr allows improvement in average base map sampling from 250 to 140 m/pixel, color to 1 km/pixel	Data coverage simulation
		Pixels 2x2 or 4x4 without overflow at 7 ms exposure	2x2 binning cn-chip sums signal, does not overflow at min. solar distance and phase angle; 2x2, 4x4 binning in MP averages signal	Radiometric calibration; instrument and spacecraft functional testing
		Lossy compression, > 6:1 with artifacts near noise	Wavelet compression in MP; artifacts near noise at 8:1	Simulation using NEAR 16-bit images
Provide optical navigation support for Mercury flybys	Promptly downlink star-planet-star triplets	Return jailbars from Mercury images	Jailbars at regular period in image	Instrument and spacecraft functional testing
		Return ≥3 subframes of stars per image (to 140x140 pixels for NA, allowing for 0.1° pointing control)	Up to 5 subframes per image, sized up to full image	
	Locate Mercury against star background	Detect ≥3 stars in FOV at max exposures	<u>Met for WAC at longest exposure; marginal in NAC</u>	Radiometric calibration and analytical modeling
	Take unsmeared star frames	Jitter <25 μrad in 10 s (<1 NAC pixel)	<25 μrad in 10 s >99% of time	Analytical modeling

Table 3c. MDIS requirements and as-built performance for multispectral imaging. Underlined items incur additional data processing or revisions to the data acquisition strategy to meet requirements, as indicated.

Measurement Objective	Measurement Requirement	Instrument / s/c Requirement	As-built Performance	Method of Verification
Multispectral map at 2 km/pixel	Move filter wheel to allow 11-color imaging strip from lowest altitude over day side	Worst-case FOV motion by 1 footprint in 15.5 sec requires 14 sec per cycle (allowing 10% overlap), 1 Hz imaging in 11 fiilters + 3 sec for reposition	1 Hz imaging supported for exposures <500 ms; 2 sec for reposition; 13 sec total	Instrument functional testing
	<2 km/pixel spatial sampling	<2 km/pixel during flyby, from orbit to fill gaps in flyby coverage	2 km/pixel resolution at 4.5 RM, or within 10,000 km during orbit	Geometric calibration, trajectory analysis
	Spectral filters for mapping of olivine, pyroxene, glass, opaques	7 WA spectral filters, violet to 1050 nm	11 WA spectral filters to measure key features, plus clear filter	Radiometric calibration (see Table 4)
	Map abundance variations in opaque and mafic minerals - 750/415 nm, 750/650 nm, and 750/950 nm ratios measured to 1% precision	MTF >0.62 at 1 cycle/8 pixels to preserve variations above noise level	MTF ~0.75 1 cycle/8 pixels for typical filter	Analysis and radiometric calibration
		Model dark current to <<system noise (<<1 DN)	Dark current model residuals at read-noise level at <5C, consistent with model accuracy <<noise	Radiometric calibration
		Response linearity to 1%	Departures of ≤2% at low DN levels correctable during ground processing	Radiometric calibration
		Characterize responsivity to 5% absolute, 2% relative between filters	Onground cal at -34C, -30C, 24C insufficient for extrapolation to higher (-10C) CCD operating temps.; need flight measurement of Mercury-illuminated cal. target	Radiometric calibration
		Model flat field to 0.1% precision (0.4 of noise at full well)	Composite of 100 images provides 0.04% precision; flight measurements needed due to mobility of dust donuts	Radiometric calibration
	Protect optics from contamination that increases scattered light	Stow MDIS in position with optics protected from contaminants during burns, thermal spikes on sunshade	Front optic stowable in instrument base	Instrument functional test

Table 3d. MDIS requirements and as-built performance for high-resolution and stereo imaging.

Measurement Objective	Measurement Requirement	Instrument / s/c Requirement	As-built Performance		Method of Verification
Targeted high-resolution imaging	Acquire continuous strip of images with NAC from minimum orbital altitude	At minimum altitude of 200 km, NA footprint moves 1 FOV in 1.4 sec. Requires 1 Hz imaging.	1 Hz imaging supported using 2x2 pixel binning or quarter frames		Instrument functional testing
	Acquire <20 m/pixel NAC frames from lowest altitude expected over day side (280 km) with <20 m smear due to spacecraft motion	NAC IFOV <71 µrad	NAC IFOV 20 µrad		Geometric and radiometric calibration
		Minimize time for CCD frame transfer (minimum useful exposure time ~2x frame transfer time)	3.7 ms frame transfer yields ~7 ms exposure. At 3.3 km/s, 18 m linear smear. Pixel footprint 12 m/pixel after 2x2 binning required for 1 Hz imaging		
	No saturation at minimum exposure time	No saturation in 7 ms NAC image at 33° phase, min. solar distance, 2x2 pixel binning	Worst-case saturation time 16 ms		Radiometric calibration and photometric model
Off-nadir imaging to complement nadir geometry for stereo	Image areas both at nadir and off-nadir with similar lighting	Consistent observation strategy meeting other spacecraft constraints	N hemisphere nadir 1st solar day, off-nadir 2nd solar day; S hemisphere nadir and off-nadir on adjacent orbits 1st solar day. Meets s/c constraints as given in Table 3b.		Coverage simulation
	Ability to take off-nadir images an arbitrary orbit	Pivot and spacecraft roll usable together to point MDIS boresight offset along-track from local nadir	G&C scenarios MDPT4 and DTZPT6 roll s/c to keep nadir offset from pivot plane, supply MDIS with pivot attitude		Spacecraft functional testing
	Stereo vertical accuracy GOAL ±2 km from 6000-km altitude (RSS pointing knowledge 240 µrad)	180 µrad boresight knowledge with inflight calibrations (1.4x worse than NEAR with inflight pointing cals. using star images; allows for scan plane vs. fixed pointing)	Ability to extract multiple subframes from starfield images for pointing calibrations within downlink	200 µrad expected pointing knowledge	Instrument and spacecraft functional testing; flight calibration required for ptg. knowledge
		150 µrad knowledge of pivot position	85 µrad		Gimbal position calibration
		Knowledge of center of MDIS exposure to ±10 ms	<1 ms uncertainty		Analysis of image acquistion timing using external strobe and UT clock
		Acquire images from orbits with minimal thermal disturbances to instrument deck	Nadir and off-nadir coverage planned from near-terminator orbit with lesser thermal variation		By design

Table 4. MDIS Wide Angle Camera (WAC) filter wavelengths, bandpasses, and scientific rationale (glass=agglutinates and pyroclastic, RGB=natural color composite, opaques= minerals such as ilmenite, mafic=iron bearing silicate minerals such as olivine, and pyroxene). WHAT DOES THE COLUMN COMPLY CONVEY???????

Filter #	Nominal Center Wavelength	Nominal Bandwidth	System Center Wavelength, -26°C	System Bandwidth	Comply?	Rationale
1	700	5	698.8	4.4	Y	glass
2	700	600			Y	optical nav., pointing cal.
3	480	10	480.4	8.9	Y	RGB, opaques
4	560	5	559.2	4.6	Y	RGB, glass
5	630	5	628.7	4.4	Y	RGB, glass
6	415	40	430	18	Y	opaques
7	750	5	749.0	4.5	Y	mafic,., opaques, maturity
8	950	7	948.0	4.9	Y	mafic.
9	1000	15	996.8	12.0	Y	mafic.
10	900	5	898.1	4.3	Y	mafic.
11	1020	40	1010	20	Y	mafic
12	830	5	828.6	4.1	Y	mafic

Table 4a. MDIS Camera Specifications.

	Narrow Angle	**Wide Angle**
Field of View	1.5°	10.5°
Pivot Range (Observational)	-40° to +50° (Sunward) (Planetward)	
Exposure Time	1 ms to 9989 ms	
Frame Transfer Time	3.84 ms	
Image Readout Time†	1 s	
Spectral Filters	1	12 positions
Focal Length	550 mm	78 mm
Collecting Area	462 mm²	48 mm²
Detector-TH7888A	CCD 1024×1024, 14 μm pixels	
IFOV	26 μrad	179 μrad
Pixel FOV	5.1 m at 200 km altitude	35.8 m at 200 km altitude
Quantization	12-bits per pixel	
Compression	Lossless, multi-resolution lossy, 12-to-n bits	

†Transfer to DPU; Transfer from DPU to SSR limited to 3 Mbps (4 sec to transfer 1024×1024 image)

Table 5a. MDIS Wide Angle Camera (WAC) sensitivity to stars. Light gray boxes represent mv values with <3 stars in FOV; dark gray boxes represent DN levels below 7x the read noise (7 DN for the WAC). White boxes show the range of mv values meeting optical navigation requirements (≥3 stars per FOV at 7x read noise). (What does mv stand for?)

mv	10 s exposure, no pixel sum, ensq. energy = 70% DN	10 s exposure, 2x2 pixel sum, ensq. energy = 90% DN	10 s exposure, no pixel sum, ensq. energy = 22% DN	# stars of ≥ mag in WA FOV
0	21000	27000	6500	0.06
1	8200	11000	2600	0.16
2	3300	4200	1000	0.37
3	1300	1700	410	0.9
4	520	670	160	2.2
5	210	270	65	5.2
6	82	110	26	12
7	33	42	10	30
8	13	17	4.1	71
9	5.2	6.7	1.6	180
10	2.1	2.7	0.66	420
11	0.84	1.1	0.26	1000

Table 5b. MDIS Narrow Angle Camera (NAC) sensitivity to stars. Light gray boxes represent mv values with <3 stars in FOV; dark gray boxes represent DN levels below 7x the read noise (14 DN for the WAC).

mv	10 s exposure, no pixel sum, ensq. energy = 43% DN	10 s exposure, 2x2 pixel sum, ensq. energy = 70% DN	10 s exposure, no pixel sum, ensq. energy = 30% DN	# stars of ≥ mag in NA FOV
0	8600	32000	14000	0
1	3400	13000	5600	0
2	1400	5100	2200	0.01
3	540	2000	890	0.01
4	220	820	350	0.03
5	86	320	140	0.08
6	34	130	56	0.2
7	14	51	22	0.48
8	5.4	20	8.8	1.2
9	2.2	8.2	3.5	2.8
10	0.86	3.3	1.4	6.7
11	0.34	1.3	0.56	16

Table 6a. NAC not-binned dark models.

Coefficient	H_0	H_1	H_2	H_3
Dark Current				
C	4202.30	-10.7314	0.00974273	-2.94302e-06
D	-64.4884	0.179181	-0.000165891	5.11765e-08
E	-2.58253	0.00754599	-7.35219e-06	2.38873e-09
F	-0.000464774	1.31009e-06	-1.23407e-09	3.88515e-13
O	0.0143372	-4.21571e-05	4.12534e-08	-1.34637e-11
P	-6.86389e-05	1.80933e-07	-1.57409e-10	4.50925e-14
Q	-0.000169733	4.92790e-07	-4.77059e-10	1.53993e-13
S	1.35800e-07	-4.33913e-10	4.56621e-13	-1.58643e-16
Dark Column				
C	5451.46	-14.2965	0.0131305	-4.01470e-06
D	-66.9307	0.185911	-0.000172068	5.30647e-08
E	-2.42407	0.00705565	-6.84831e-06	2.21669e-09
F	0.00526574	-1.44654e-05	1.32342e-08	-4.03222e-12
O	-1.81968	0.00519216	-4.93259e-06	1.55995e-09
P	0.00351380	-9.68964e-06	8.90189e-09	-2.72453e-12
Q	-0.000402942	1.21434e-06	-1.21845e-09	4.07108e-13
S	-8.26754e-06	2.26993e-08	-2.07595e-11	6.32380e-15

Table 6b. NAC binned dark models.

Coefficient	H_0	H_1	H_2	H_3
Dark Current				
C	-5809.80	17.2831	-0.0163855	5.17322e-06
D	-18.7770	0.0535211	-5.08542e-05	1.61084e-08
E	-52.1256	0.148428	-0.00014089	4.45864e-08
F	-0.00425778	1.22892e-05	-1.18214e-08	3.78984e-12
O	0.676937	-0.00190954	1.79397e-06	-5.61987e-10
P	0.00180111	-5.16803e-06	4.94001e-09	-1.57305e-12
Q	-0.00688223	1.94574e-05	-1.83419e-08	5.76568e-12
S	9.00182e-06	-2.57628e-08	2.45929e-11	-7.83098e-15
Dark Column				
C	-8188.55	24.0208	-0.0227352	7.16515e-06
D	-16.5122	0.0471223	-4.48311e-05	1.42195e-08
E	-38.7242	0.110516	-0.00010516	3.33600e-08
F	-0.0110371	3.13365e-05	-2.96580e-08	9.35730e-12
O	7.69642	-0.0217915	2.05305e-05	-6.43961e-09
P	-0.00486634	1.36687e-05	-1.27902e-08	3.98703e-12
Q	-0.0463603	0.000131138	-1.23619e-07	3.88354e-11
S	2.89199e-05	-8.17259e-08	7.69996e-11	-2.41893e-14

Table 6c. WAC not-binned dark models.

Coefficient	H_0	H_1	H_2	H_3
Dark Current				
C	1238.24	-2.76843	0.00256473	-7.86953e-07
D	-3.48338	0.0101166	-9.79576e-06	3.16249e-09
E	-2.42999	0.00714405	-7.00585e-06	2.29185e-09
F	-0.00053432	1.49958e-06	-1.40025e-09	4.34984e-13
O	0.0206338	-6.29517e-05	6.39338e-08	-2.16318e-11
P	-0.00033310	9.70986e-07	-9.43818e-10	3.05943e-13
Q	0.000517513	-1.51006e-06	1.46957e-09	-4.77044e-13
S	1.17016e-07	-3.34717e-10	3.19031e-13	-1.01330e-16
Dark Column				
C	-3182.94	9.81730	-0.00936597	2.97916e-06
D	12.7966	-0.0364940	3.46355e-05	-1.09384e-08
E	11.4352	-0.0325653	3.08604e-05	-9.73046e-09
F	-0.0755373	0.000216107	-2.05838e-07	6.52700e-11
O	1.26711	-0.00353596	3.28770e-06	-1.01873e-09
P	0.00127217	-3.57421e-06	3.33658e-09	-1.03455e-12
Q	0.000637356	-1.79417e-06	1.67841e-09	-5.21619e-13
S	-2.32720e-06	6.63236e-09	-6.28992e-12	1.98479e-15

Table 6d. WAC binned dark models.

Coefficient	H_0	H_1	H_2	H_3
Dark Current				
C	-484.568	2.11771	-0.00206813	6.75547e-07
D	-10.2411	0.0299233	-2.91567e-05	9.47476e-09
E	-27.9169	0.0813578	-7.90653e-05	2.56248e-08
F	0.000646762	-1.91510e-06	1.89122e-09	-6.22884e-13
O	-0.550564	0.00152559	-1.40630e-06	4.30355e-10
P	-0.00201059	5.92984e-06	-5.83228e-09	1.91308e-12
Q	0.0127947	-3.69327e-05	3.55415e-08	-1.14037e-11
S	-1.54738e-06	4.29029e-09	-3.95289e-12	1.20989e-15
Dark Column				
C	876.088	-1.72949	0.00155692	-4.62411e-07
D	-8.67913	0.0253792	-2.47483e-05	8.04835e-09
E	-24.2259	0.0705204	-6.84466e-05	2.21526e-08
F	-0.00286560	8.40352e-06	-8.21840e-09	2.68055e-12
O	-4.55575	0.0128502	-1.20770e-05	3.78006e-09
P	-0.00660749	1.93028e-05	-1.88063e-08	6.11108e-12
Q	0.00192523	-5.01882e-06	4.27240e-09	-1.17912e-12
S	8.80210e-06	-2.61144e-08	2.58360e-11	-8.52398e-15

Table 7. WAC and NAC responsivities. Slope and offset are for correction to responsivity at a CCD temperature count of 1060, or -30.25°C. Binned responsivity in each filter is four times the not-binned value, but the temperature correction offset and slope are the same.

Filter #	Responsivity, W m^{-2} nm^{-1} sr^{-1}	Temperature correction offset	Temperature correction slope
Not-binned WAC			
01	11320.0	2.9472E-01	6.6513E-04
03	869.9	-3.3249E+00	4.0787E-03
04	4106.4	1.2232E+00	-2.1054E-04
05	7823.5	1.0085E+00	-8.0254E-06
06	59.9	1.2313E+00	-2.1811E-04
07	11635.2	-3.6408E-01	1.2864E-03
08	6286.5	-9.2164E-01	1.8122E-03
09	2957.1	-2.4858E+00	3.2873E-03
10	9135.5	-6.3166E-01	1.5388E-03
11	2175.6	-2.6621E+00	3.4536E-03
12	11769.9	-1.7758E-01	1.1105E-03
Binned WAC			
01	45280.0	2.9472E-01	6.6513E-04
03	3479.6	-3.3249E+00	4.0787E-03
04	16425.6	1.2232E+00	-2.1054E-04
05	31294.0	1.0085E+00	-8.0254E-06
06	239.6	1.2313E+00	-2.1811E-04
07	46540.8	-3.6408E-01	1.2864E-03
08	25146.0	-9.2164E-01	1.8122E-03
09	11828.4	-2.4858E+00	3.2873E-03
10	36542	-6.3166E-01	1.5388E-03
11	8702.4	-2.6621E+00	3.4536E-03
12	47079.6	-1.7758E-01	1.1105E-03
Not-binned NAC	2647.07	1.3267E+00	-3.0895E-04
Binned NAC	10082.8	1.1397E+00	-1.3267E-04

Table 8. MESSENGER MDIS EDR delivery schedule to PDS.

Mission Data	Product	MESSENGER Planned Delivery Date
Prelaunch Calibration	EDR	6 months after launch
Earth flyby 1	EDR	6 months after 2nd Venus flyby encounter
Venus flyby 1	EDR	6 months after 2nd Venus flyby encounter
Venus flyby 2	EDR	6 months after 2nd Venus flyby encounter
Mercury flyby 1	EDR	6 months after 2nd Mercury flyby encounter
Mercury flyby 2	EDR	6 months after 2nd Mercury flyby encounter
Mercury flyby 3	EDR	6 months after 3rd Mercury flyby encounter
Mercury orbit	EDR	6 months after end of mission (18 months after Mercury orbit insertion)

FIGURES

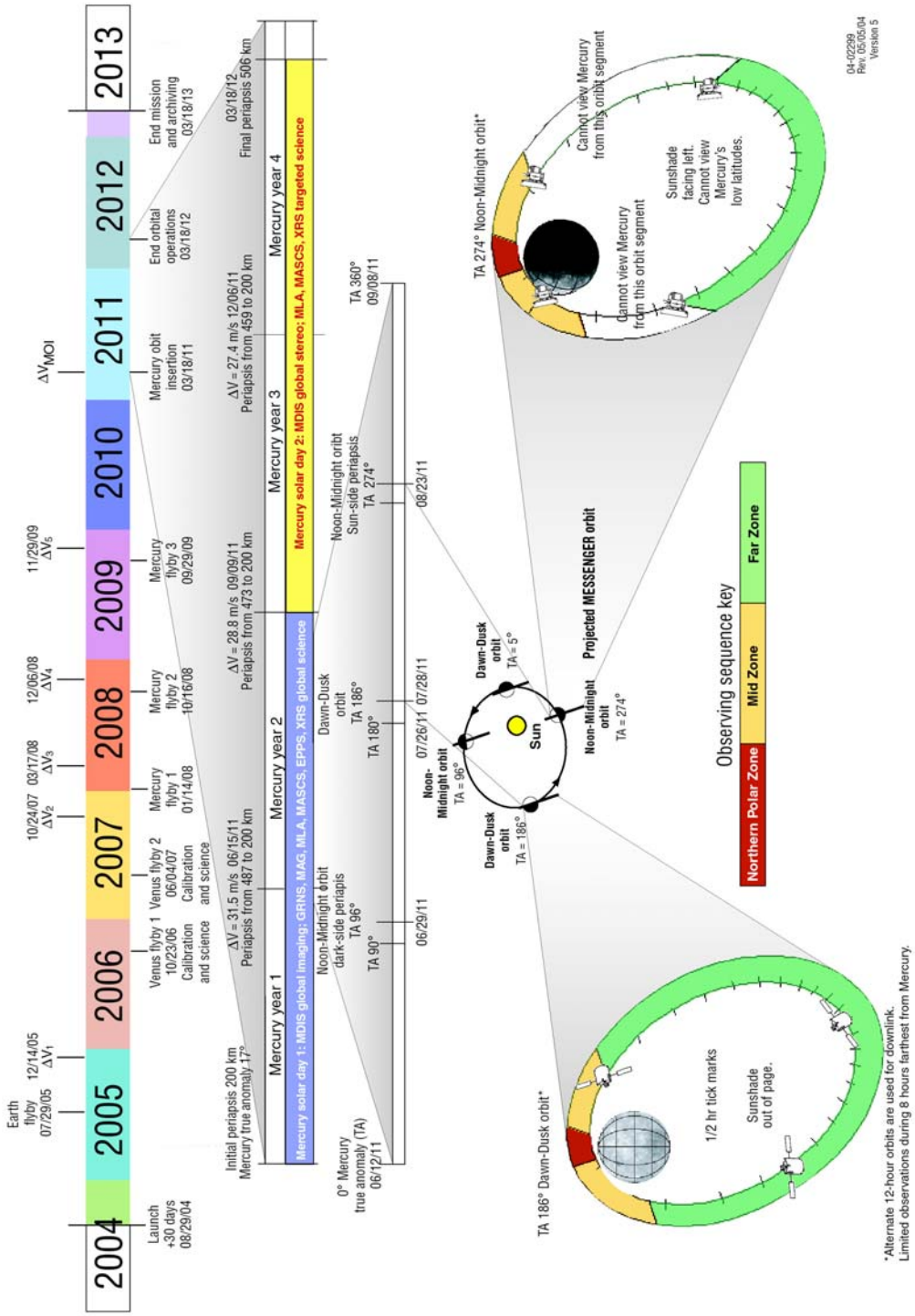

Figure 1. Schematic overview of the MESSENGER mission timeline and orbital geometry.

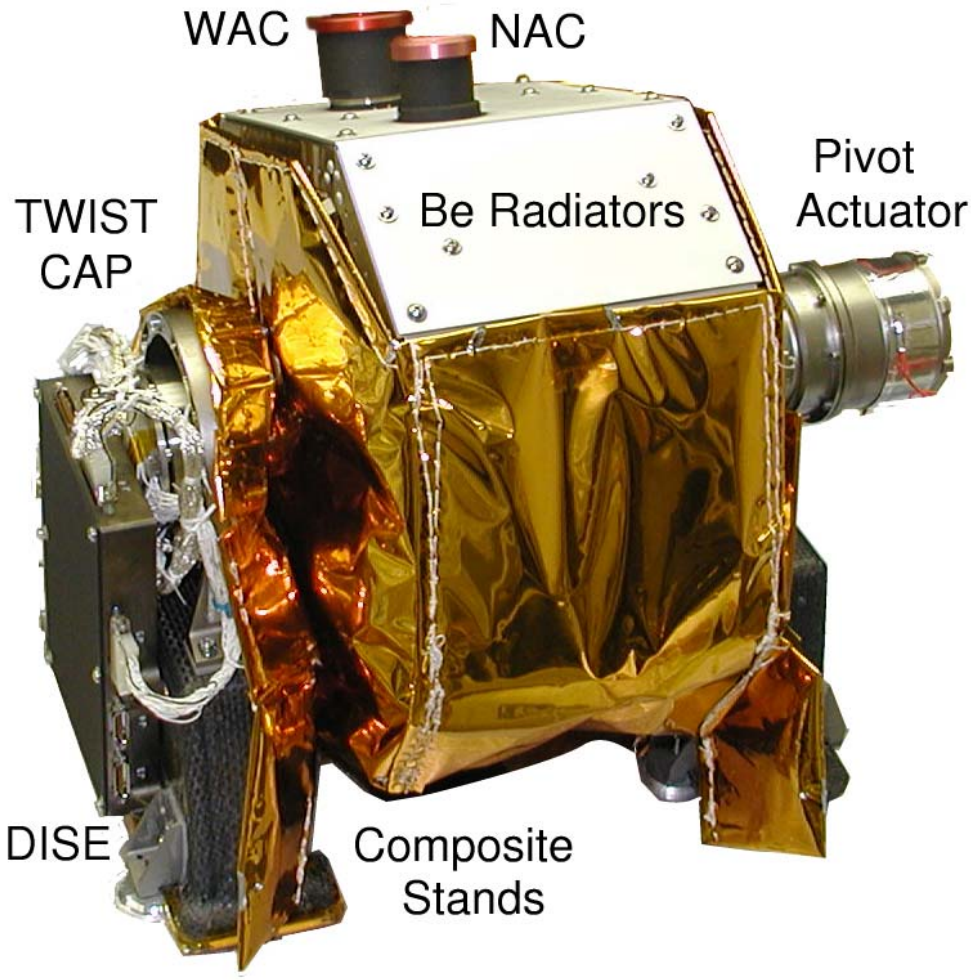

Figure 2. Mercury Dual Imaging System (MDIS) contains wide and narrow angle imagers mounted on a common pivot.

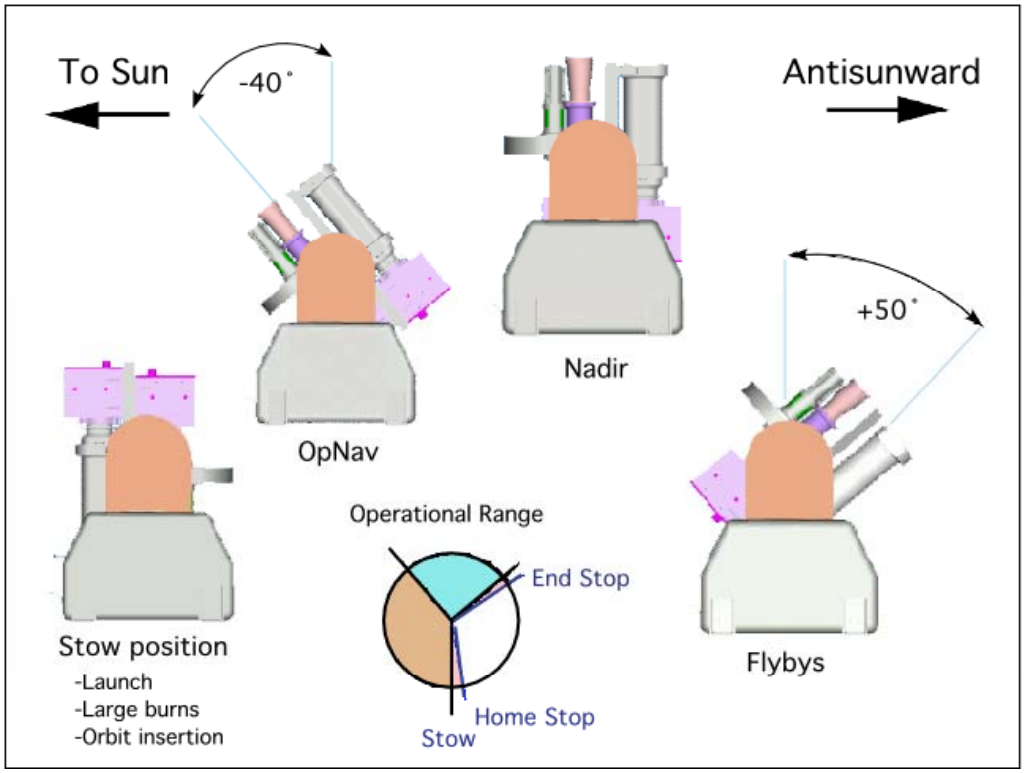

Figure 3. Mobility of MDIS pivot.

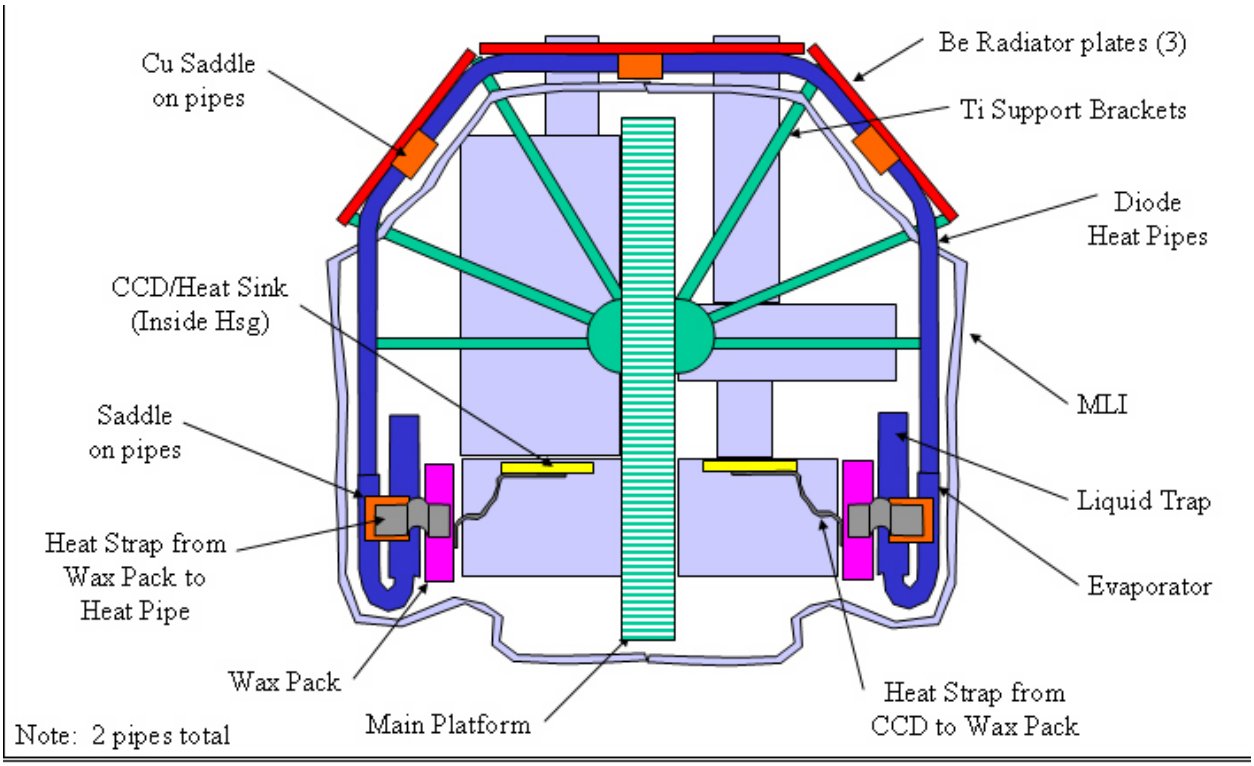

Figure 4. Key design elements that maintain the MDIS CCD at nominal operating temperatures. Each CCD (NAC on left, WAC on right) is thermally coupled to phase-change wax packs that buffer the detector temperature. The wax packs are cooled by the radiator at times when the hot surface of Mercury does not occupy a large part of the radiator FOV. The thermal switches and heat pipes provide thermal connection when the radiator FOV is cold, and thermal isolation when it is hot.

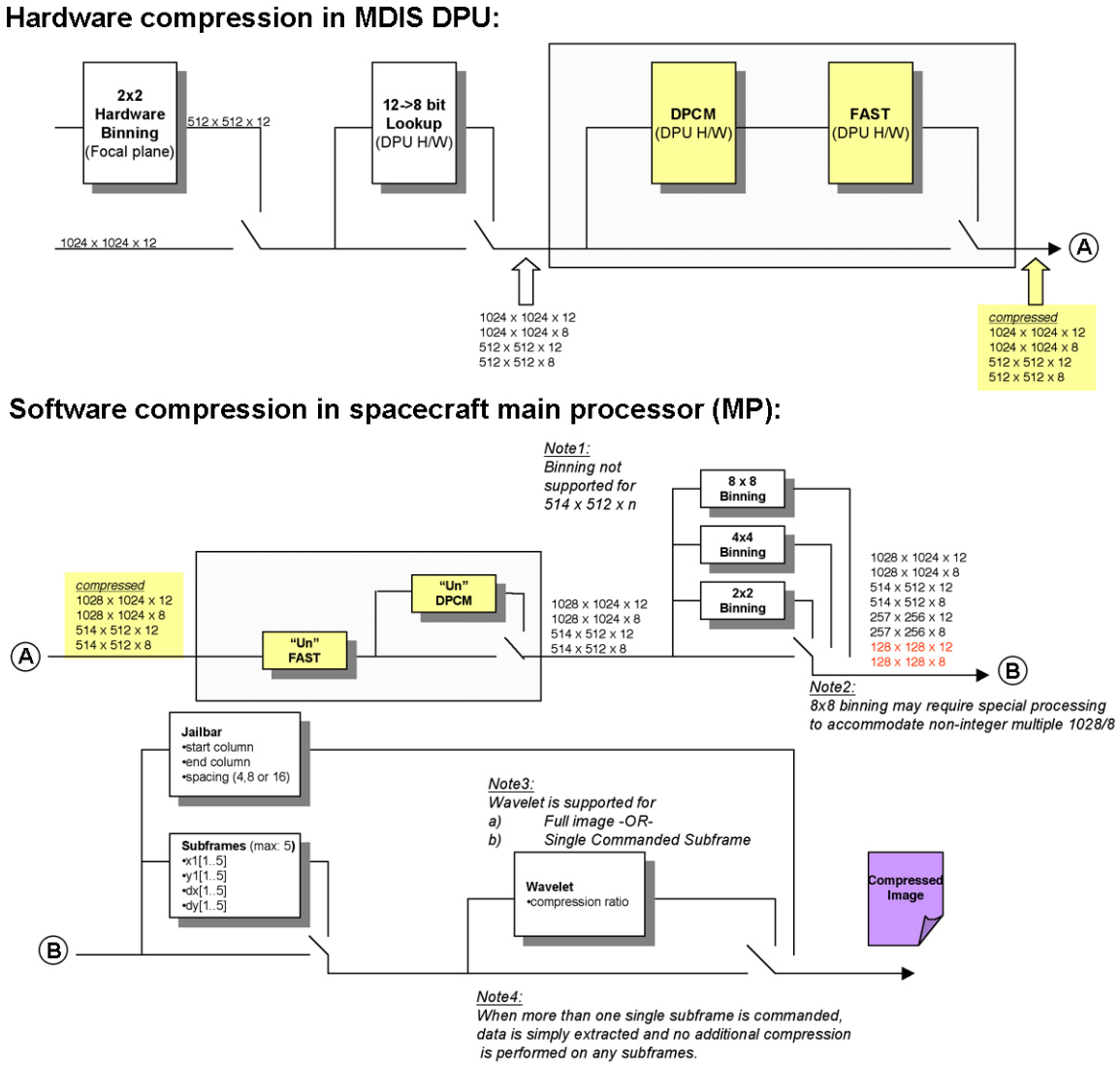

Figure 5. Compression options available for MDIS images in the instrument DPU and spacecraft main processor.

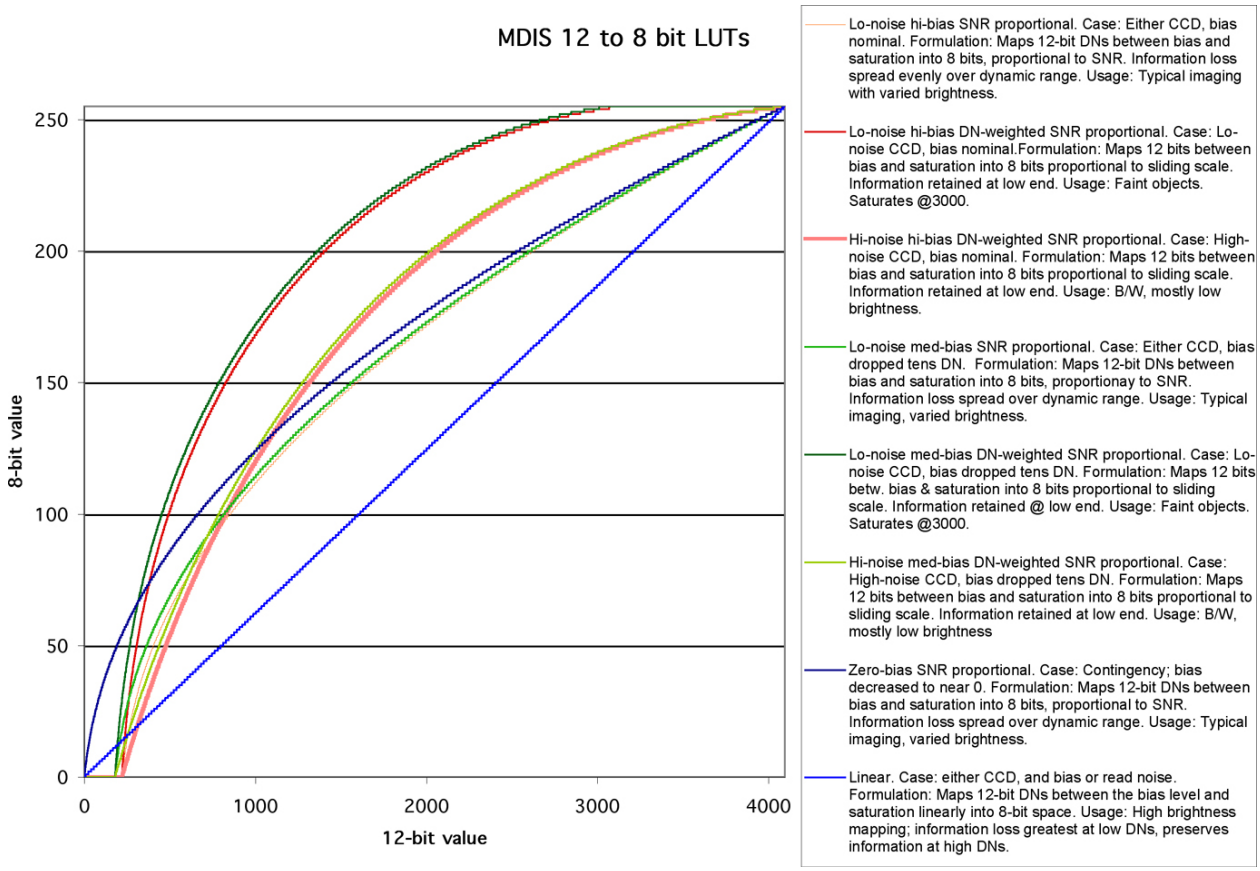

Figure 6. Mapping of 12 bits to 8 bits will be accomplished using onboard look-up tables. The tables are designed to preferentially preserve information at different DN ranges, and they can accommodate a nominal detector dark level as well as one that has changed with time.

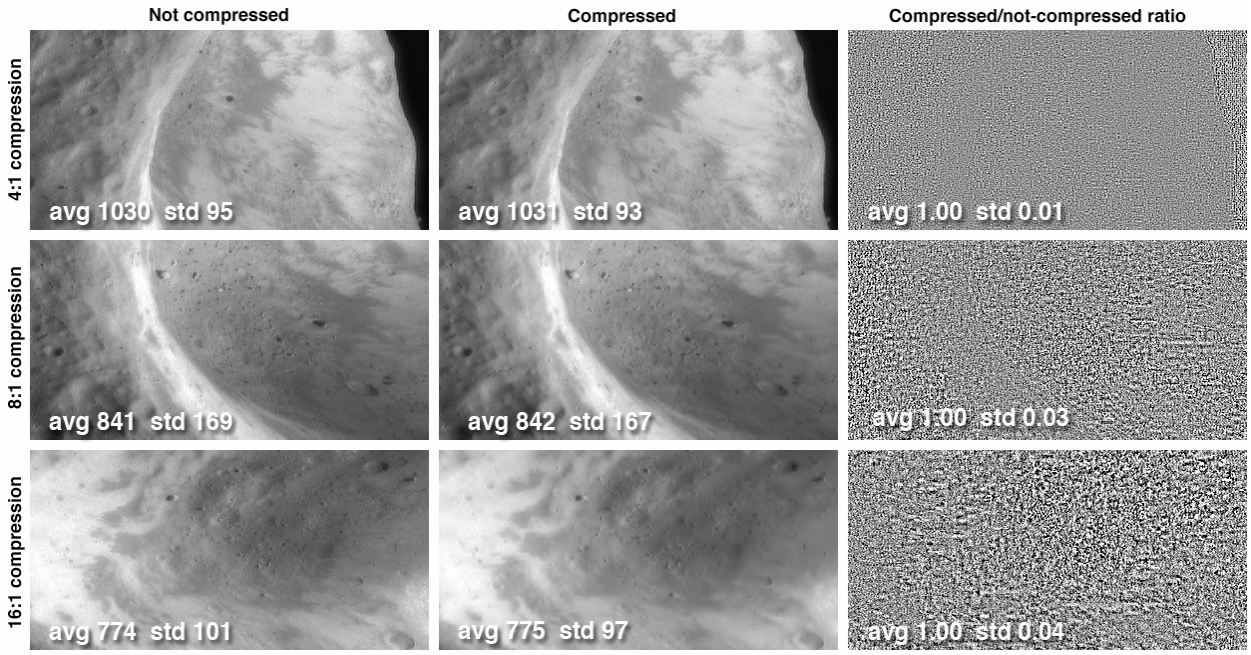

Figure 7. Effects of compression to different ratios using the MESSENGER integer wavelet transform. Well-exposed 12-bit (DN peaks near 3000 out of 4095) NEAR MSI images simulate well the properties of MDIS raw data. . The left column shows the image prior to compression, and the middle column after compression and decompression. The right column shows the ratio of the decompressed image to the original; the standard deviation of the ratio is a measure of the artifacts for typical illumination.

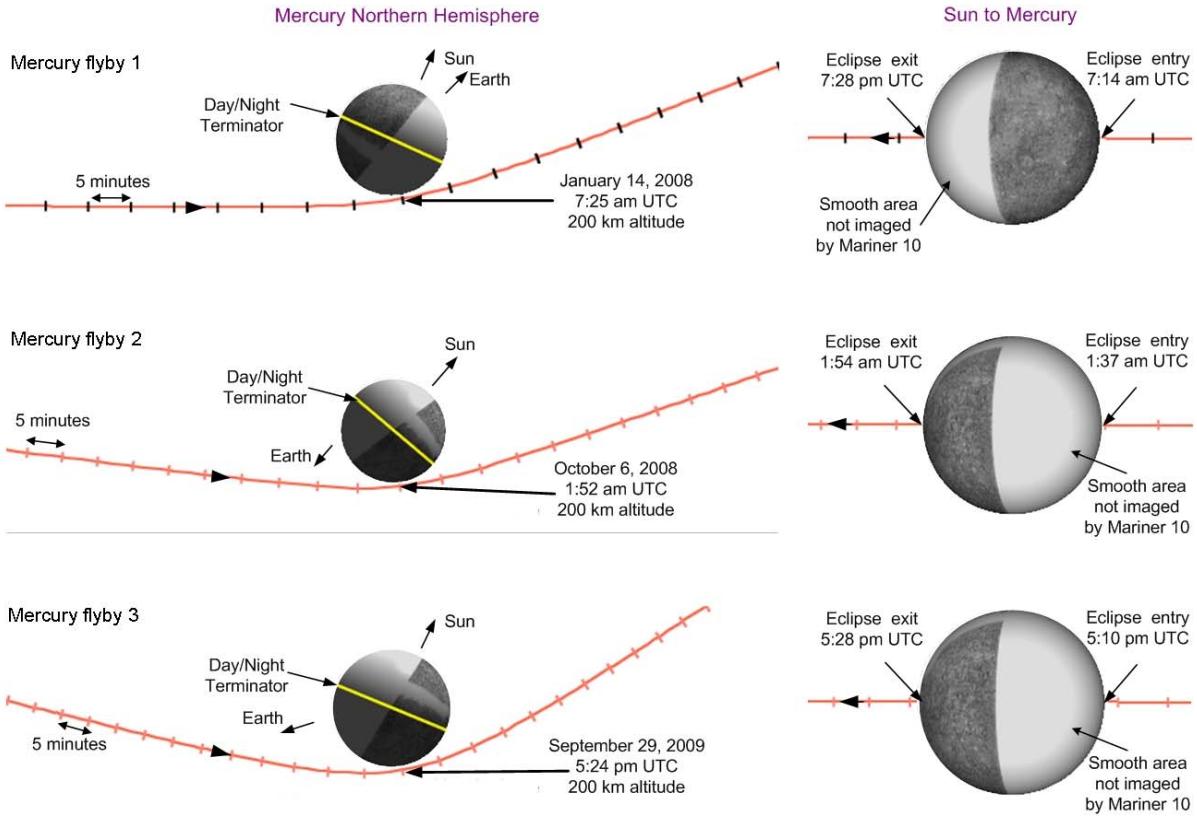

Figure 8. Geometry of Mercury flybys for a 30 July 2004 launch date.

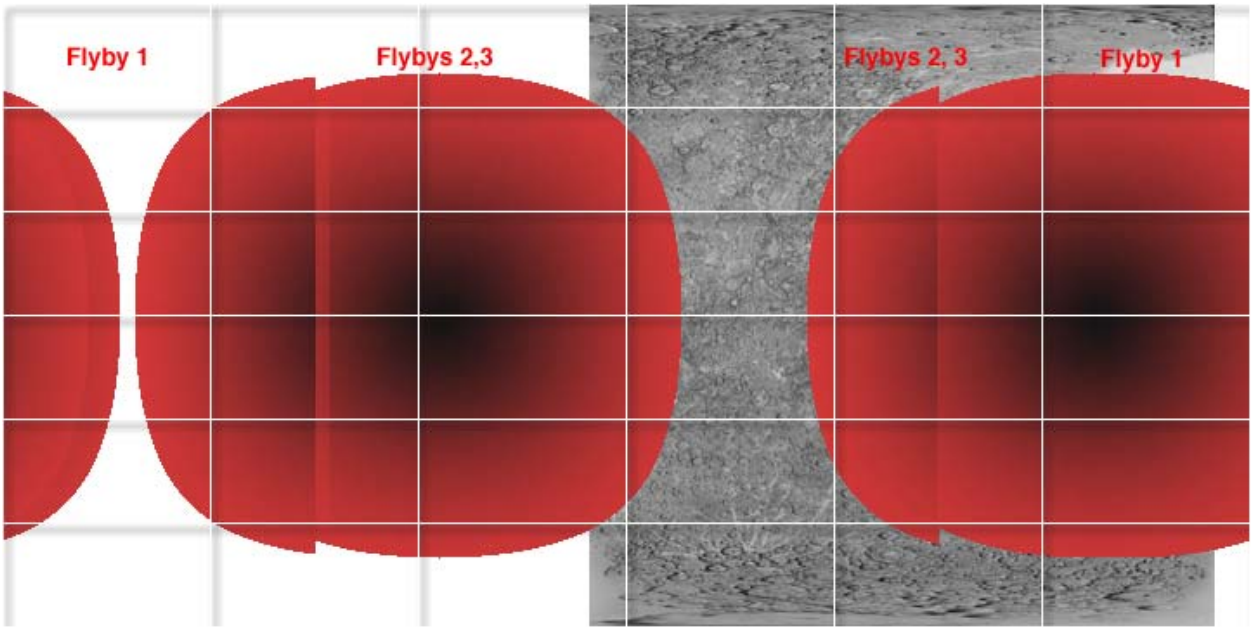

Figure 9. Preliminary map, in simple cylindrical projection, of MDIS flyby imaging coverage at ≤500 m/pixel (at subspacecraft point) from a range of 20,000 km and emission angle ≤70°.

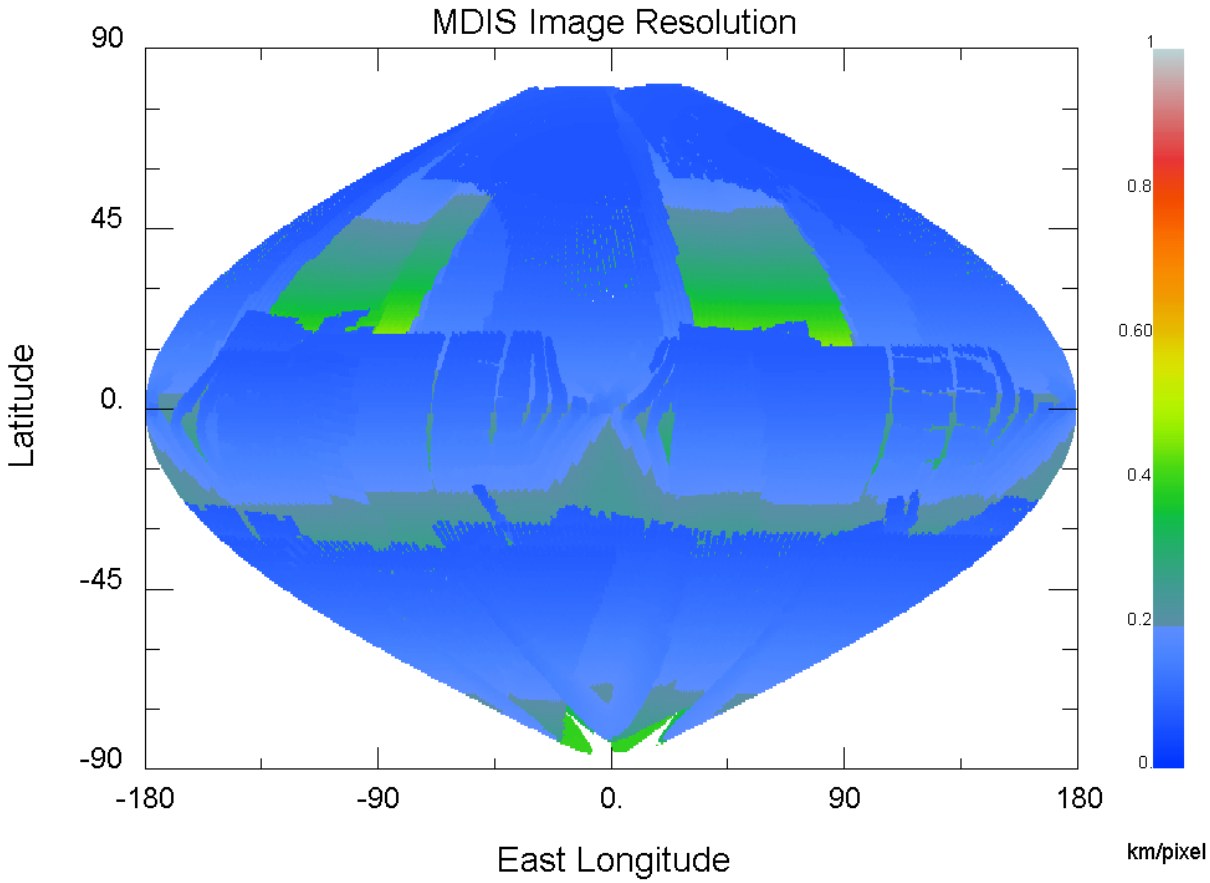

Figure 10. Preliminary map of spatial sampling in the MDIS global basemap, in simple sinusoidal projection.

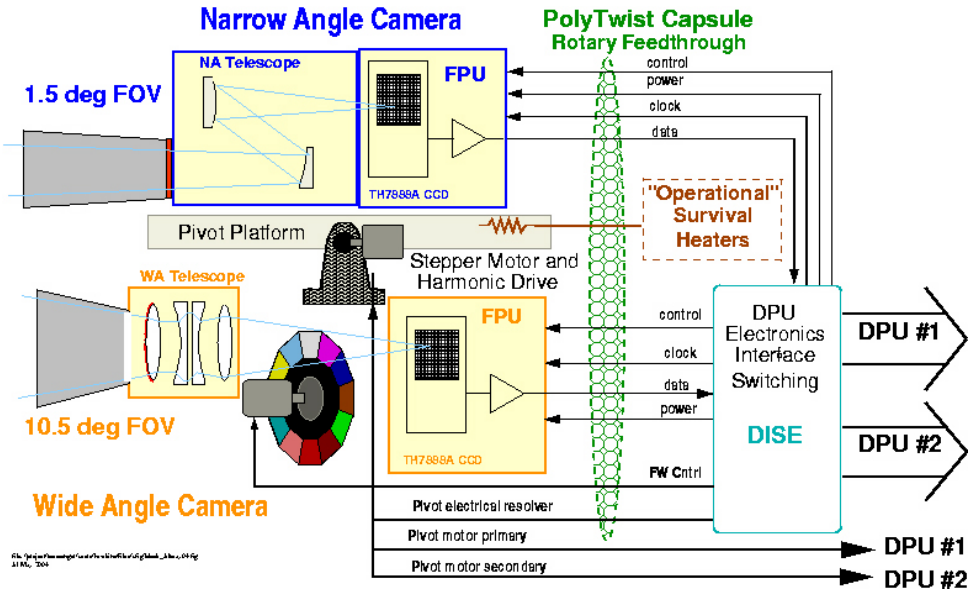

Figure 11. MDIS functional block diagram.

Figure 12. Hollow shaft after assembly. (Why is this figure in here?????)

Figure 13. Mounting of pivot assembly, and who cares? Caption should convey main point.

Figure 14. Twist cap assembly. Why is this figure in here?

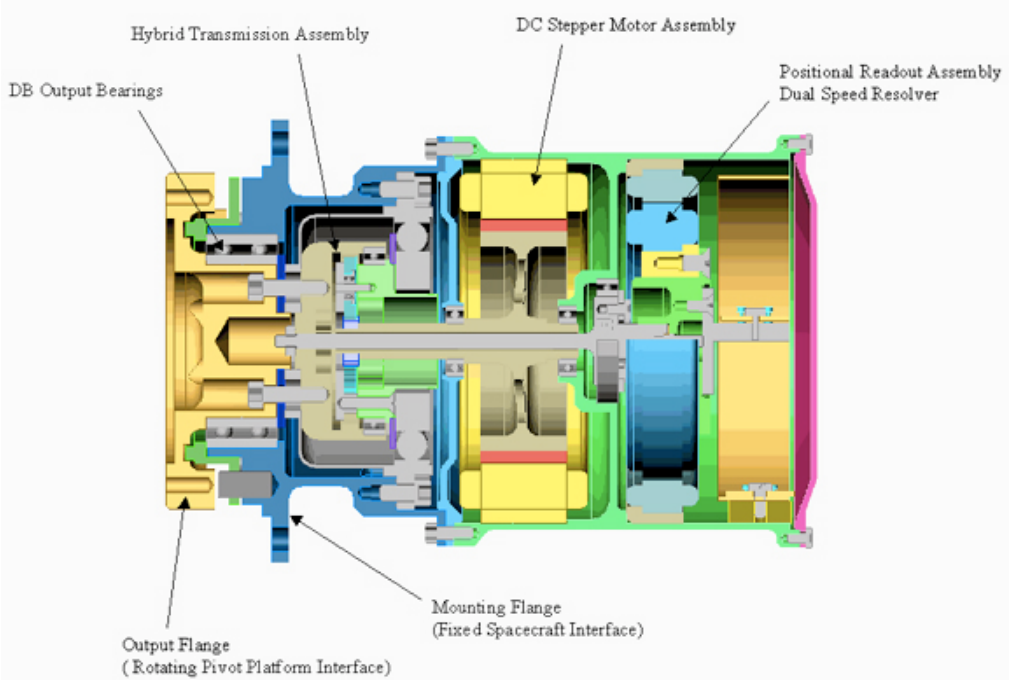

Figure 15. Schematic of MDIS pivot motor.

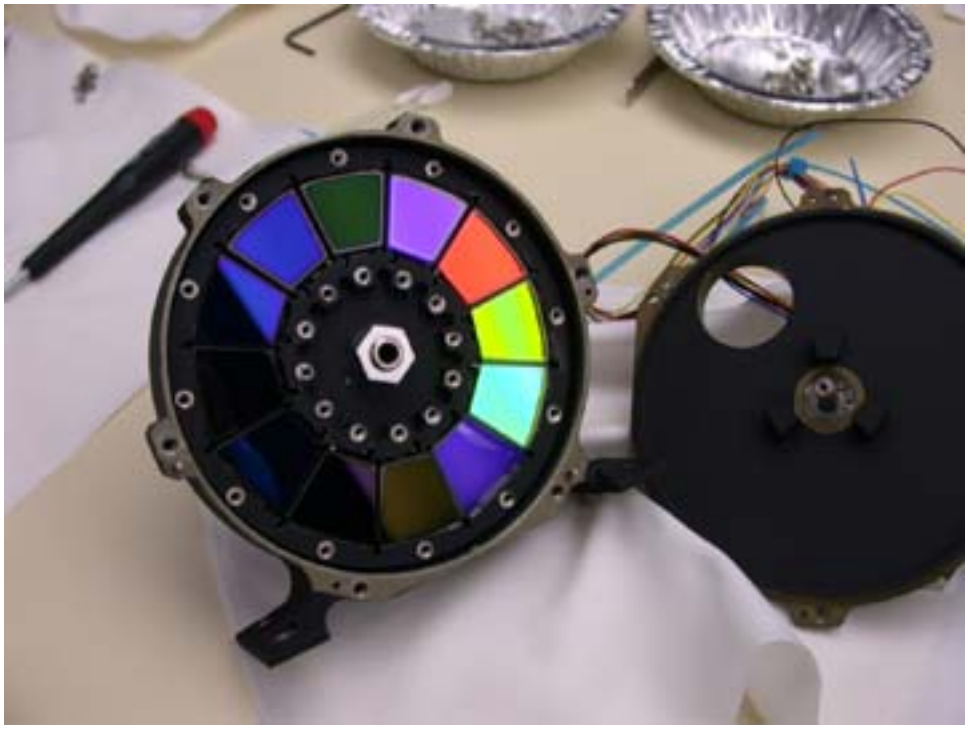

Figure 16. Filter wheel assembly

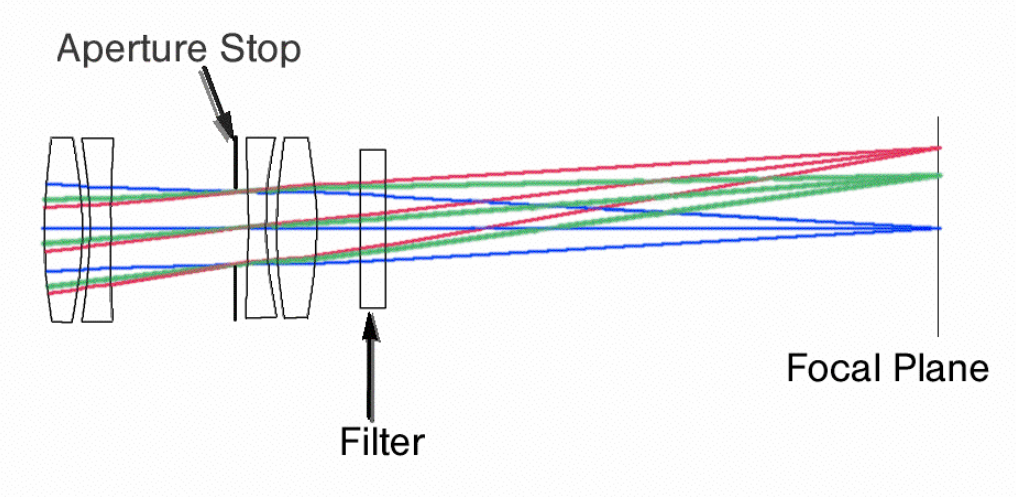

Figure 17. Wide angle camera (WAC) ray-trace diagram.

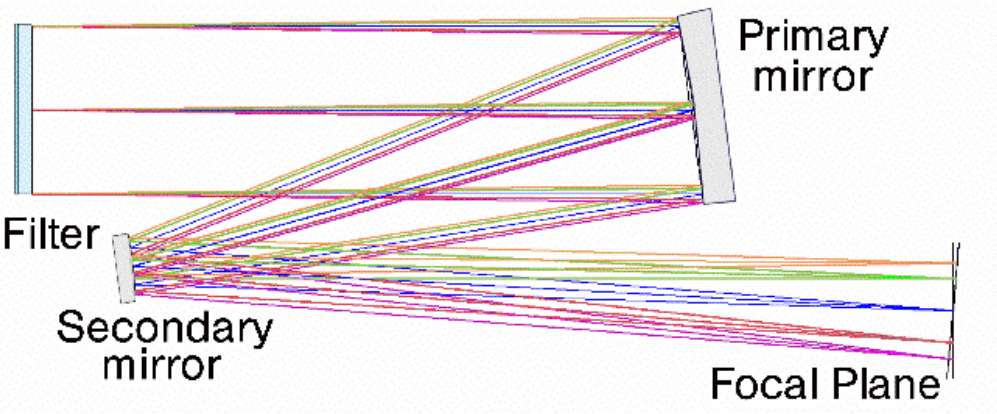

Figure 18. NAC ray-trace diagram.

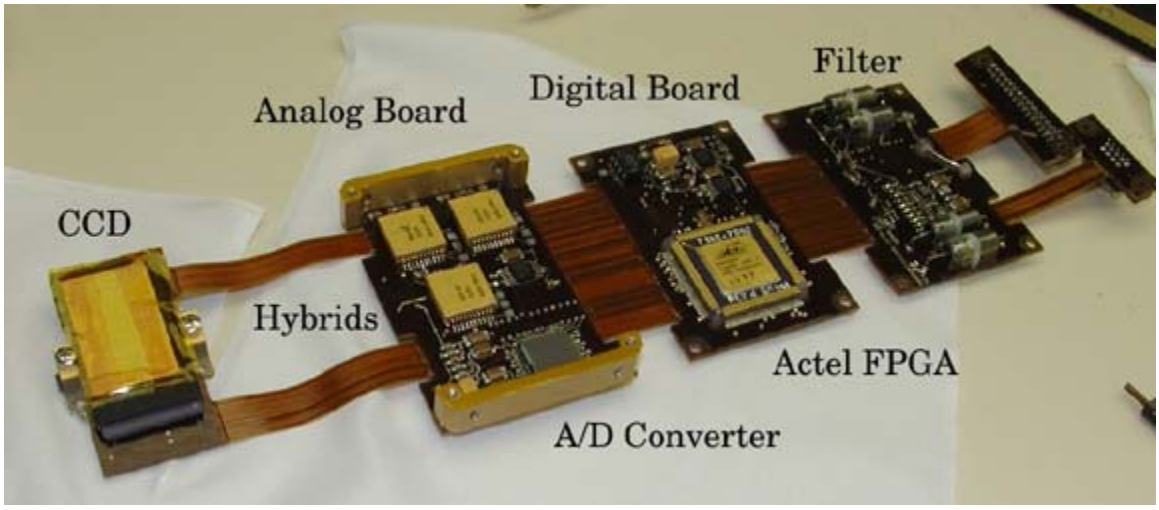

Figure 19. Multiple rigid flex circuits comprise the FPU electronics. This figure could go if you run into space problems.

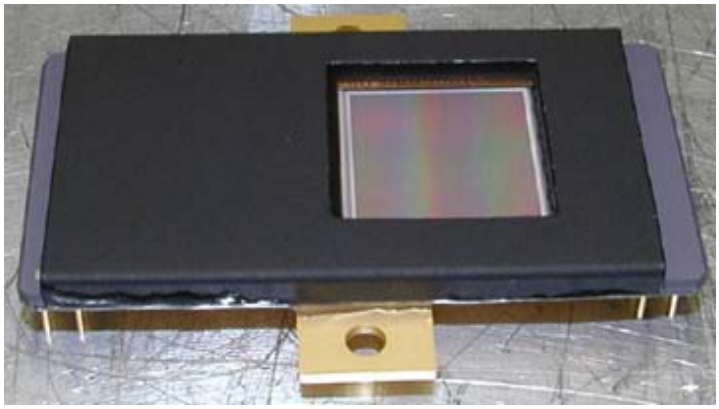

Figure 20. Thomson (Atmel)-TH7888A CCD. Need some sense of scale and some labels!

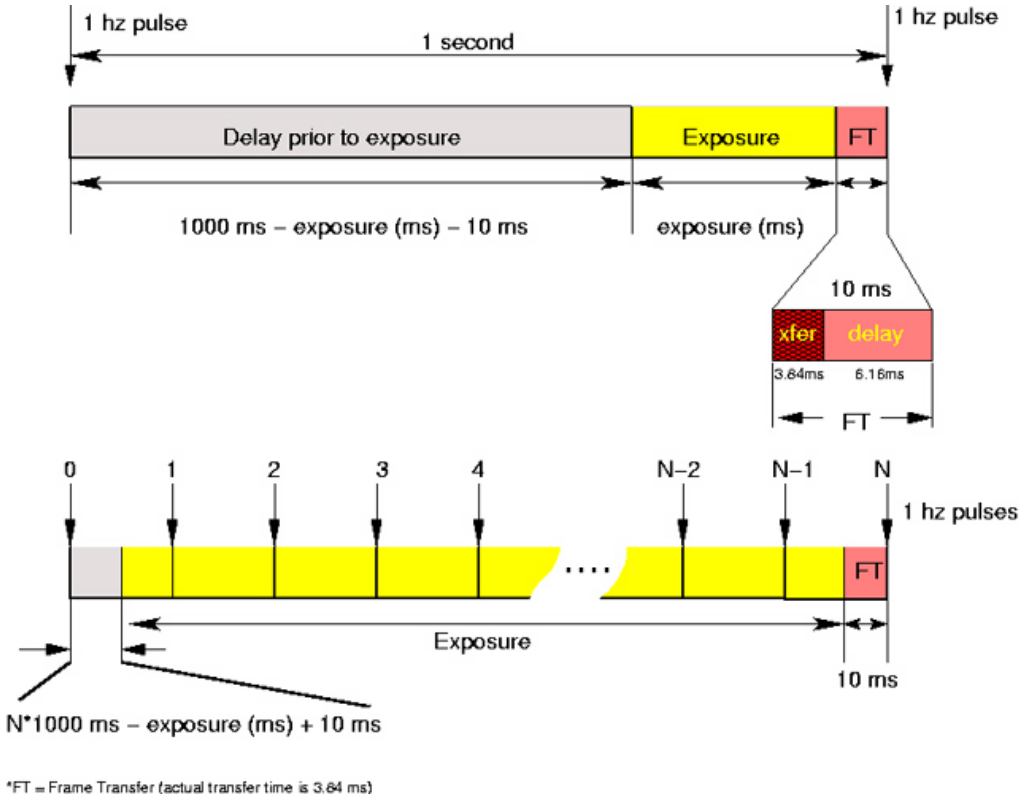

Figure 21. Field Programmable Gate Array clocking, control and readout of the CCDs.

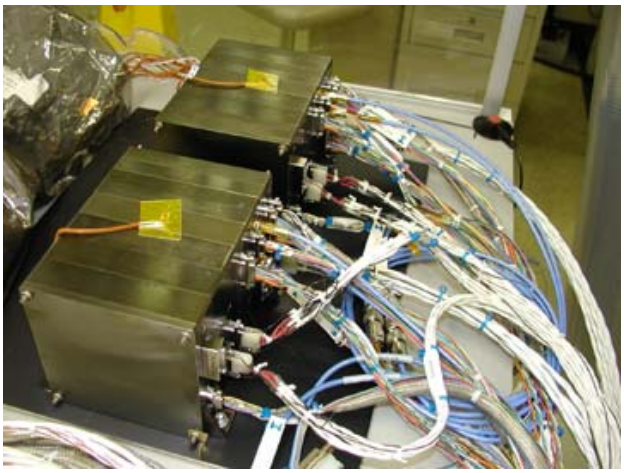

Figure 22. MDIS DPUs. This figure could also end up on the cutting room floor.

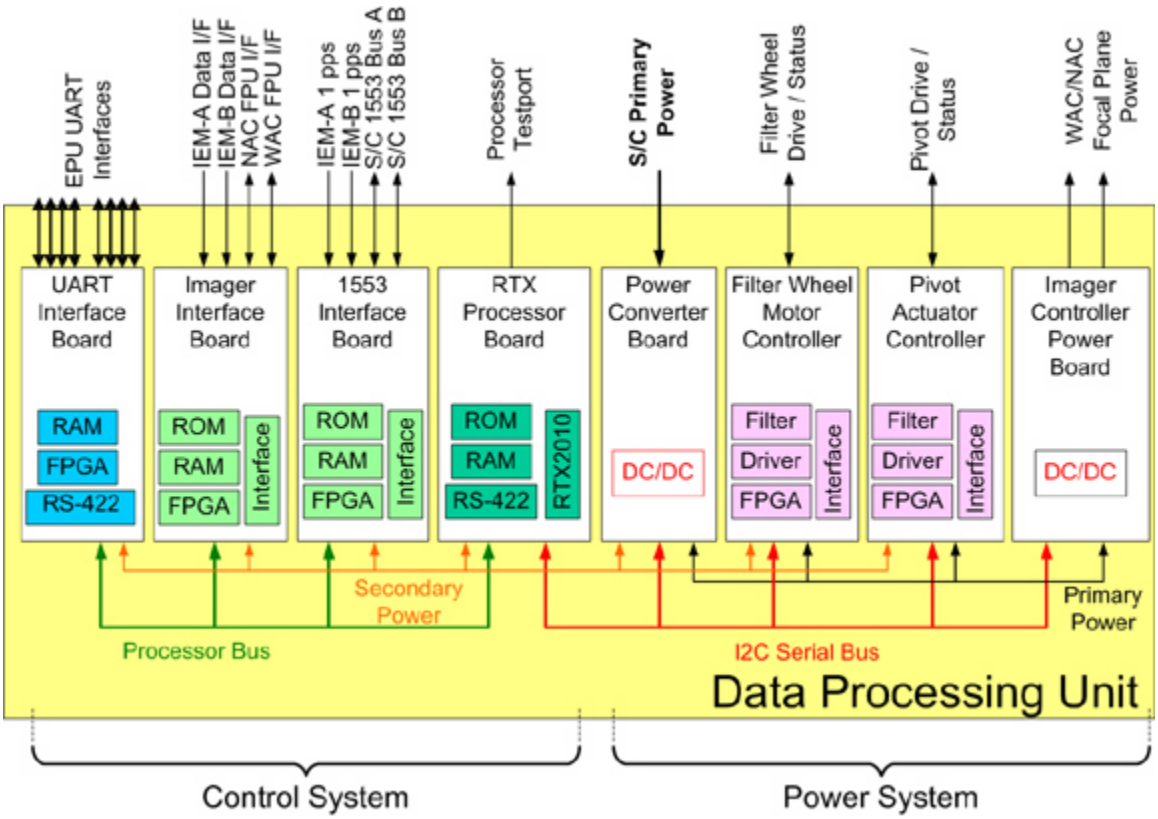

Figure 23. MESSENGER DPU block diagram

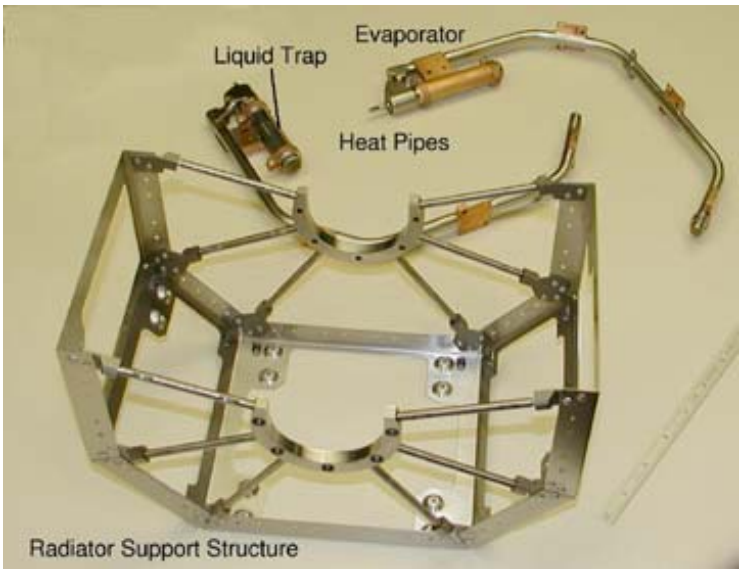

Figure 24. Heat pipe diodes and supporting structure prior to assembly.????

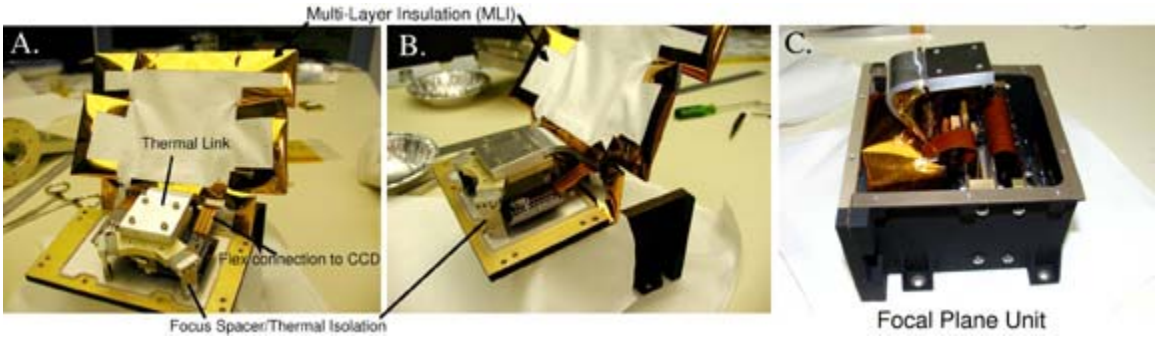

Figure 25. Front panel of NAC FPU.

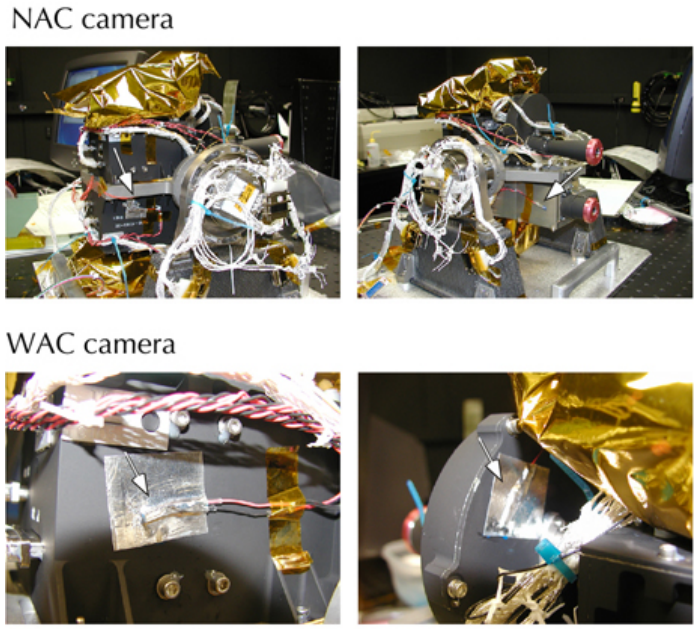

Figure 26. Locations of termperature sensors in MDIS. The top two panels, left to right, show "NAC_camera_temp 1" and “NAC_camera_temp 2.” The bottom two panels, left to right, show "WAC_camera_temp 1" and “WAC_camera_temp 2.”

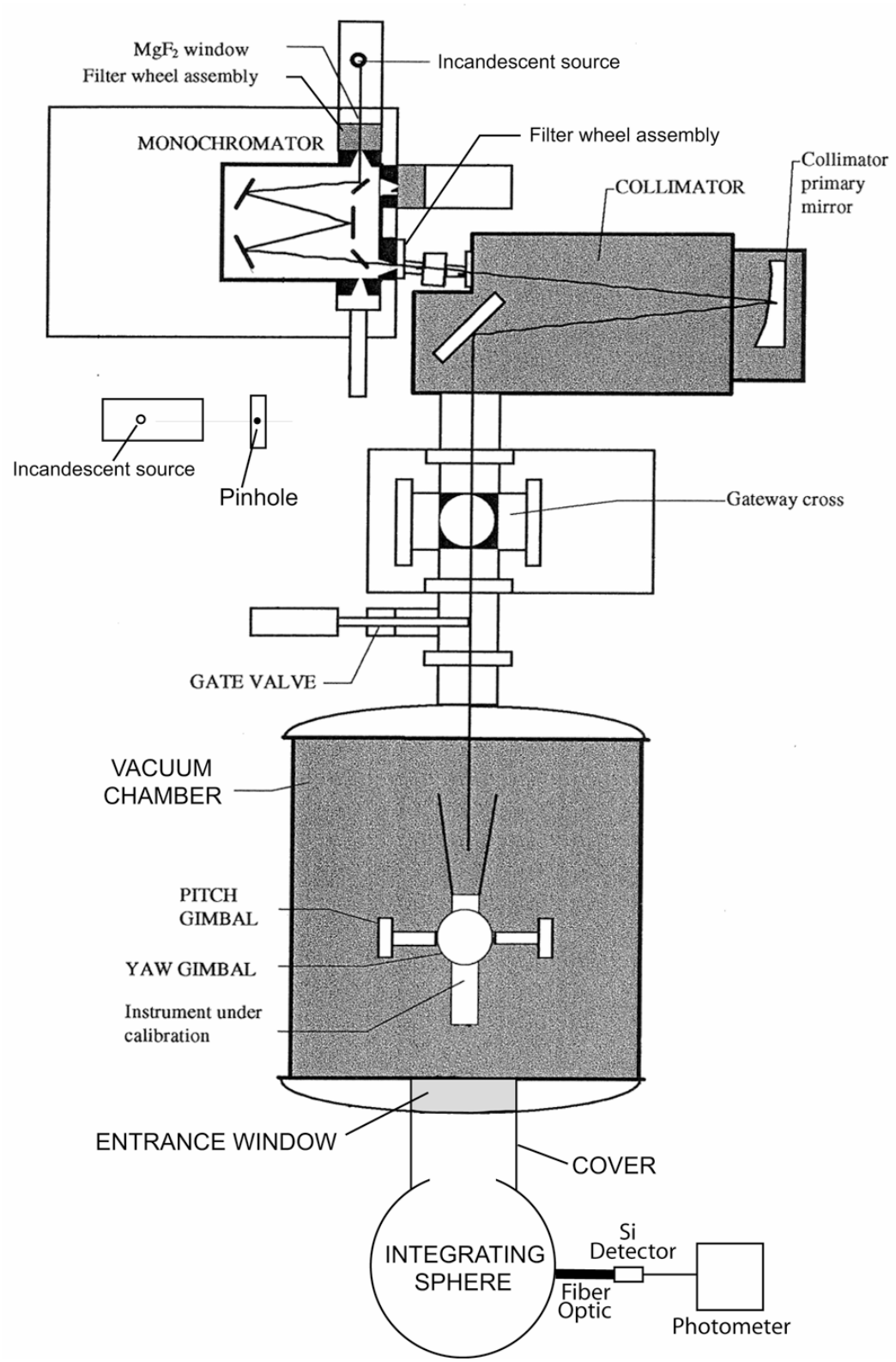

Figure 27. Optical calibration facility hardware configuration used for MDIS calibration.

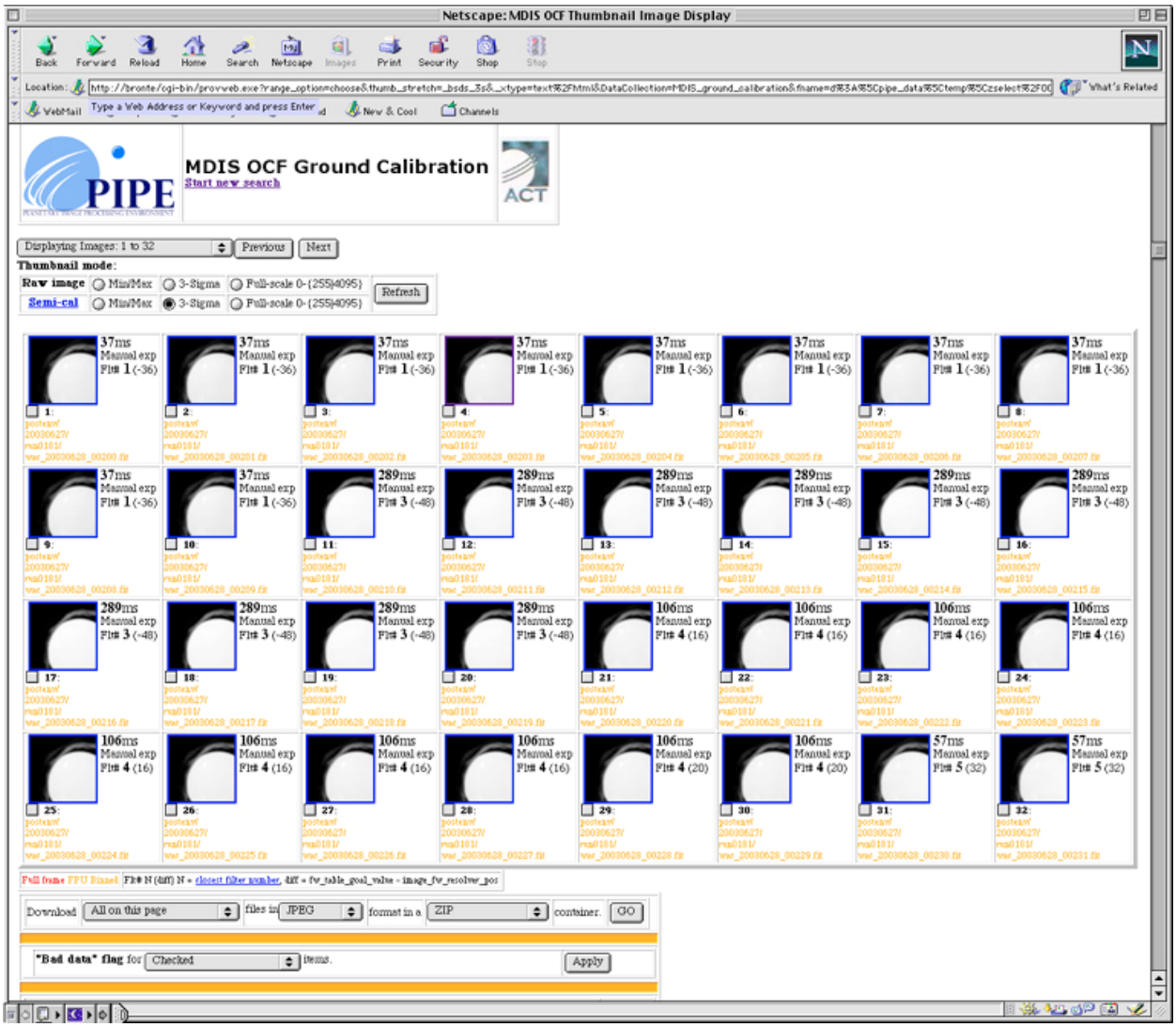

Figure 28. Web interface to the MESSENGER Science Operations Center, showing one set of MDIS calibration images of the integrating sphere. DELETE THIS FIGURE

(b)

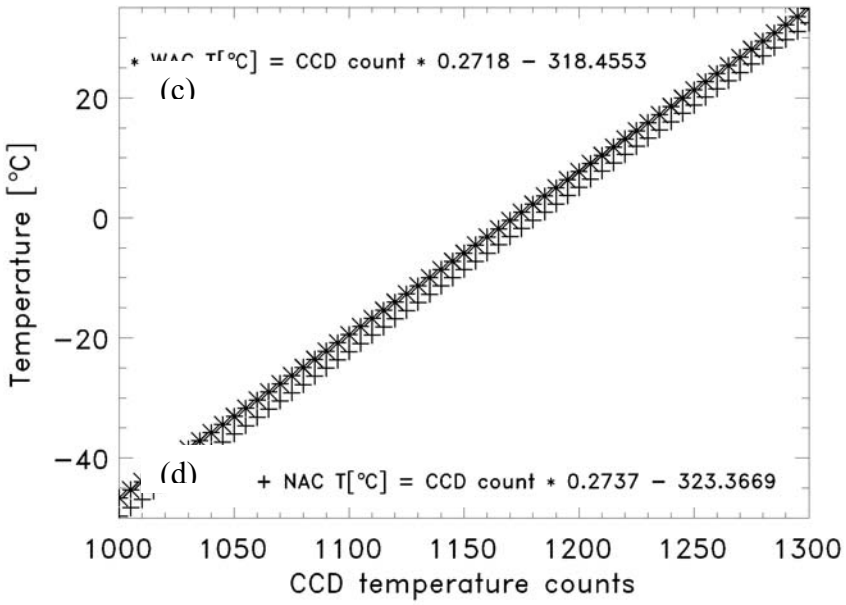

Figure 29. Conversion from CCD temperature counts to °C for WAC and NAC. DELETE THIS FIGURE

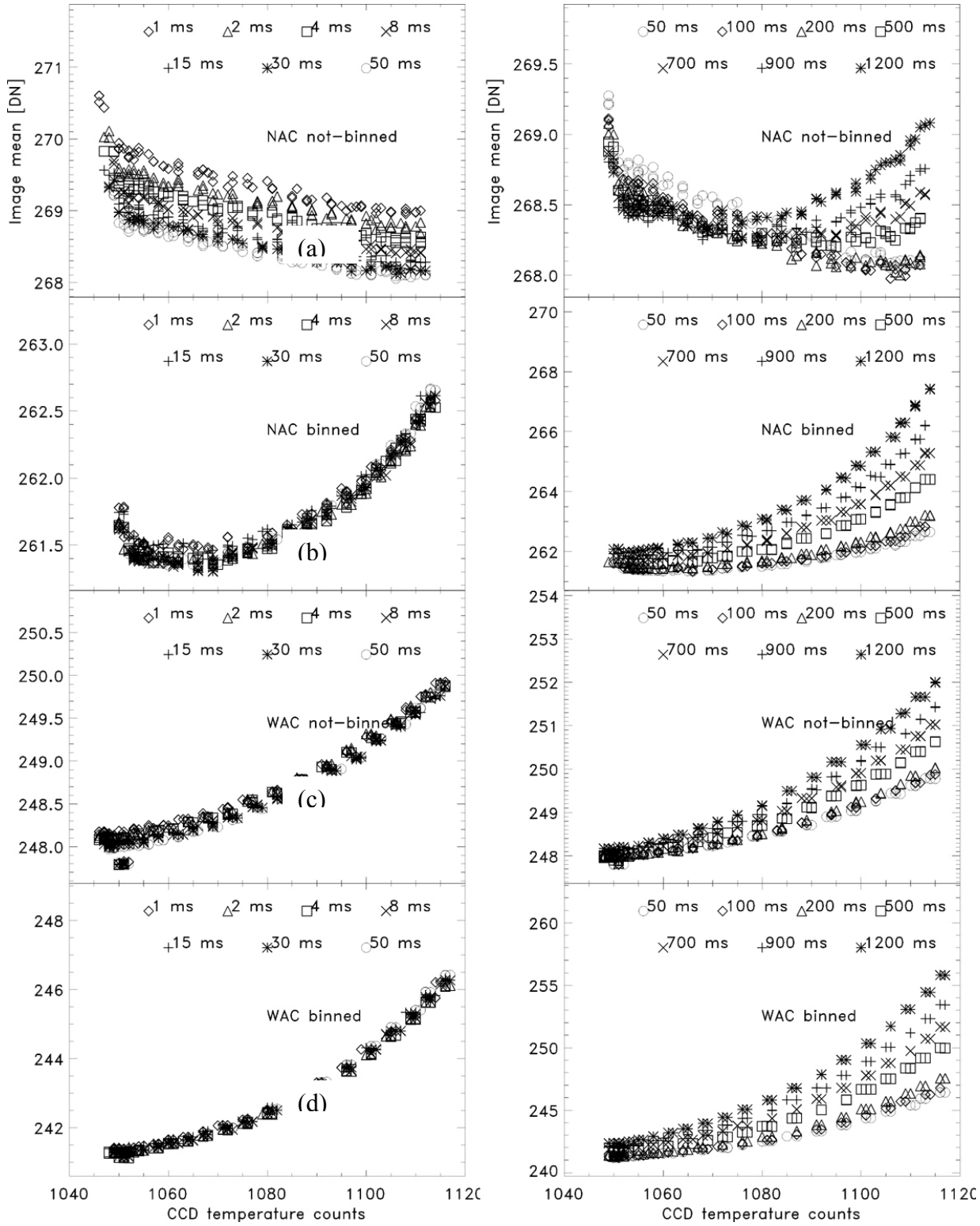

Figure 30. Dark image mean as a function of temperature counts and exposure time for the WAC and NAC in each binning state.

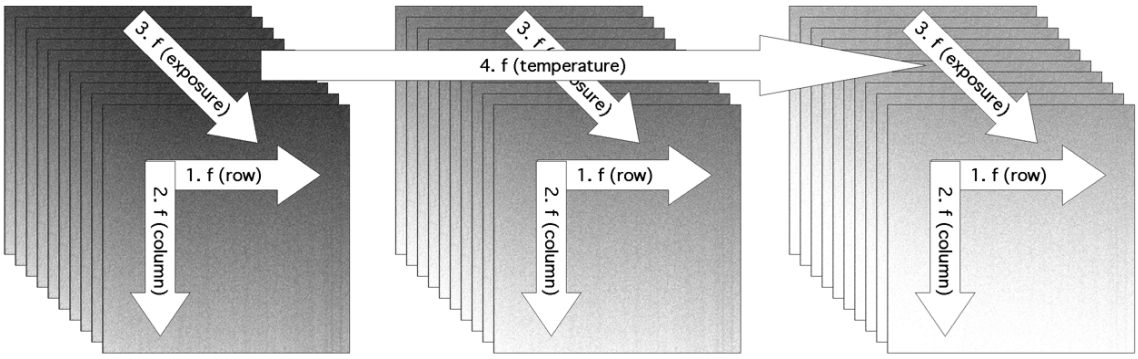

Figure 31. Schematic representation of dark model calculation decision tree. Caption needs amplification?

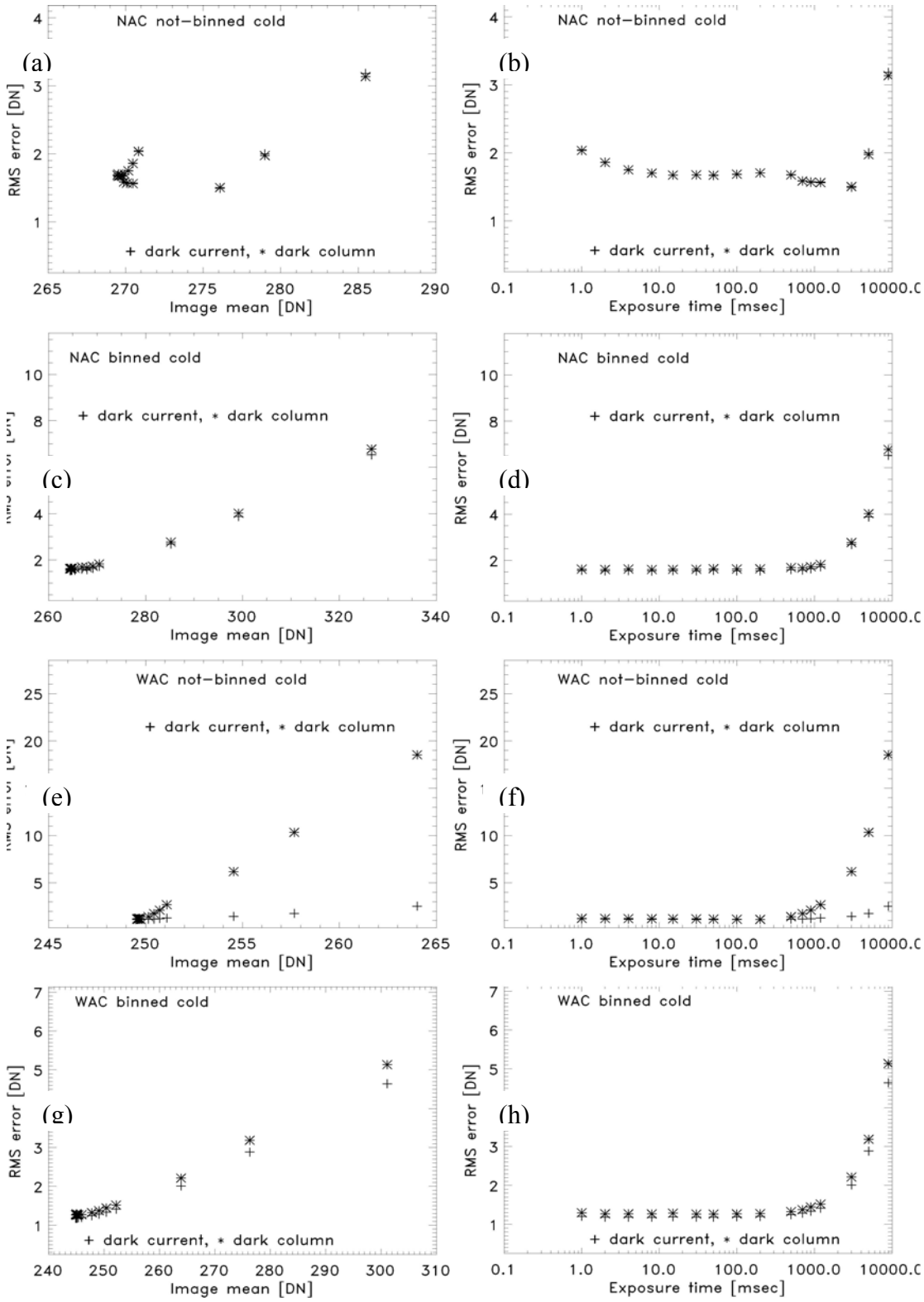

Figure 32. RMS error of the dark models to image pixels as a function of dark image mean and exposure time for the NAC and WAC binned and not binned, from OCF calibration data.

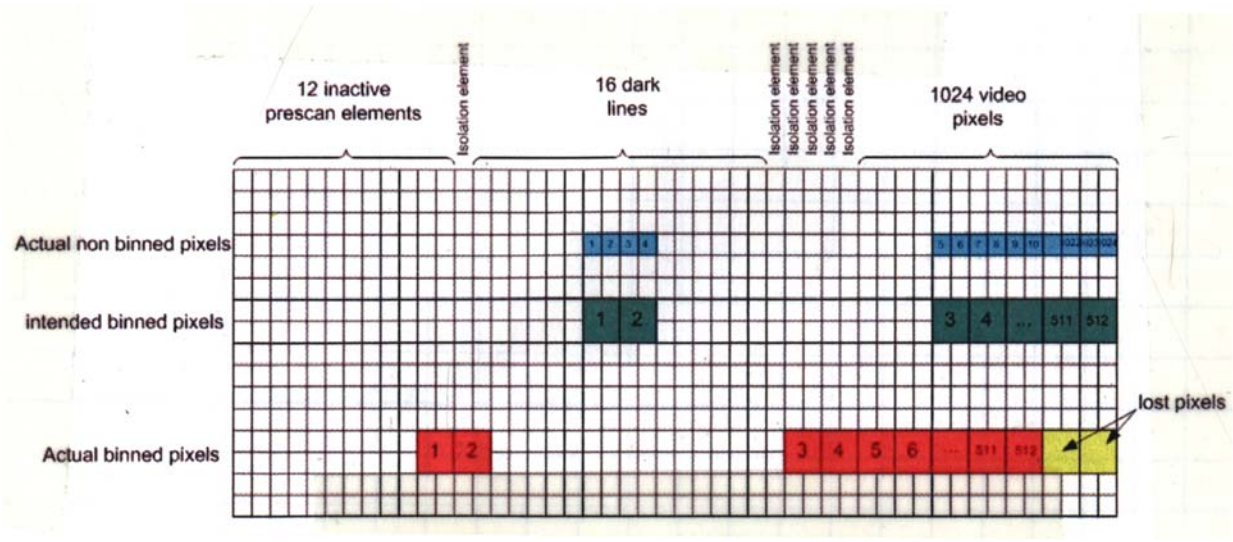

Figure 33. Pixels intended for dark columns, and actual pixels used in binned images for WAC and NAC.

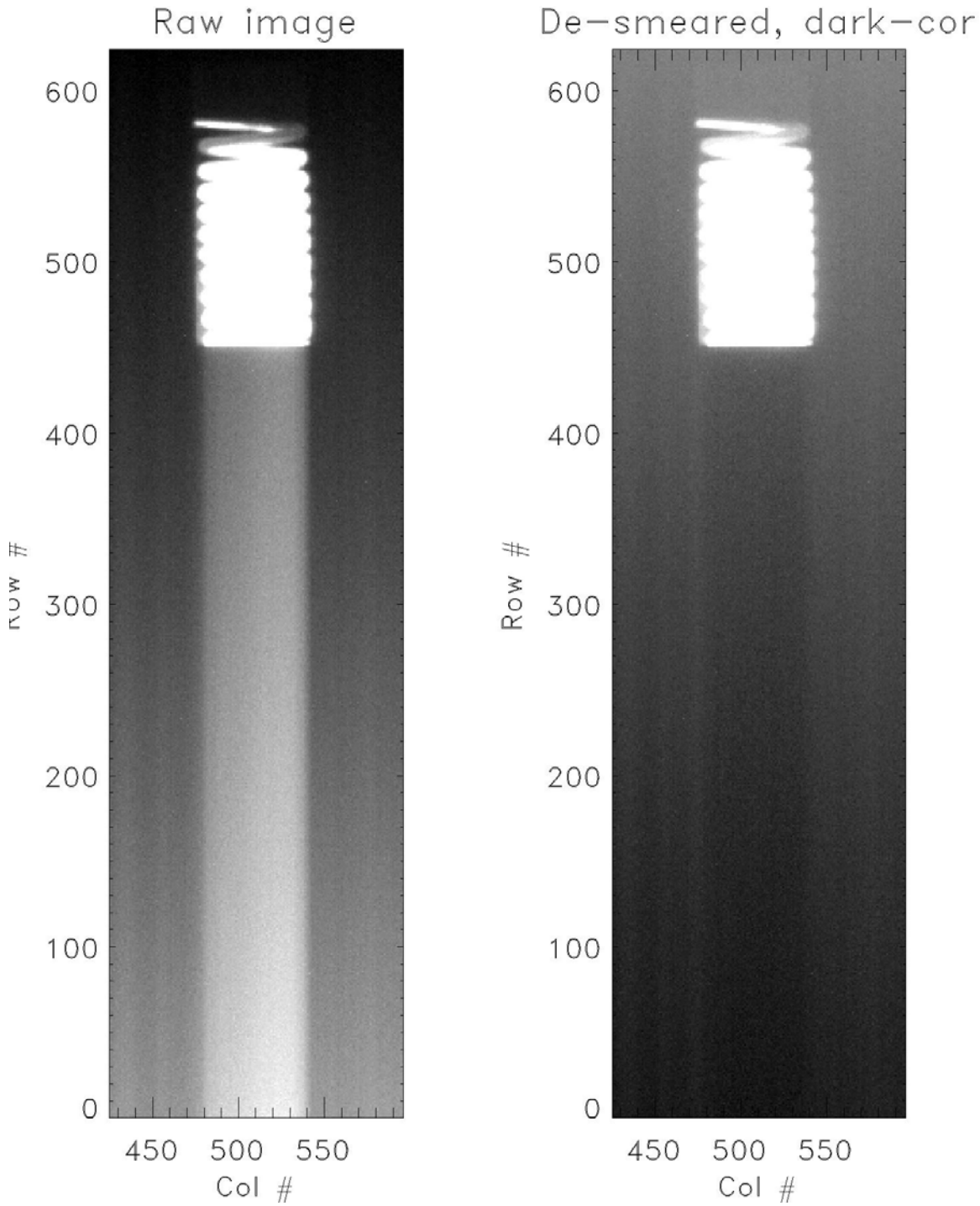

Figure 34. Smear correction for not-binned NAC. Image is of a light bulb filament, taken at 5 msec exposure time at 23C .

Figure 35. Scale, offset, and relative twist of NAC and WAC images.

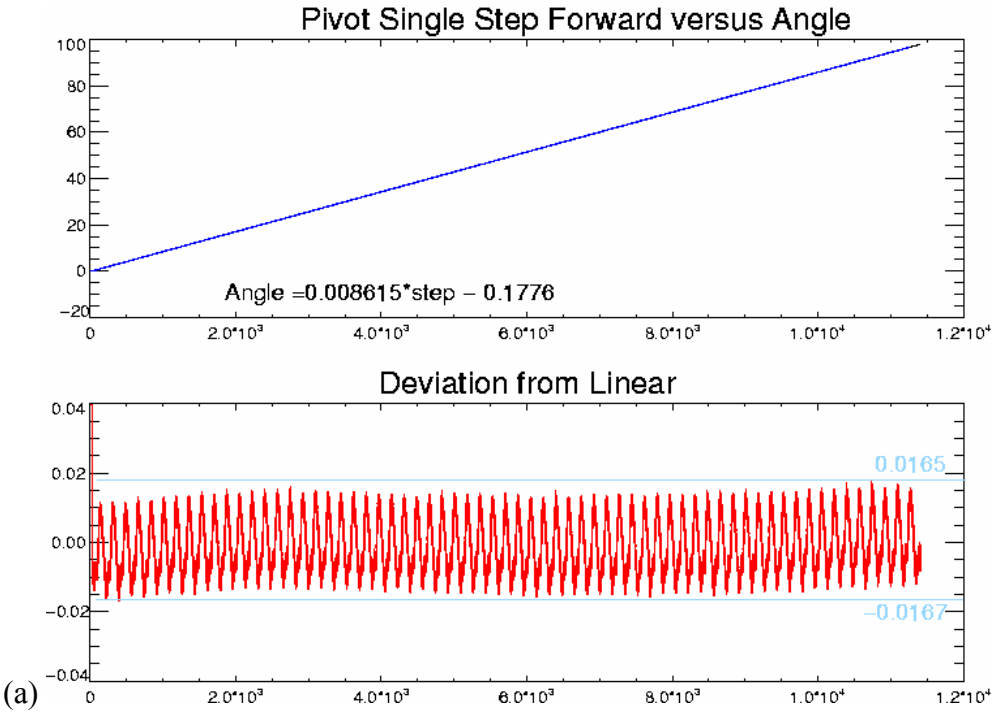

(a)

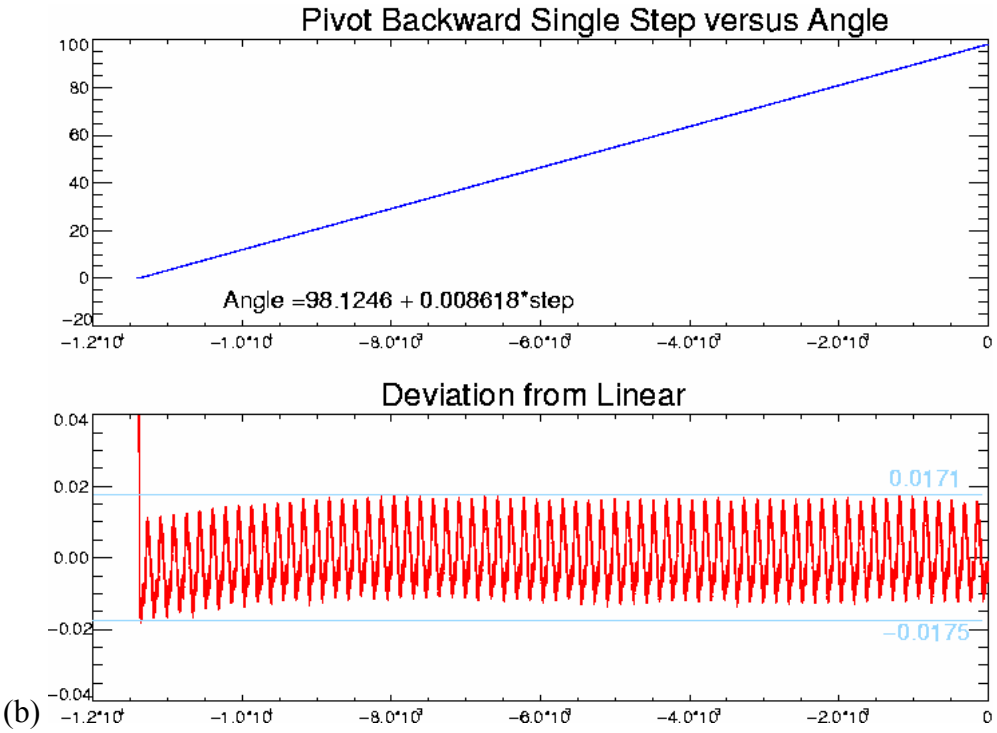

(b)

Figure 36. Deviations from linear translation of pivot position to angle, for motion of the pivot in the forward direction (a) and reverse direction (b).

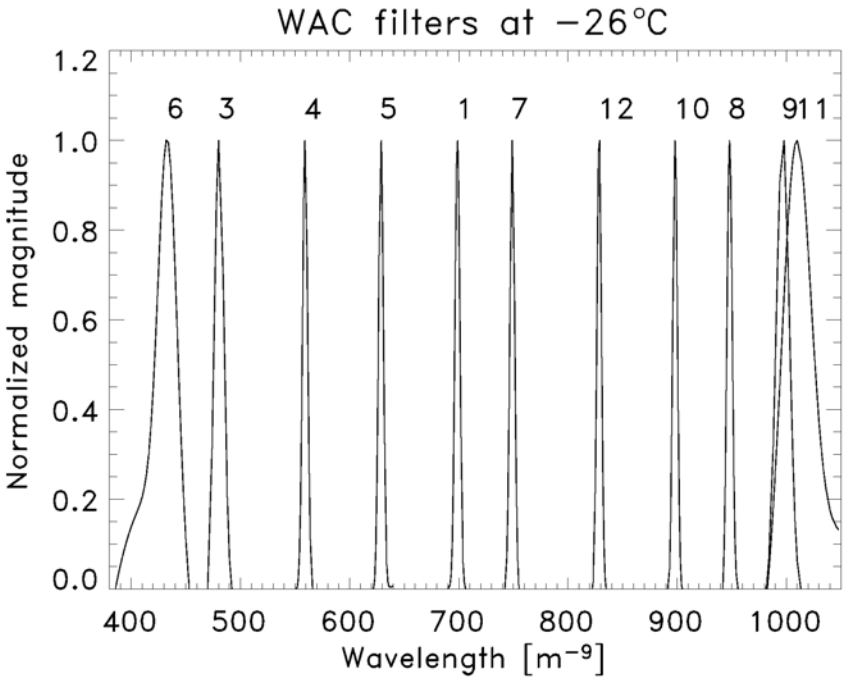

Figure 37. WAC filter centers and bandpasses at -26°C

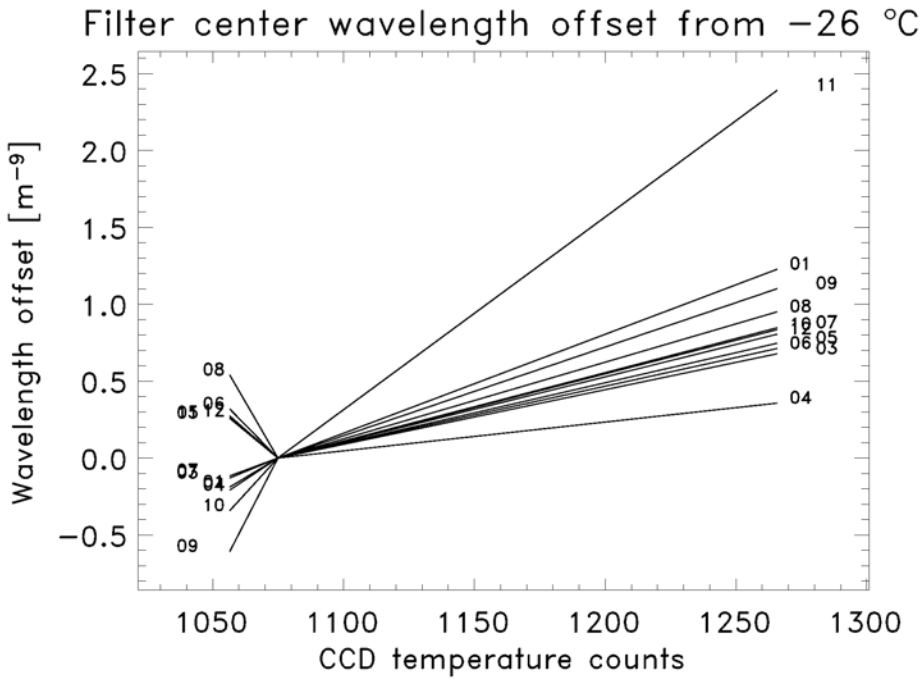

Figure 38. Offset in WAC filter center relative to position at -26°C, as a function of temperature as expressed in raw CCD temperature counts.

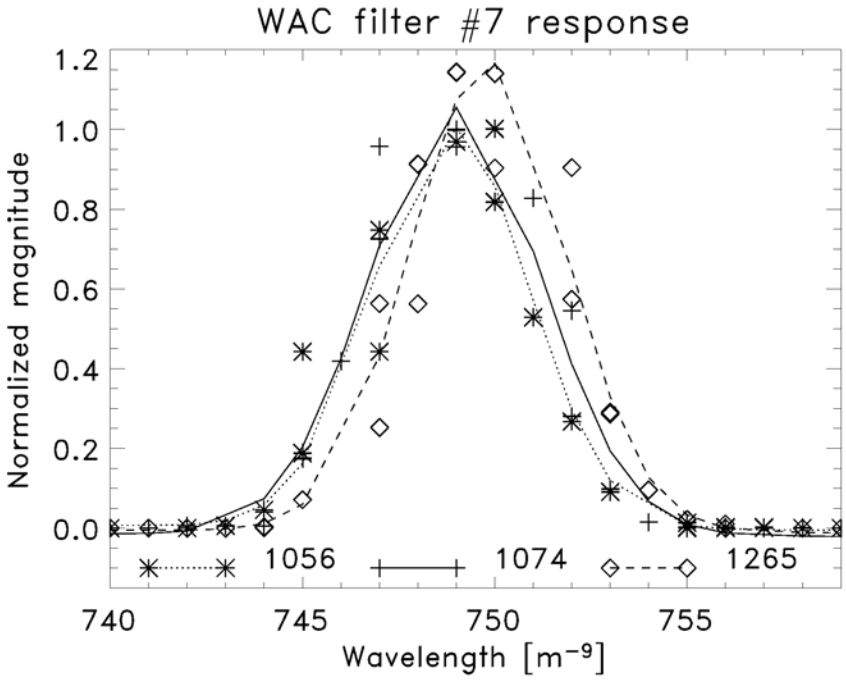

Figure 39. Shift in WAC filter 7 (750 nm) bandpass between -26°C and room temperature. The diagram indicates temp curves in counts and the caption uses C – confusing…

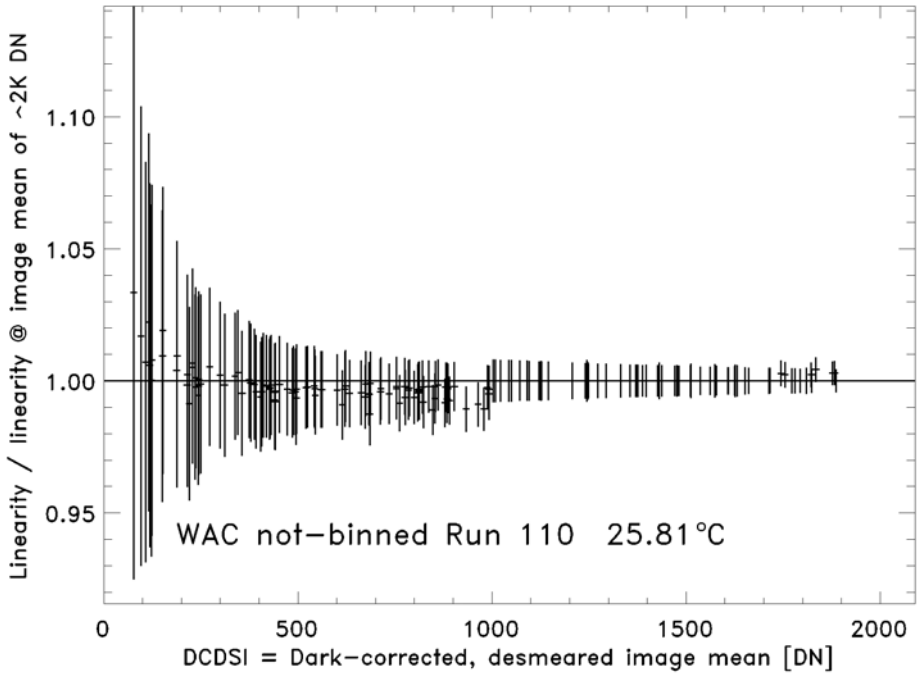

Figure 40. Not-binned WAC normalized linearity at CCD temperature count 1267. Filters 1, 3, 5, 7-10 and 12 are plotted without distinction.

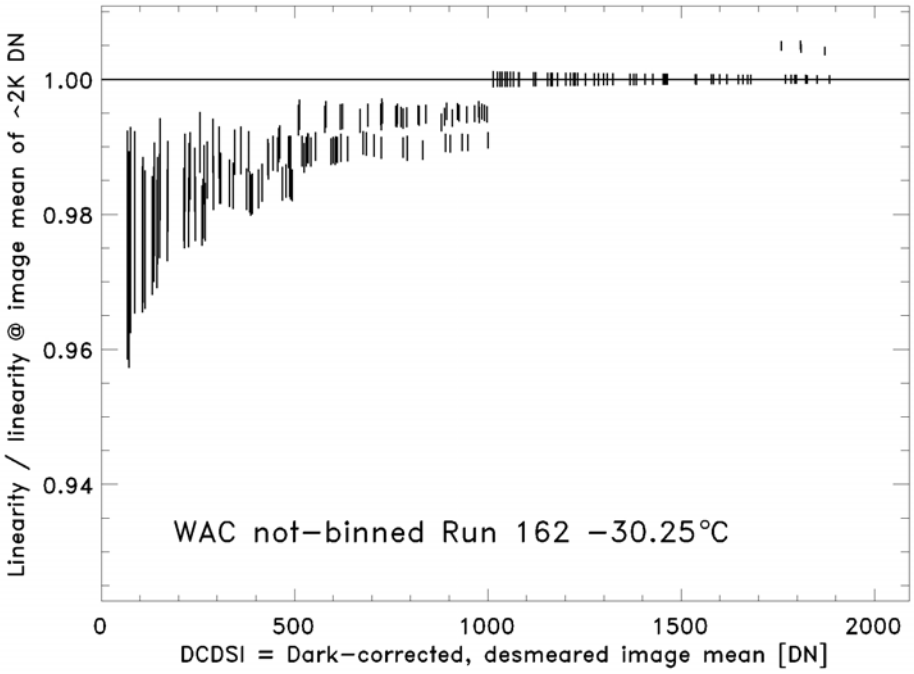

Figure 41. Not-binned WAC linearity at CCD temperature count 1060. Filters 1, 3, 5, 7-10 and 12 are plotted without distinction.

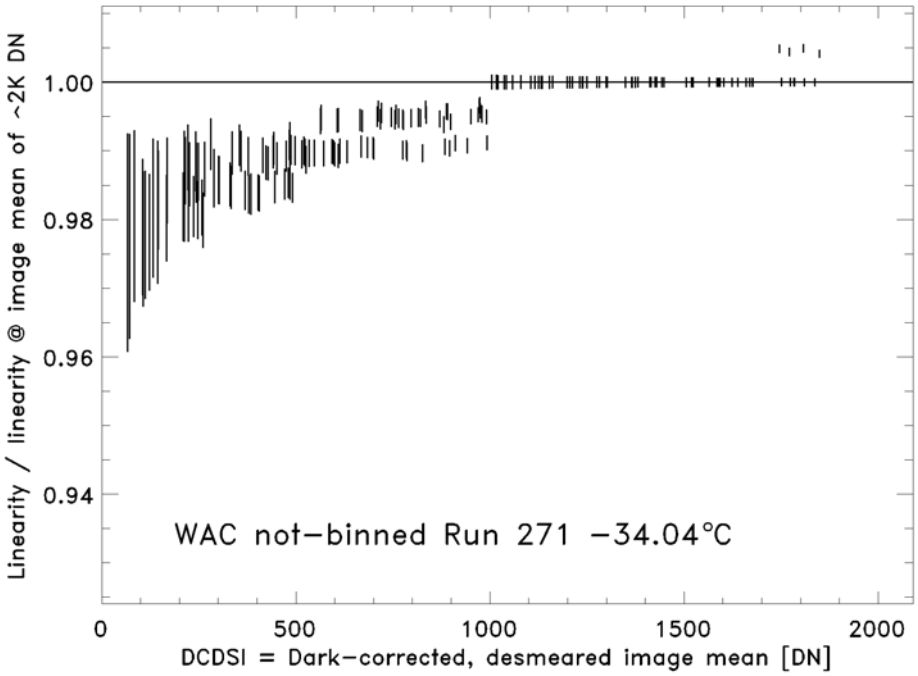

Figure 42. Not-binned WAC linearity at CCD temperature count 1046. Filters 1, 3, 5, 7-10 and 12 are plotted without distinction.

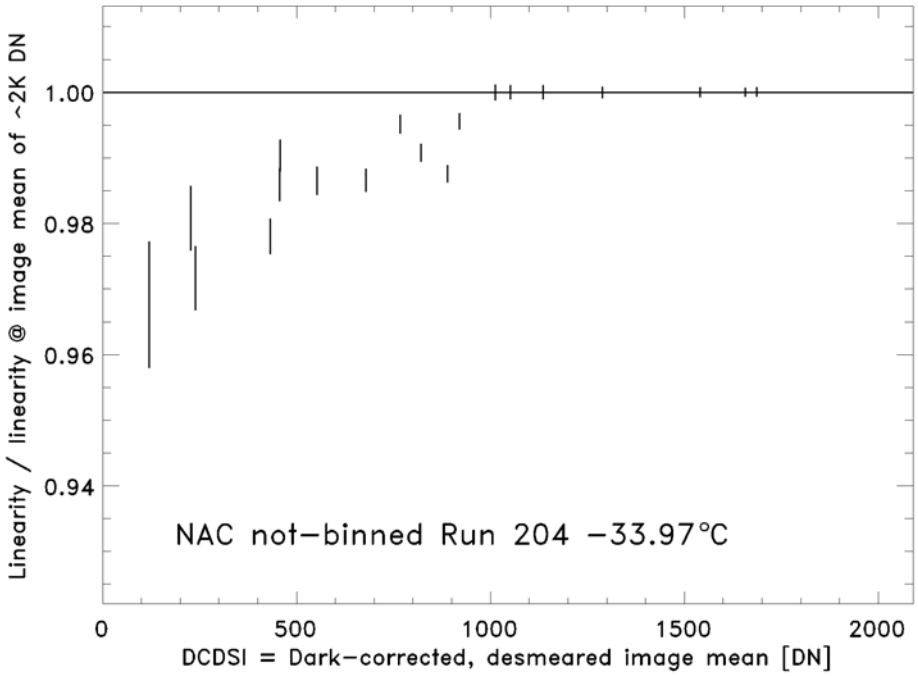

Figure 43. Not-binned NAC linearity at CCD temperature count 1057.

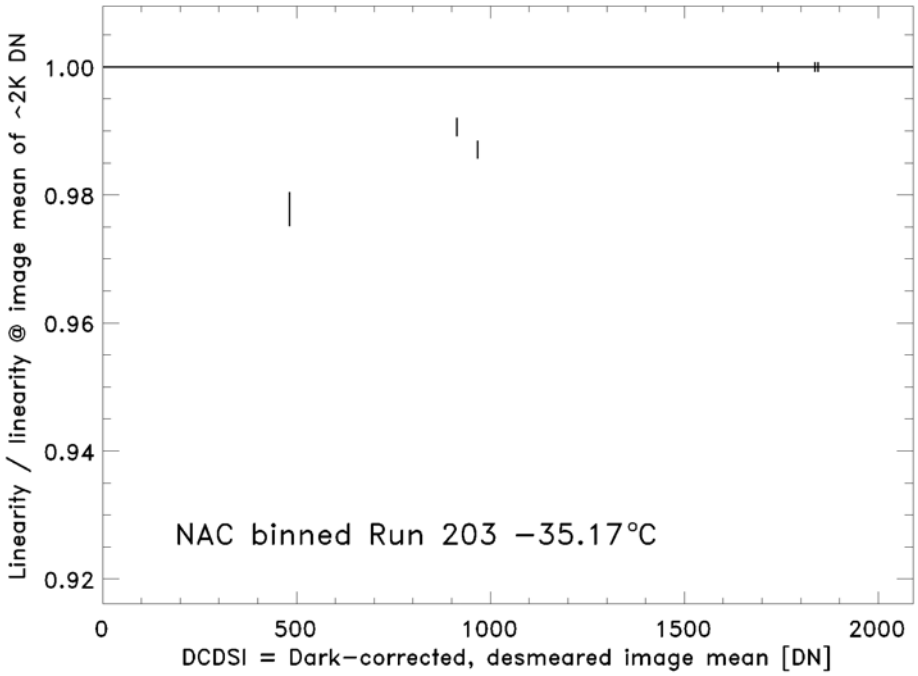

Figure 44. Binned NAC linearity at CCD temperature count 1053.

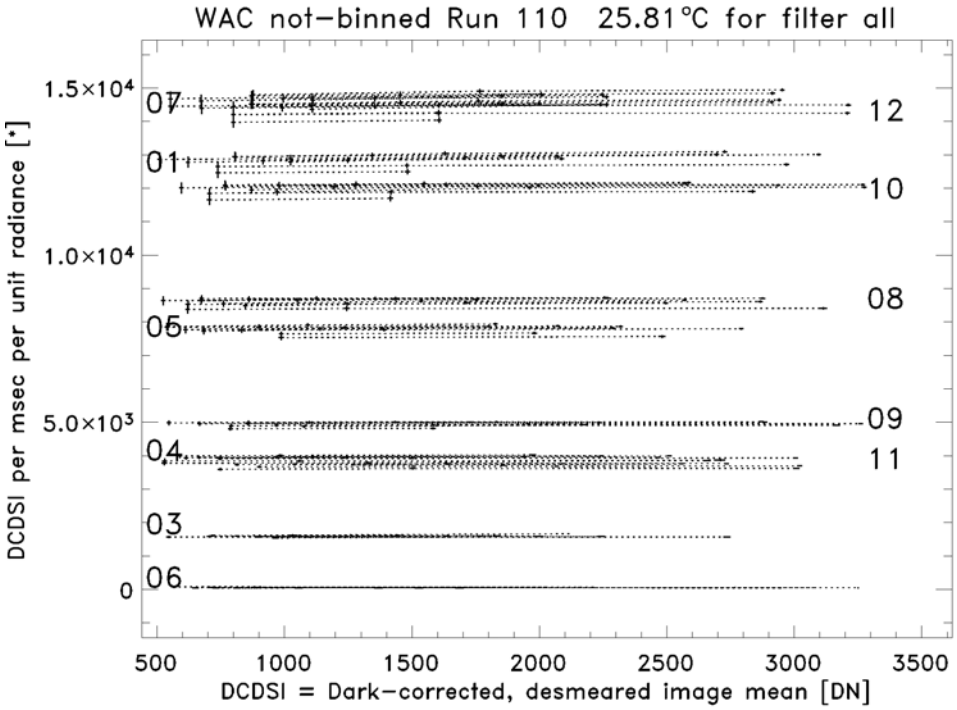

Figure 45. Not-binned WAC responsivity at CCD temperature count 1267 (26°C). Radiance is in units W m^{-2} nm^{-1} sr^{-1}. The lines represent different light combinations; groupings of lines correspond to different filters, whose numbers as given in Table 4 are indicated.

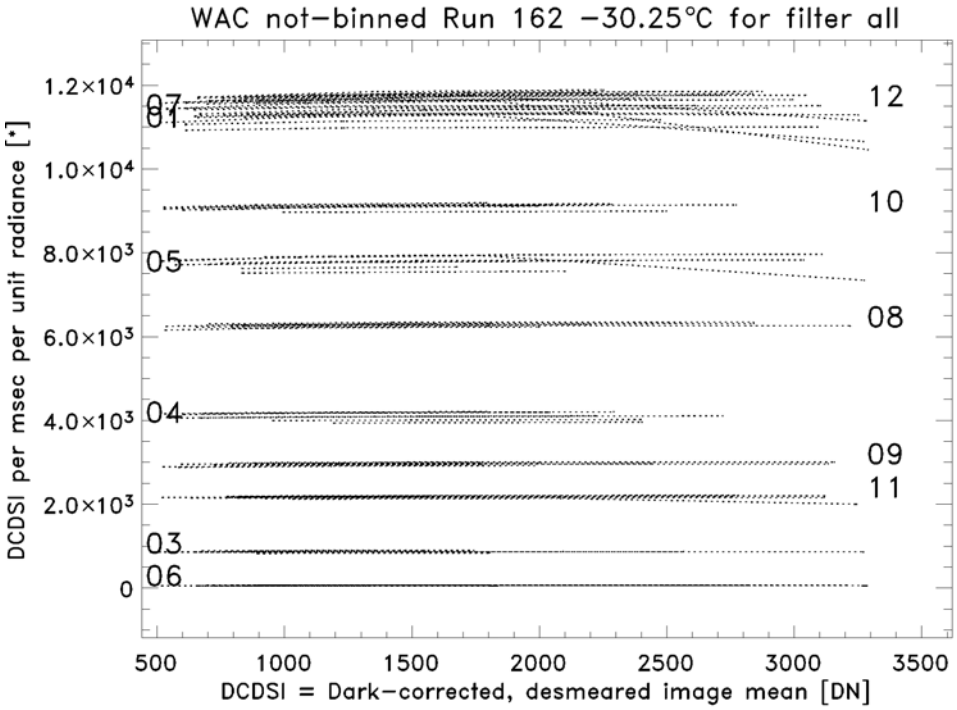

Figure 46. Not-binned WAC responsivity at CCD temperature count 1060 (-30°C). Radiance is in units W m^{-2} nm^{-1} sr^{-1}. The lines represent different light combinations; groupings of lines correspond to different filters, whose numbers as given in Table 4 are indicated.

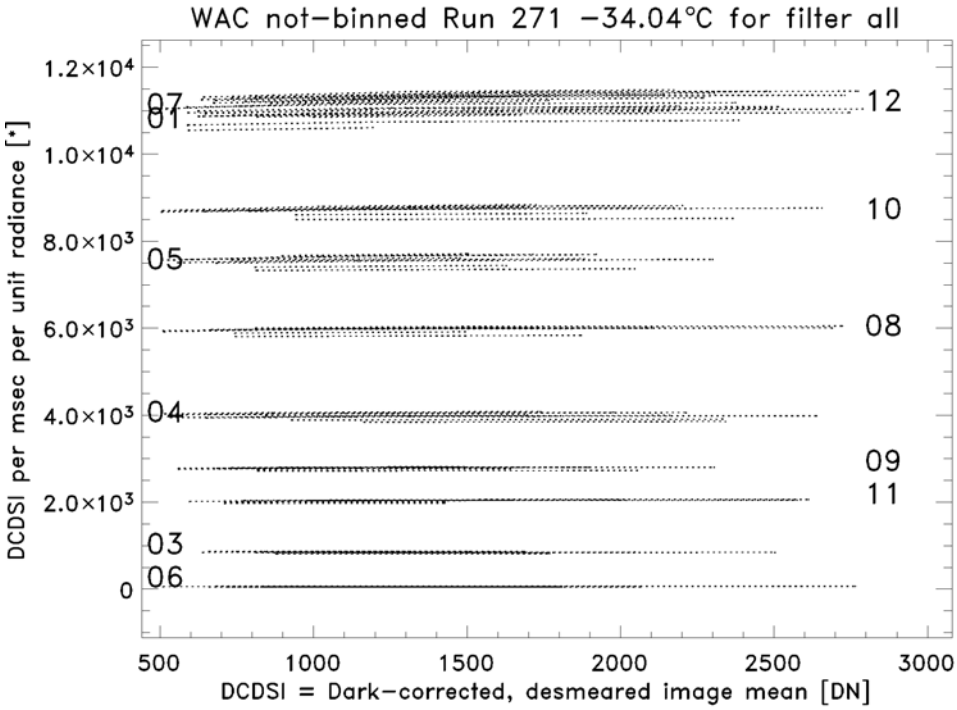

Figure 47. Not-binned WAC responsivity at CCD temperature count 1046 (-34°C). Radiance is in units W m^{-2} nm^{-1} sr^{-1}. The lines represent different light combinations; groupings of lines correspond to different filters, whose numbers as given in Table 4 are indicated.

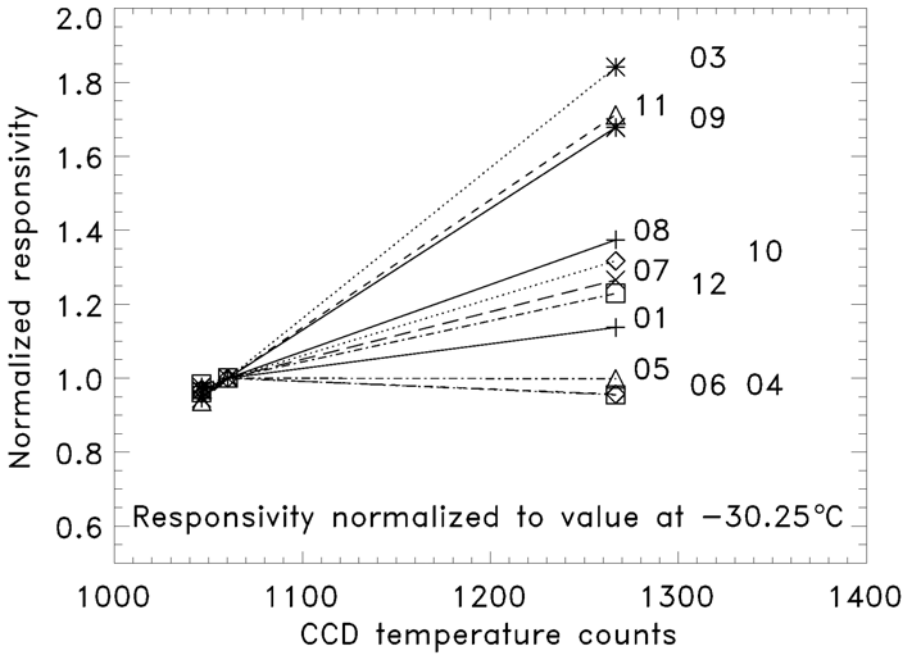

Figure 48. Relative responsivity vs. temperature for not-binned WAC measurements, normalized to the responsivity at -30°C.

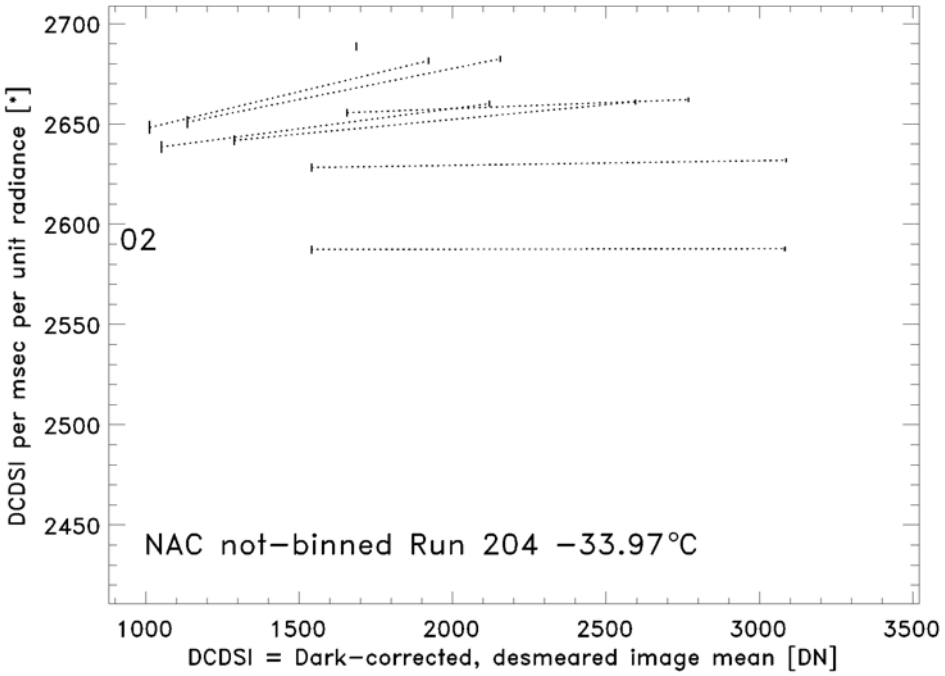

Figure 49. Not-binned NAC responsivities for CCD temperature count 1057 (-34°C). Radiance is in units W m^{-2} nm^{-1} sr^{-1}. The lines represent different light combinations.

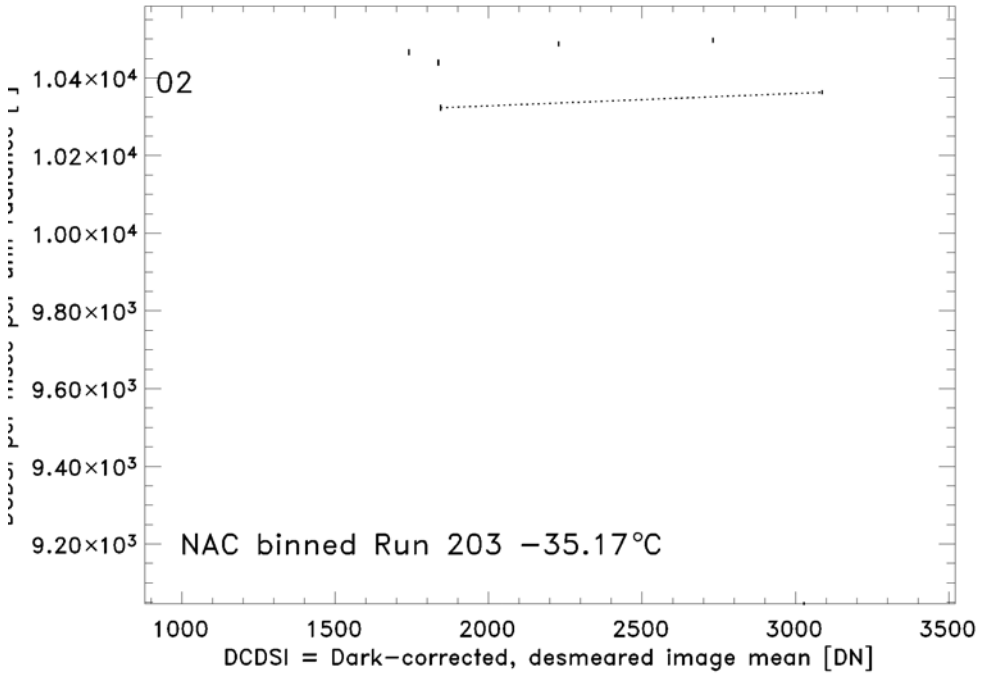

Figure 50. Binned NAC responsivities for CCD temperature count 1053. Radiance is in units W m^{-2} nm^{-1} sr^{-1}. The lines represent different light combinations.

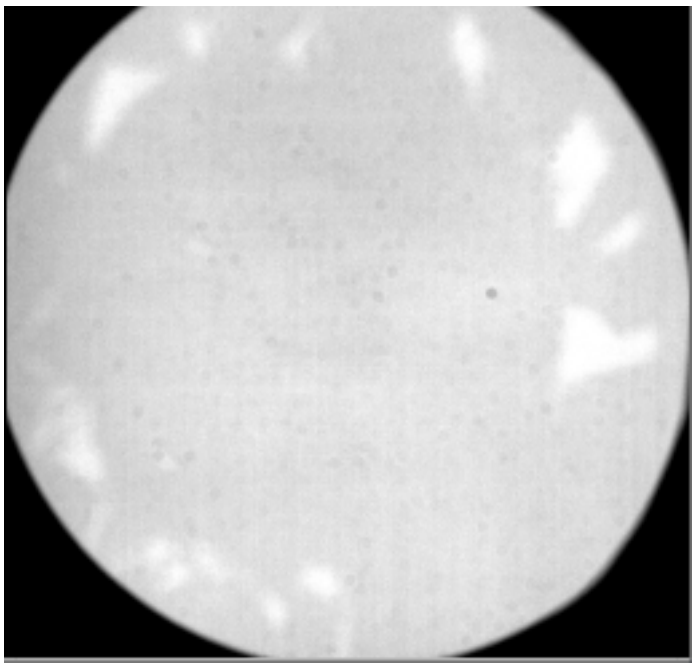

Figure 51. Non-uniformities are visible in integrating sphere images acquired through the quartz window in the OCF chamber door (Instrument or calb facilities?).

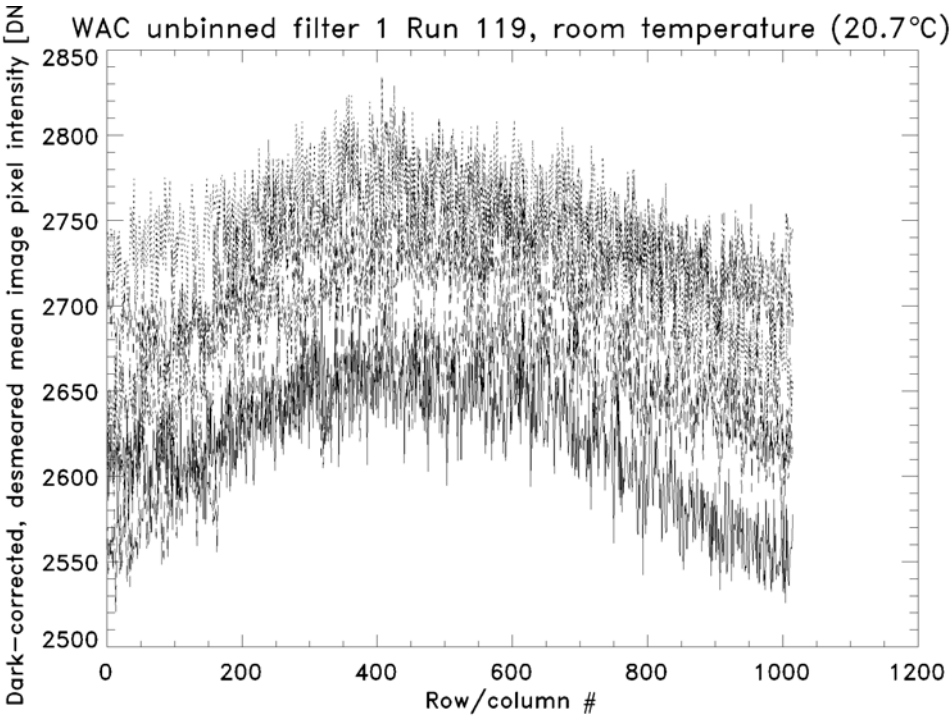

Figure 52. Profile cuts through a not-binned 699-nm filter WAC integrating sphere image, showing the $\cos^4$ falloff in response off the optic axis. Image is average of 100 images after dark-model and desmearing correction.

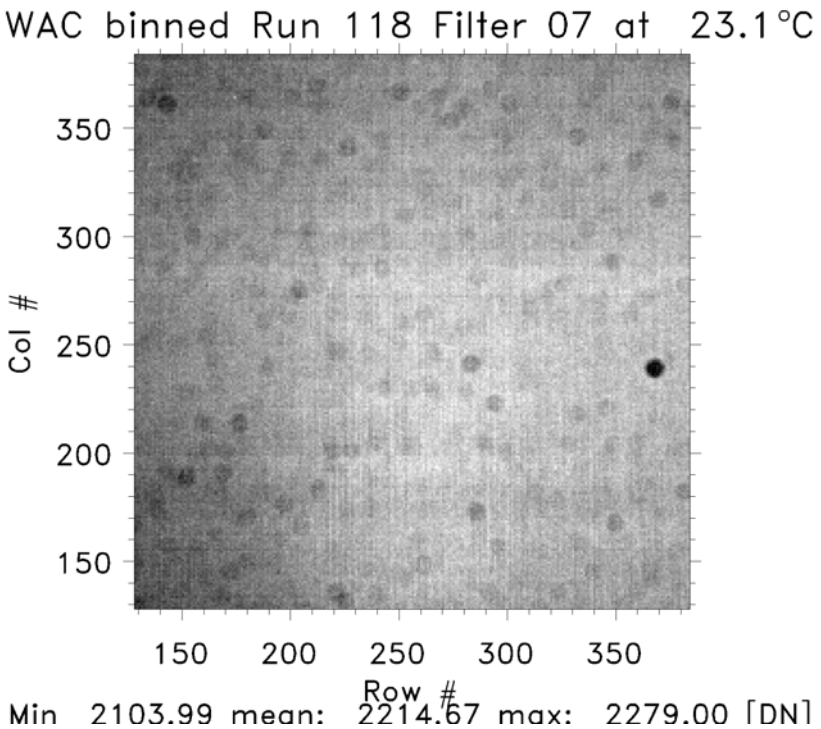

Figure 53. Contrast-enhanced room temperature binned WAC integrating sphere image with portal door open.

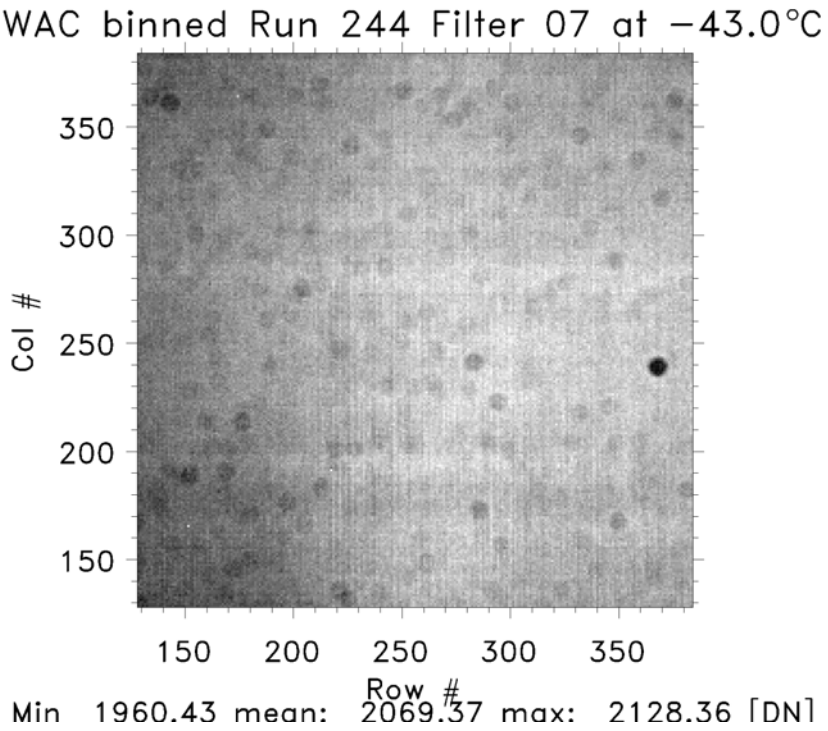

Figure 54. Contrast-enhanced, cold binned integrating sphere image with portal door closed.

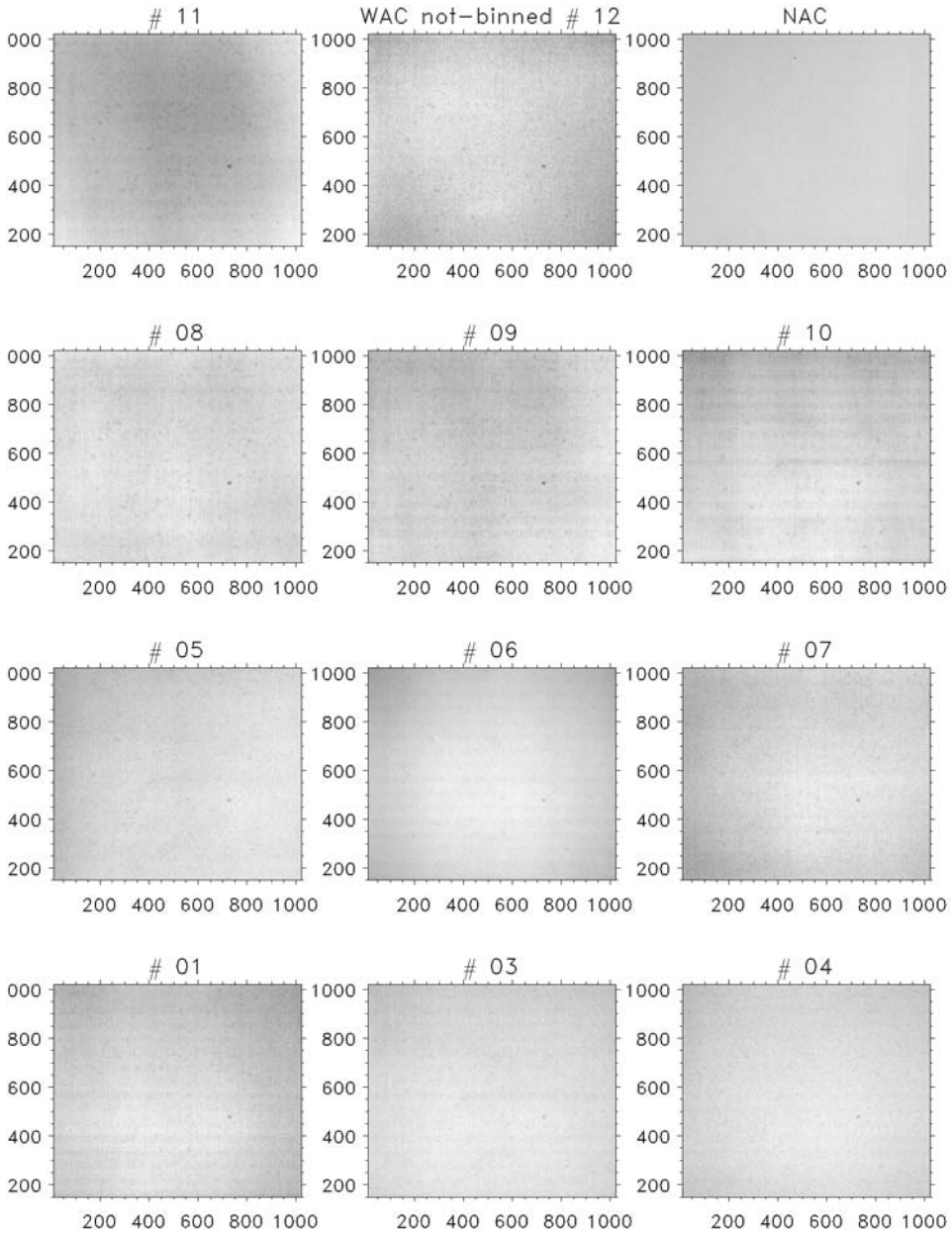

Figure 55. Contrast-enhanced not-binned flat fields.

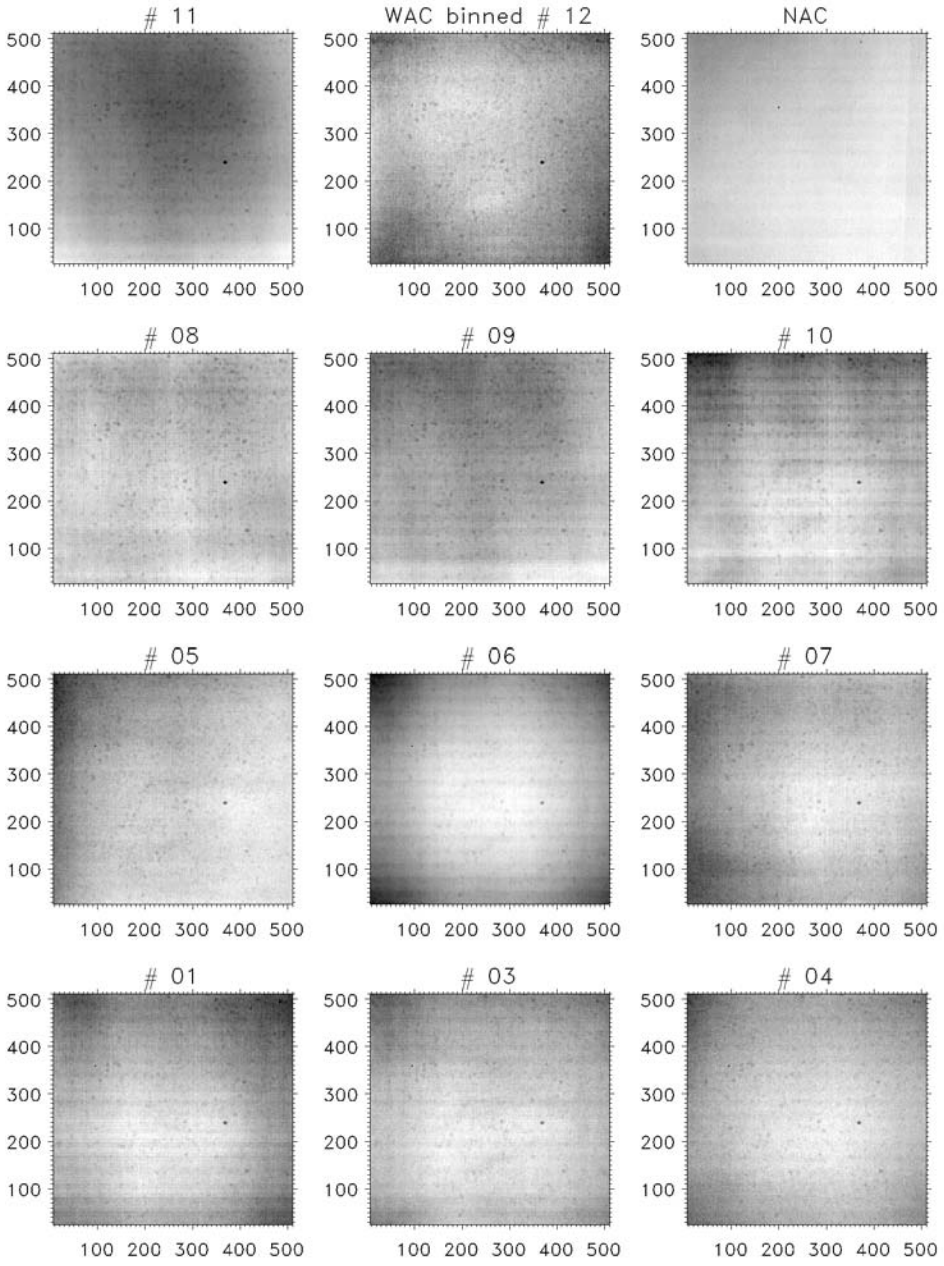

Figure 56. Contrast-enhanced binned flat fields.

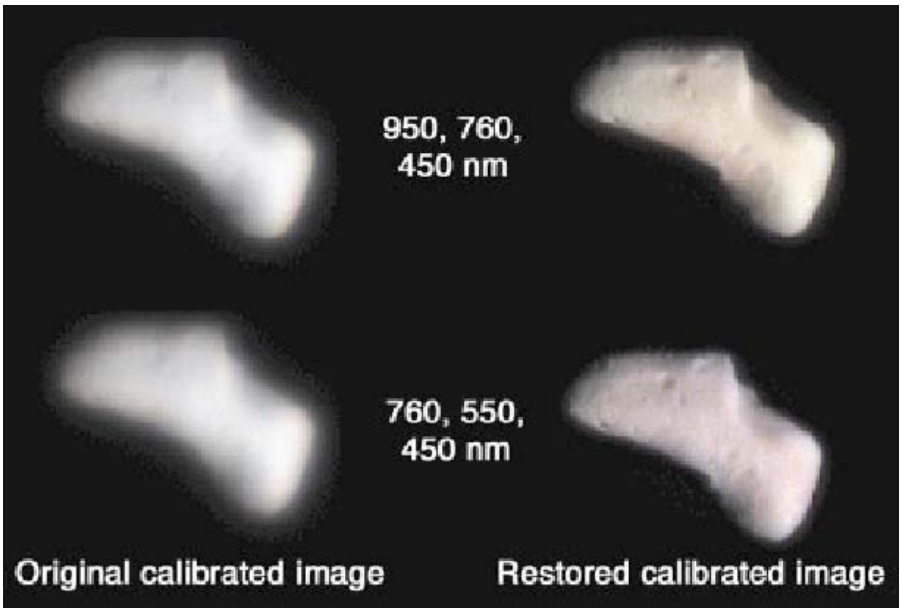

Figure 57. Effect of image restoration using the optimal filter on a NEAR image blurred due to contaminants on the optics. DELETE – refer reader to original MSI paper.

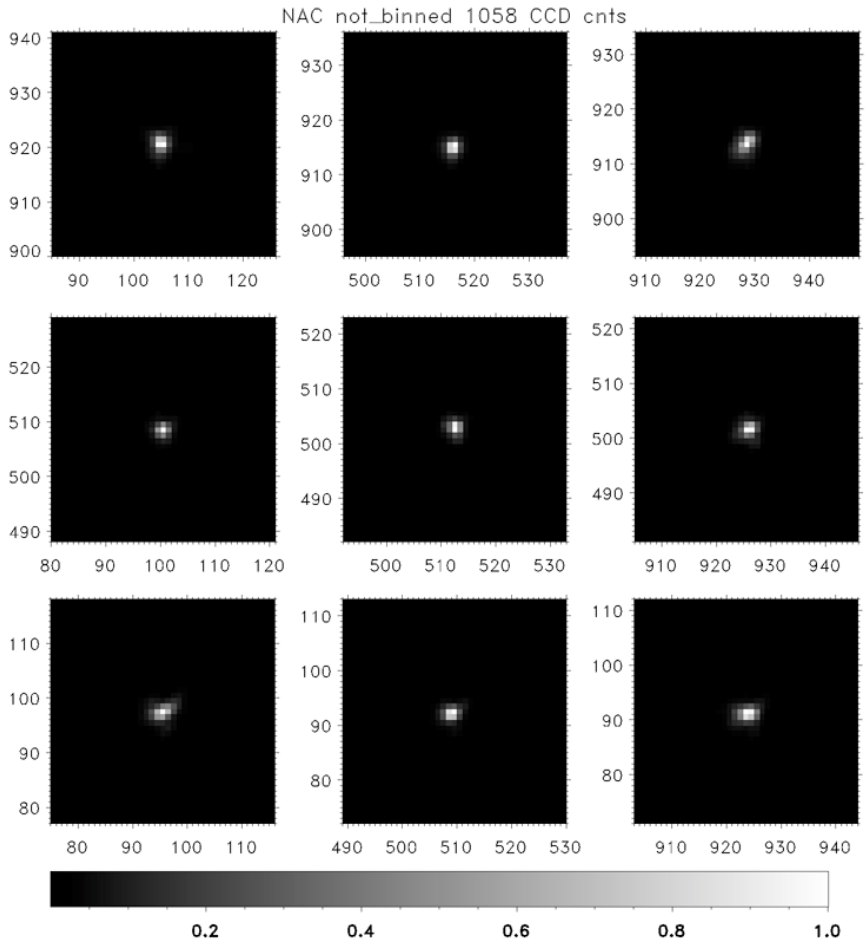

Figure 58. Two-dimensional intensity distribution of the NAC point spread function.

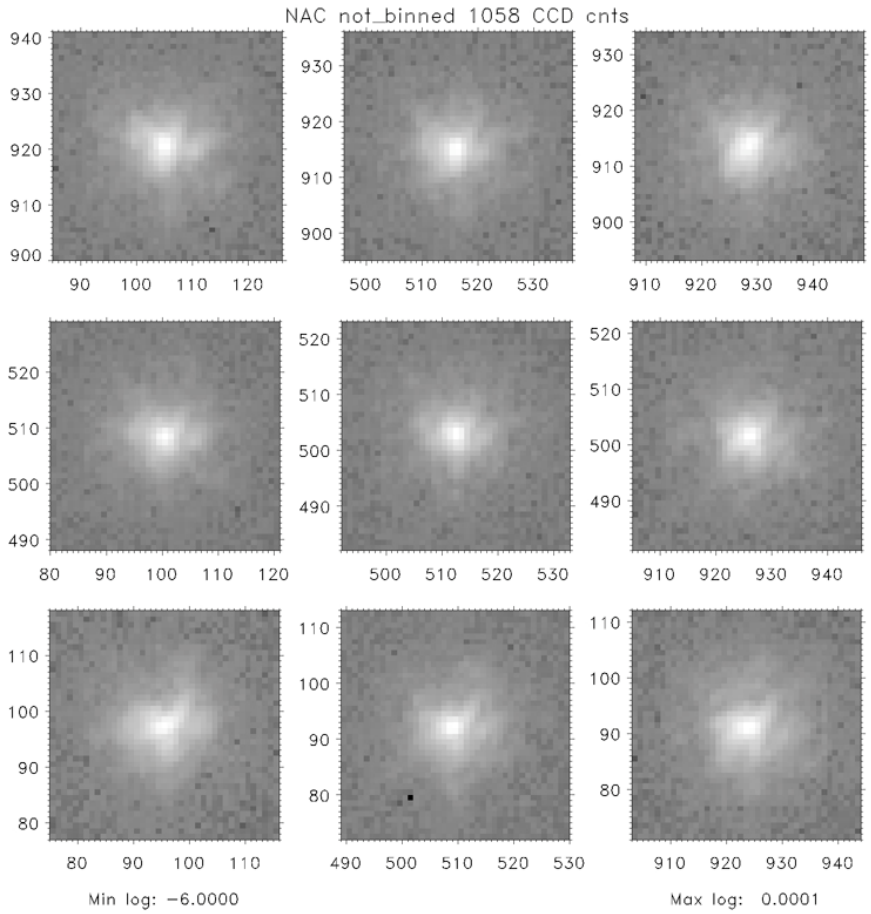

Figure 59. Two-dimensional intensity distribution of the NAC point spread function, at a 3x3 grid of positions across the FOV. Pixel locations are labeled; position 0,0 is in the lower lest. The stretch is logarithmic from 10^{-6} to 1.